

## DNA sensing with nanopores in graphene nanoribbons

Heerema, Stephanie

**DOI**

[10.4233/uuid:5c1bd018-d612-48a2-97c4-ab49e982593e](https://doi.org/10.4233/uuid:5c1bd018-d612-48a2-97c4-ab49e982593e)

**Publication date**

2018

**Document Version**

Final published version

**Citation (APA)**

Heerema, S. (2018). *DNA sensing with nanopores in graphene nanoribbons*. [Dissertation (TU Delft), Delft University of Technology]. <https://doi.org/10.4233/uuid:5c1bd018-d612-48a2-97c4-ab49e982593e>

**Important note**

To cite this publication, please use the final published version (if applicable).  
Please check the document version above.

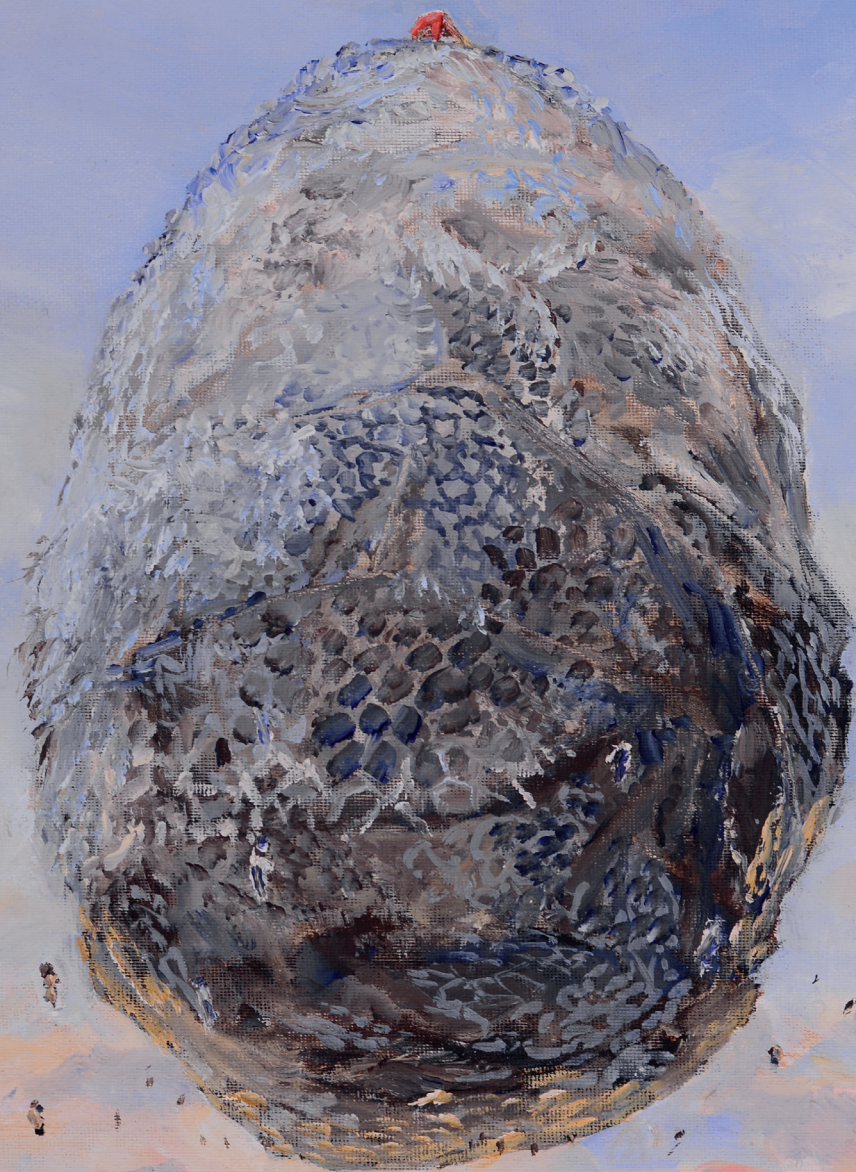
**Copyright**

Other than for strictly personal use, it is not permitted to download, forward or distribute the text or part of it, without the consent of the author(s) and/or copyright holder(s), unless the work is under an open content license such as Creative Commons.

**Takedown policy**

Please contact us and provide details if you believe this document breaches copyrights.  
We will remove access to the work immediately and investigate your claim.

DNA SENSING WITH NANOPORES IN  
GRAPHENE NANORIBBONS



STEPHANIE J. HEEREMA



DNA SENSING WITH NANOPORES IN  
GRAPHENE NANORIBBONS



# DNA SENSING WITH NANOPORES IN GRAPHENE NANORIBBONS

## **Dissertation**

for the purpose of obtaining the degree of doctor  
at Delft University of Technology  
by the authority of the Rector Magnificus prof.dr.ir. T.H.J.J. van der Hagen  
chair of the Board for Doctorates to be defended publicly on  
Wednesday 4 April 2018 at 15:00 o'clock

by

**STEPHANIE JOY HEEREMA**

Master of Science in Applied Physics, Delft University of Technology, The Netherlands  
born in Leiden, The Netherlands

This dissertation has been approved by the promotor:  
Prof. dr. C. Dekker

Composition of the doctoral committee:

Rector Magnificus                      chairperson  
Prof. dr. C. Dekker                      Delft University of Technology, promotor

Independent members:

Prof. dr. J.H.P. Bayley                      University of Oxford  
Prof. dr. M. Drndić                      University of Pennsylvania  
Dr. R.H. Scheicher                      Uppsala University  
Prof. dr. G.C.A.M Janssen                      Delft University of Technology  
Prof. dr. P.G. Steeneken                      Delft University of Technology

Other member:

Prof. dr. H.W. Zandbergen                      Delft University of Technology



Keywords:                      DNA sensing, DNA sequencing, biosensing, graphene nanopore,  
graphene nanoribbon, STEM.

Printed by:                      Gildeprint

Front & Back:                      'de Ontstijging' inspired by Magritte, by Jacob Kerssemakers.

Copyright © 2018 by S.J. Heerema

Casimir PhD Series 2018-09

ISBN 978.90.8593.341.0

An electronic version of this dissertation is available at <http://repository.tudelft.nl/>







# Contents

<b>PREFACE</b>	<b>XVII</b>
<b>1. GENERAL INTRODUCTION</b>	<b>1</b>
1.1 DNA: form and function	2
1.2 DNA sensing with nanopores	3
1.3 Graphene: a wonderful material	5
1.4 Nanopores in graphene nanoribbons	7
1.5 Thesis outline	8
References	10
<b>2. GRAPHENE NANODEVICES FOR DNA SEQUENCING</b>	<b>15</b>
2.1 Introduction	16
2.3 Tunnelling across a graphene nanogap	21
2.4 Inplane transport of a graphene nanoribbon with a nanopore	23
2.5 Detection methods based on DNA adsorption	26
2.6 Outlook	29
References	32
<b>3. CONTROLLING DEFECTS IN GRAPHENE FOR OPTIMIZING THE ELECTRICAL PROPERTIES OF GRAPHENE NANODEVICES</b>	<b>41</b>
3.1 Defects and electrical transport in graphene	42
3.1.1 Defects in graphene	42
3.1.2 Edge defects in graphene nanoribbons	45
3.2 Graphene self-healing and recrystallization	46
3.2.1 Graphene ultra-high vacuum healing and metal catalyzed etching at room-temperature	46
3.2.2 Silicon-assisted growth of graphene at high temperature	48
3.2.3 Graphene STEM sculpting at high temperature	48
3.2.4 Graphene nanoribbon edge recrystallization induced by Joule heating	49
3.3 Outlook and future challenges	50
References	52
<b>4. 1/f NOISE IN GRAPHENE NANOPORES</b>	<b>55</b>
4.1 Introduction	56

4.2 Results and discussion	57
4.3 Conclusion	63
4.4 Methods	64
References	65
<b>5. THROUGH-MEMBRANE ELECTRON-BEAM LITHOGRAPHY FOR ULTRATHIN MEMBRANE APPLICATIONS</b>	<b>69</b>
5.1 Introduction	70
5.2 Electron migration in thin SiN windows	71
5.3 Low-noise graphene nanopore devices	74
5.4 Supplementary information	77
References	79
<b>6. PROBING DNA TRANSLOCATIONS WITH INPLANE CURRENT SIGNALS IN A GRAPHENE NANORIBBON WITH A NANOPORE</b>	<b>81</b>
6.1 Introduction	82
6.2 Results	85
6.2.1 Fabrication workflow and device characterization	85
6.2.2 Decoupling of capacitive signals using a differential current amplifier	87
6.2.3 Proof-of-principle experiments	90
6.2.4 Probing DNA translocations	91
6.2.5 Data interpretation	92
6.3 Conclusions	94
6.4 Methods	95
6.4.1 Fabrication procedure	95
6.4.2 STEM sculpting of nanoribbons and nanopores	96
6.4.3 Device yield	97
6.4.4 Nanopore experiments	97
6.5 Supplementary information	98
6.5.1 Calculation of the graphene capacitance	103
6.5.2 Interpretation of the differential current signals	104
6.5.3 Interpretation of the common mode signals	105
References	108
<b>7. CONCLUSIONS AND RECOMMENDATIONS</b>	<b>113</b>
7.1 General challenges for nanopore measurements based on electrophoretic force	114
7.2 Considerations for graphene nanoribbon inplane current measurements	115
7.2.1 Signal-to-noise in the transverse current – where it all started	115
7.2.2 Some considerations for the device layout	116

7.2.3 Nanoscale size, damage, and yield – a trade-off	117
7.2.4 What about other 2D materials?	119
7.3 Outlook	120
<b>REFERENCES</b>	<b>121</b>
<b>SUMMARY</b>	<b>125</b>
<b>SAMENVATTING</b>	<b>129</b>
<b>CURRICULUM VITAE</b>	<b>135</b>
<b>LIST OF PUBLICATIONS</b>	<b>137</b>



# Preface

Sensors that enable fast and accurate detection of biomolecules can have unexpectedly powerful consequences for healthcare. Such sensors can potentially provide the knowledge on the current state of health of a human body, the disease a person is prone to get, and what treatment to pursue. They could facilitate non-invasive diagnosis of the majority of illnesses, including all known cancer variants. At this moment, we are crossing a frontier in the biological sciences that will hopefully bring us to an era where we will be able to access such biosensors, which will change the way we diagnose and treat people. And perhaps, ultimately, we might even be able to prevent people from getting sick.

DNA features four bases, A, T, C, and G, that align in a sequence that codes for all biomolecular processes in an organism. During the past 40 years, DNA sequencing has changed the way we study biology and practice medical science<sup>1</sup>. The technology has helped us to relate disease to certain genes, to understand the background of diseases, and it facilitates non-invasive diagnosis of illnesses<sup>2,3</sup>. Sequencing of the full genome maps the genetic heterogeneity among humans, which can be used to diagnose disease and to determine the right treatment to a patient in so-called personalized medicine. Now that the costs to sequence an individual human genome have lowered to \$ 1,000<sup>4</sup>, it is expected that the pace at which full genomes are mapped will take off at high pace. Similarly, the scientific fields related to data interpretation will flourish. Clearly, DNA sequencing is of tremendous value in biomedical sciences, and the amount of information that is to be extracted from it cannot yet be overseen.

Over the past decades, commercial sequencing technologies have continuously become faster and more affordable. However, the current ‘second-generation’ sequencing technologies, are somewhat limited as they require amplification steps and labeling, and suffer from error rates that increase with read-length. The ultimate sequencing technology would enable measurements on unlabeled and non-amplified DNA, it would be accurate, and it would not have any limitations regarding read-length<sup>1</sup>.

This thesis presents research that is underlying the development of biosensors that can read the genetic sequence of DNA at a single-molecule level. Solid-state nanopores provide a tool to detect one molecule at the time, without the need for labeling. Nanopores in graphene membranes, are of particular interest, as they can maximize the spatial resolution of the measurement, due to their atomic thickness. We explore the potential of graphene

---

nanopores to act as a platform for a future sequencing technology, and more specifically, how graphene's special electronic characteristics can be exploited.

Over the past 5 years, I have witnessed an impressive progress in the nanopore field. DNA sequencing with nanopores has been realized and commercialized, and numerous interesting biophysical studies have been reported. Excitingly, leading scientists in the field are now facing a great new challenge: single protein sequencing. What is the position of graphene in the nanopore field anno 2018? Graphene with its unique properties has a huge potential for DNA sequencing and biosensing. However, the relatively slow experimental progress in the graphene nanopore field does indicate that the work involves quite a few experimental challenges. The studies reported in this thesis do add some bits and pieces to the puzzle, and will hopefully guide future scientists in their exploration. Luckily, there is still so much to explore.

Stephanie J. Heerema  
March, 2018

1. Shendure, J. et al. DNA sequencing at 40: past, present and future. *Nature* **550**, 345–353 (2017).
2. Chiu, R. W. K. et al. Noninvasive prenatal diagnosis of fetal chromosomal aneuploidy by massively parallel genomic sequencing of DNA in maternal plasma. *Proc. Natl. Acad. Sci. U. S. A.* **105**, 20458–63 (2008).
3. Fan, H. C., Blumenfeld, Y. J., Chitkara, U., Hudgins, L. & Quake, S. R. Noninvasive diagnosis of fetal aneuploidy by shotgun sequencing DNA from maternal blood. *Proc. Natl. Acad. Sci. U. S. A.* **105**, 16266–71 (2008).
4. Wetterstrand, K. DNA Sequencing Costs: Data - National Human Genome Research Institute (NHGRI). (2017). Available at: <https://www.genome.gov/sequencingcostsdata/>.

## PREFACE

---





# 1

## GENERAL INTRODUCTION

## 1.1 DNA: FORM AND FUNCTION

DNA is the language of life<sup>1</sup>. It stores hereditary information in the form of a long polymer, built up of four different nucleotides, or 'DNA bases'. Each base consists of a nucleobase (adenine (A), thymine (T), cytosine (C) and guanine (G)), a sugar (deoxyribose), and a phosphate group. A strand of DNA is formed by covalent bonds between the sugar and the phosphate group of two neighboring nucleotides, leading to an alternating sugar-phosphate backbone (Fig. 1.1a). DNA bases can complementary pair through hydrogen bonds to form double stranded DNA (dsDNA) in a specific manner: A to T and C to G. The two chains fold into a right-handed helical structure, with the phosphate-sugar backbone on the outside, while the bases are stacked and folded to the inside (Fig. 1.1b)<sup>2</sup>.

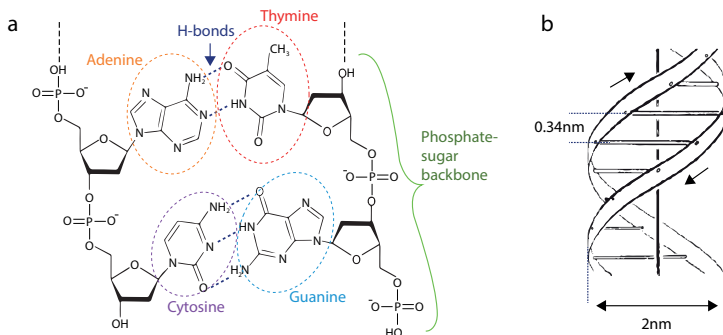


**Figure 1.1: The molecular structure of DNA.** (a) double stranded DNA chains are formed by alternating phosphate-sugar bonds making up the backbone, and basepairing of bases through hydrogen bonds. Only specific bases bind to each other; adenine to thymine by two hydrogen bonds and cytosine to guanine by three hydrogen bonds, leading to two complementary sequences of DNA. (b) Schematic image of the DNA helix as first eluded by Watson and Crick<sup>2</sup>. The two ribbons represent the phosphate-sugar backbone, and the horizontal bars the pairs of bases holding the chains together. The planes of the bases are perpendicular to the vertical axis.

The successive order of bases constitutes the DNA sequence. Segments of DNA sequences are known as genes, which code for RNA, which is synthesized in a process called transcription. RNA can be 'translated' into amino acids that build up proteins. Proteins fill up a wide range of functions within organisms. They act as building components, catalysts for reactions, they transport molecules, act as switches, etc. If proteins are the instrumentalists in an orchestra, the RNA is represented by the musical director who communicates the musical notes, i.e. the DNA, while the ensemble brings about the concert.

All genetic material of an organism is called the genome. The human genome contains about 3 billion bases, corresponding to approximately a meter in length, which is carefully folded in chromosomes in the nuclei of our cells, which are only several micrometers in size. The width of the dsDNA helix is 2nm, and the distance between two consecutive bases

is 0.34nm. Human DNA is surprisingly similar, only ~0.2% of our DNA determines our uniqueness<sup>3</sup>. Gene variations can potentially lead to disease. Genetic diseases are inherited, and can be expressed at any stage in life. Mutations can also appear *ad hoc*, during DNA synthesis, or due to exposure to external factors, such as chemicals or radiation. The vast majority of these mutations are repaired inside the cell. However, in some cases, mutations are transmitted to the daughter cells, and can in some cases cause disease, such as cancer. With the use of DNA sequencing, genetic variation can be tracked, and use the data to improve our understanding of life. An important application for humanity, is the early detection of diseases, by searching for mutations in genes. It also enables to improve our understanding of diseases and to treat patients better. Nanopores present a versatile tool to read the sequence of DNA molecules.

## 1.2 DNA SENSING WITH NANOPORES

The principle of nanopores is simple and elegant. A membrane separates two compartments containing an ionic solution, where a tiny hole (nanopore) represents the only passage for ions and molecules to travel from one side to the other. When an electric field is applied across the membrane, an ionic current emerges, and DNA which is highly negatively charged due to its phosphate-rich backbone, is pulled through the nanopore towards the positive electrode (Fig 1.2). During this translocation, the DNA molecule physically blocks part of the nanopore leading to a temporal change in the ionic current, which represents the sensing signal. Astoundingly, such measurements can even provide a direct electronic measurement of the slight volume differences between the DNA bases, and hence there is no need for labels and amplification. In addition, the technique can be scaled up to enable high-speed sequencing.

Nanopores were first used for sensing nucleic acids in the mid 1990s, using protein nanopores<sup>4,5</sup>. Since 2014, the technique has been successfully commercialized by Oxford Nanopore Technologies (ONT) and used in research labs across the world, and even in outer space<sup>6</sup>. The particular strength of the ONT Minion sequencer is that it allows to sequence relatively long read lengths (~10kb, and recently even 1 Mb), which enables mapping of highly repetitive DNA sequences<sup>7</sup>. Second, the possibility of *de novo* sequencing, combined with the portability of the device, facilitates fast diagnosis of rare genetic diseases and the screening of disease progression<sup>7</sup>. Using nanofabrication, nanopores can be artificially made of solid-state materials, introducing some nice advantages, such as chemical and thermal flexibility and a better rigidity of the membrane<sup>8,9</sup>. Moreover, the use of thin membranes could increase spatial resolution, possibly leading to a more accurate approach than what biological nanopores offer. Our lab has years of expertise in solid-state nanopores and has been using them for a huge variety of biophysical studies.

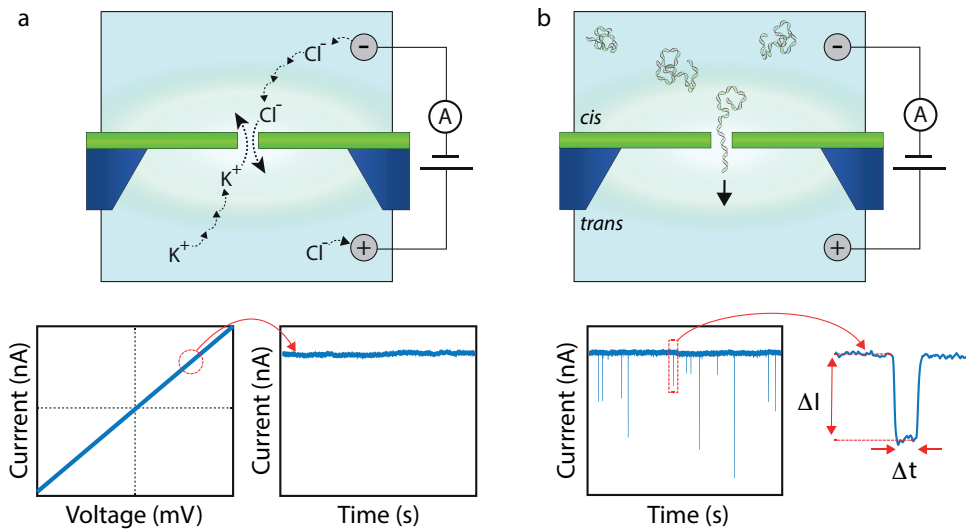


**Figure 1.2: The nanopore principle.** (a) A nanopore in a membrane is the only passage for ions and water molecules through the membrane. Application of a transmembrane potential triggers electrochemical reactions at the electrodes (typically Ag/AgCl), and causes ions to migrate through the nanopore giving rise to an ionic current. The current-voltage behavior is linear (Ohmic), a positive transmembrane voltage leads to a positive ionic current baseline in the order of nA. (b) Negatively charged DNA molecules on the ‘cis’ side of the membrane are driven through the nanopore towards the positive electrode on the ‘trans’ side. The translocation event causes a blockade in the ionic current (i.e. the signal), which is characterized by the current blockade magnitude ( $\Delta I$ ) and a translocation time ( $\Delta t$ ). [figure inspired from ref. 10].

DNA sequencing with solid-state nanopores has not yet been shown, as several challenges remain to be overcome. Firstly, the DNA molecules translocate through the nanopore very fast ( $\sim 1\text{-}10$  bases/ $\mu\text{s}$ ). Therefore, high-bandwidth measurements are needed ( $>10\text{MHz}$ ) to resolve the structural features of the molecule at the single-base level. Recent work has shown that a temporal resolution down to 100ns can be reached with a custom-built low-noise current amplifier<sup>11</sup>. However, the nanopore chip capacitance needs to be lowered, to further improve the signal-to-noise at these time scales, in order to resolve DNA base features. A second point of attention is the spatial resolution of the measurement, which is set by the thickness of the nanopore membrane. Ideally, only a single base moves through the nanopore at the same time, meaning that the membrane thickness should approach the scale of the DNA base-base separation on ssDNA ( $\sim 0.5\text{nm}$ ). Conventional solid-state nanopore membranes are 10-30nm thick, which implies that an ionic current signal originates from about 20-50 bases that simultaneously reside in the nanopore during DNA translocation. Graphene is, however, composed of a single layer of carbon atoms, organized in a two-dimensional hexagonal lattice (Fig. 1.3a), and with its single-atomic thickness, it could indeed maximize the spatial resolution of the measurement (Fig. 1.3b). Our group was the first to report DNA translocations through nanopores in graphene membranes<sup>12-14</sup>.

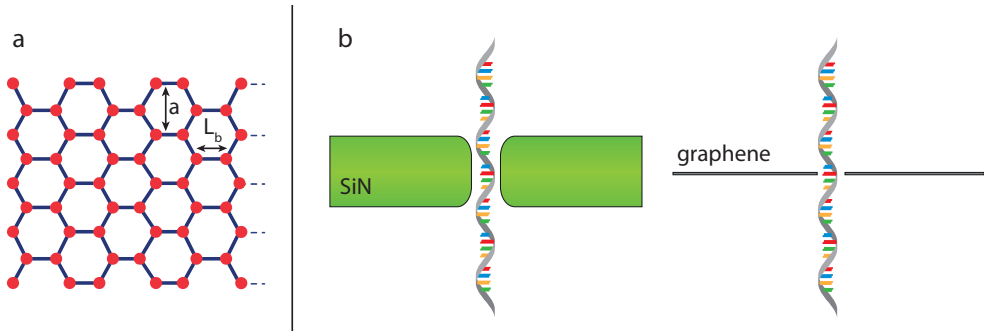


**Figure 1.3: Graphene as nanopore membrane.** (a) Graphene is composed of carbon atoms arranged in a 2-dimensional hexagonal lattice. The bond length between adjacent carbon atoms  $L_b = 1.42 \text{ \AA}$  and the lattice constant  $a = 2.46 \text{ \AA}$ . [figure adapted from ref. 17] (b) Scheme of a conventional solid-state nanopores (left) are made of SiN with a typical thickness of 10-30nm, hosting tens of DNA bases simultaneously. A graphene nanopore (right) has an effective thickness of approx. 0.6nm and can host a 1-2 basepairs at the same time, depicting a much higher spatial resolution.

### 1.3 GRAPHENE: A WONDERFUL MATERIAL

Next to its atomic thickness, graphene is the strongest material ever measured, it has interesting quantum properties, and it is an excellent electrical and thermal conductor<sup>15</sup>. Due to the many special properties of the material, the Nobel Prize in 2010 was awarded to the scientists that first achieved its isolation and characterization in 2004<sup>16</sup>. Its discovery was followed by the identification of many other two-dimensional materials, each having their own interesting properties. Since 2010, the graphene nanopore work took off, and interesting results have been reported.

Using graphene as the membrane for nanopore experiments on DNA, it was found that, as expected, the current signals in graphene pores were larger than those typically measured with SiN pores<sup>18</sup>. However, the ionic current baselines exposed significantly higher noise, which was shown to be reduced through the use of multiple layers or by reducing the area of freestanding graphene<sup>19</sup>. ssDNA interacts with graphene through  $\pi$ - $\pi$  stacking interactions, which led to an increase the translocation times of ssDNA<sup>20</sup>. In an opposite approach, ssDNA-graphene interactions were impeded by the rendering the graphene surface with a hydrophilic PEG coating<sup>21</sup>. Despite these improvements, the signal-to-noise in these measurements was too low to resolve any DNA sequence information. This triggered many theorists and experimentalists in the field to find new ways of detection while exploiting the special characteristics of graphene<sup>22</sup>.

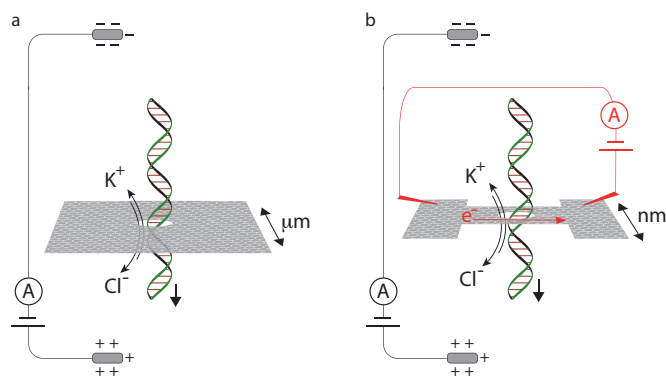


**Figure 1.4: Ionic current measurements and graphene inplane current measurements.** (a) DNA translocations through a nanopore in a freestanding sheet of graphene (typically of micrometer size) are detected in the ionic current. (b) DNA translocations through a nanopore in a nanometer-sized graphene nanostructure are detected in the ionic current and in the electric current through the nanostructure.

One of the first ideas proposed, involved the measurement of a tunneling current and its modulations across a graphene nanogap, whilst a DNA molecule moves vertically through the gap<sup>23</sup>. Theoretical studies, based on density functional theory (DFT) and non-equilibrium Green's function (NEGF), where transport across the nanogap was calculated in presence and absence of the DNA bases, indeed showed that the different DNA bases could be distinguished in that way<sup>24–30</sup>, although such measurements are challenging because of the difficulty in fabricating reproducible tunnel gaps. A second suggested idea, which caught our greatest interest, was the readout of an inplane current through a graphene nanoribbon with a nanopore within that ribbon. Also for this measurement layout, calculations predicted base-specific modulations in the current, due to the presence of DNA bases in the nanopore<sup>31–40</sup>. Nanoribbons are thin strips of graphene with a width of 1-100nm. A huge benefit of the graphene inplane current readout is that the magnitude of the current is substantially larger than the tunneling currents ( $\mu\text{A}$  versus  $\text{pA}$ ), which, in principle, enables high-frequency bandwidth detection, which is advantageous given the fast translocation speeds measured in solid-state nanopores<sup>41,42</sup>.

This thesis explores the feasibility and potential of that experiment, where both the ionic current through the nanopore and the inplane current through a graphene nanoribbon are measured, while DNA molecules translocate through the nanopore within that nanostructure (Fig. 1.4b).

#### 1.4 NANOPORES IN GRAPHENE NANORIBBONS

When the experiment was conceived, a number of requirements were listed in order to obtain the highest sensitivity for DNA in the devices. In that pursuit, we aimed to make as small as possible nanoribbons and nanopores, with limited amount of defects. Our group already closely collaborated with the Zandbergen group, who had developed expertise in high-temperature scanning transmission electron microscopy (STEM) to sculpt graphene nanostructures while retaining the materials' crystallinity<sup>43,44</sup>. We combined our efforts to gain expertise in the fabrication of freestanding nanostructures and use them for DNA detection.

STEM provides a unique tool as it enables patterning of graphene with true nanoscale precision. During sculpting, atoms are 'knocked out' of their lattice using a focused electron beam (with a spot size of 0.1nm), which occurs along a pre-defined path<sup>44</sup>. A second great advantage of the technique, is that defect generation can be limited by local heating of the graphene. At high temperatures, carbon ad-atoms on the graphene diffuse at high rates and instantly reoccupy vacancies in the lattice, preserving the crystallinity of the graphene. Additionally, high temperatures lead to graphene lattice recrystallization, or "self-repair"<sup>43-45</sup>. A challenge in the approach, is to prevent carbon deposition. Carbon atoms that are knocked out by the e-beam or originate from carbon-rich contaminations in the environment, can be deposited on the graphene surface near the illuminated area, leading to an unwanted layer of amorphous carbon at the critical areas (the edges of the structure or at the nanopore). However, this can be overcome by sculpting at high vacuum ( $\sim 10^{-8}$  mbar) and at high temperatures ( $>500^{\circ}\text{C}$ ). To heat the graphene to such temperatures, dedicated TEM 'heater chips' were made with platinum coils embedded in the SiN membrane<sup>46</sup>. Running a current through such a platinum coil results in a localized heating of the graphene membrane. A second approach to raise the temperature even more locally uses local Joule heating, where the platinum electrodes on the topside of the membrane were used to pass high current densities through the graphene nanostructure, to locally reach very high temperatures<sup>45</sup>.

A crucial step in the process, appeared to be the transfer of a thin layer of hexagonal boron nitride (h-BN) on top of the graphene nanostructure, to ensure that the nanopore is the only passage for DNA molecules during the DNA measurement. h-BN has a similar lattice to graphene, but is an insulator, which makes the material very suitable to fabricate stacks and sandwich-like structures with graphene in nanodevices<sup>47</sup>. The expected contrast levels for different flake thicknesses can be calculated to and used to determine the flake thickness of h-BN<sup>48,49</sup>. Material transfers on top of freestanding membranes, and particularly on top of suspended nanoribbons, can be difficult as these are prone to breaking. For the majority of transfers, the wedge transfer method was used to transfer exfoliated flakes to the target



chips<sup>50</sup>. This represents a powerful strategy as it facilitates the selection of thin flakes on a substrate wafer, it yields clean graphene and h-BN flakes, and it allows to transfer on top of fragile membranes, as no pressure is applied. The full workflow of the materials and methods used are described in detail in chapter 6.

## 1.5 THESIS OUTLINE

This thesis presents the work that is done in the pursuit of DNA translocation measurements with nanopores in graphene membranes and graphene nanoribbons.

### **Chapter 2:** ‘DNA sequencing with graphene nanodevices’.

This chapter reviews the four main concepts that are pursued in the field to use graphene to sequence DNA. These approaches involve the detection of ionic currents through nanopores in graphene membranes, tunneling currents across graphene nanogaps, inplane currents through graphene nanoribbons, and the physisorption of DNA molecules on graphene nanostructures. A perspective is given on the future of graphene for a new DNA sequencing technology.

### **Chapter 3:** ‘Controlling defects in graphene for optimizing the electrical properties of graphene nanodevices’.

Structural defects in the graphene play an important role for the quality of graphene-based nanodevices, as they can affect mechanical, chemical, electrical and optical properties. In this chapter, the different types of defects that exist in graphene are discussed, as well as their effect on the transport properties. Scanning transmission microscopy (STEM) provides a useful method to study defects as the material’s response to e-beam irradiation or local heating can be visualized.

### **Chapter 4:** ‘1/f noise in graphene nanopores’.

The ionic currents through graphene nanopores exhibit high noise levels, particularly in the low-frequency regime, which is characterized by a 1/f dependence. In chapter 4, an in-depth study on the noise and its relation to various parameters is presented, to gain an understanding of its origin. It is found that the 1/f noise can be lowered by increasing the flake thickness of graphene or boron nitride. The increased noise levels are proposed to be induced by mechanical fluctuations of the thin elastic two-dimensional membranes.

### **Chapter 5:** ‘Through-membrane electron-beam lithography for ultrathin membrane applications’.

Thin electron transparent windows are needed for in-situ TEM studies. However, nanofabrication on devices with freestanding membranes can be challenging as suspended sheets of material are prone to break. A technique is presented to make thin (down to 20nm) mem-

branes within thicker SiN membranes, without damaging the topside of the membrane. With the thin membranes, smaller areas of freestanding graphene could be suspended, which resulted in lower noise in the ionic currents through nanopores in graphene membranes.

**Chapter 6:** ‘Probing DNA translocations with inplane current signals in a graphene nanoribbon with a nanopore’.

This chapter discusses the core of this thesis, where the feasibility to detect DNA in the inplane current through a graphene nanoribbon, while DNA molecules translocate through a nanopore in the nanoribbon, is explored. High-temperature STEM is used to sculpt graphene nanoribbons and nanopores of the smallest scale with high conductivities. With the use of a home-built differential current amplifier, resistive modulations in the graphene current that originate from DNA-graphene interactions are decoupled from parasitic signals due to capacitive coupling.

**Chapter 7:** ‘Conclusions and Recommendations’.

In the last chapter of this thesis, I point out some considerations for the inplane current detection through graphene nanoribbons. In addition, advantages and disadvantages of different fabrication procedures are evaluated and the opportunities for other 2-dimensional materials are discussed.

## REFERENCES

1. Collins, F. S. *The Language of Life. DNA and the revolution in personalized medicine.* (Harper Collins, 2010).
2. Watson, J. D. & Crick, F. H. C. The structure of DNA. *Cold Spring Harb. Symp. Quant. Biol.* 18, 123–131 (1953).
3. McVean, G. A. et al. An integrated map of genetic variation from 1,092 human genomes. *Nature* 491, 56–65 (2012).
4. Bayley, H. *Nanopore Sequencing: From Imagination to Reality.* *Clin. Chem.* 61, 25–31 (2015).
5. Deamer, D., Akeson, M. & Branton, D. Three decades of nanopore sequencing. *Nat. Biotechnol.* 34, 518–524 (2016).
6. Jain, M., Olsen, H. E., Paten, B. & Akeson, M. The Oxford Nanopore MinION: delivery of nanopore sequencing to the genomics community. *Genome Biol.* 17, 239 (2016).
7. Jain, M. et al. Nanopore sequencing and assembly of a human genome with ultra-long reads. *bioRxiv* 128835 (2017).
8. Dekker, C. Solid-state nanopores. *Nat. Nanotechnol.* 2, 209–15 (2007).
9. Miles, B. N. et al. Single molecule sensing with solid-state nanopores: novel materials, methods, and applications. *Chem. Soc. Rev.* 42, 306–12 (2013).
10. Wanunu, M. Nanopores: A journey towards DNA sequencing. *Phys. Life Rev.* 9, 125–58 (2012).
11. Shekar, S. et al. Measurement of DNA Translocation Dynamics in a Solid-State Nanopore at 100 ns Temporal Resolution. *Nano Lett* 16, 4483–4489 (2016).
12. Schneider, G. F. et al. DNA translocation through graphene nanopores. *Nano Lett.* 10, 3163–7 (2010).
13. Merchant, C. A. et al. DNA translocation through graphene nanopores. *Nano Lett.* 10, 2915–21 (2010).
14. Garaj, S. et al. Graphene as a subnanometre trans-electrode membrane. *Nature* 467, 190–3 (2010).
15. Geim, A. K. & Novoselov, K. S. The rise of graphene. *Nat. Mater.* 6, 183–191 (2007).
16. Novoselov, K. S. et al. Electric field effect in atomically thin carbon films. *Science* 306, 666–9 (2004).
17. Schwierz, F. Graphene transistors. *Nat. Nanotechnol.* 5, 487 (2010).
18. Garaj, S., Liu, S., Golovchenko, J. A. & Branton, D. Molecule-hugging graphene nanopores. *Proc. Natl. Acad. Sci. U. S. A.* 110, 12192–6 (2013).
19. Heerema, S. J. et al.  $1/f$  noise in graphene nanopores. *Nanotechnology* 26, 74001 (2015).
20. Banerjee, S. et al. Slowing DNA Transport Using Graphene-DNA Interactions. *Adv. Funct. Mater.* 25, 936–946 (2014).
21. Schneider, G. F. et al. Tailoring the hydrophobicity of graphene for its use as nanopores for DNA translocation. *Nat. Commun.* 4, 2619 (2013).
22. Heerema, S. J. & Dekker, C. Graphene nanodevices for DNA sequencing. *Nat. Nanotechnol.* 11, 127–136 (2016).
23. Postma, H. W. C. Rapid sequencing of individual DNA molecules in graphene nan-

- ogaps. *Nano Lett.* 10, 420–5 (2010).
24. Zhao, Q. et al. Nanopore-Based DNA Analysis via Graphene Electrodes. *J. Nanomater.* 2012, 1–5 (2012).
  25. Zhang, H. et al. Detection of nucleic acids by graphene-based devices: A first-principles study. *J. Appl. Phys.* 115, 133701 (2014).
  26. Prasongkit, J., Grigoriev, A., Pathak, B., Ahuja, R. & Scheicher, R. H. Transverse conductance of DNA nucleotides in a graphene nanogap from first principles. *Nano Lett.* 11, 1941–5 (2011).
  27. Prasongkit, J., Grigoriev, A., Pathak, B., Ahuja, R. & Scheicher, R. H. Theoretical Study of Electronic Transport through DNA Nucleotides in a Double-Functionalized Graphene Nanogap. *J. Phys. Chem. C* 117, 15421–15428 (2013).
  28. He, Y. et al. Enhanced DNA Sequencing Performance Through Edge-Hydrogenation of Graphene Electrodes. *Adv. Funct. Mater.* 21, 2674–2679 (2011).
  29. Pedersen, J. N., Boynton, P., Ventra, M. Di, Jauho, A.-P. & Flyvbjerg, H. Classification of DNA nucleotides with transverse tunneling currents. *Nanotechnology* 28, 15502 (2017).
  30. Amorim, R. G., Rocha, A. R. & Scheicher, R. H. Boosting DNA Recognition Sensitivity of Graphene Nanogaps through Nitrogen Edge Functionalization. *J. Phys. Chem. C* 120, 19384–19388 (2016).
  31. Nelson, T., Zhang, B. & Prezhd, O. V. Detection of nucleic acids with graphene nanopores: ab initio characterization of a novel sequencing device. *Nano Lett.* 10, 3237–42 (2010).
  32. Ouyang, F.-P., Peng, S.-L., Zhang, H., Weng, L.-B. & Xu, H. A biosensor based on graphene nanoribbon with nanopores: a first-principles devices-design. *Chinese Phys. B* 20, 58504 (2011).
  33. Saha, K. K., Drndić, M. & Nikolić, B. K. DNA base-specific modulation of microapere transverse edge currents through a metallic graphene nanoribbon with a nanopore. *Nano Lett.* 12, 50–5 (2012).
  34. Avdoshenko, S. M. et al. Dynamic and electronic transport properties of DNA translocation through graphene nanopores. *Nano Lett.* 13, 1969–76 (2013).
  35. Girdhar, A., Sathe, C., Schulten, K. & Leburton, J.-P. Graphene quantum point contact transistor for DNA sensing. *Proc. Natl. Acad. Sci. U. S. A.* 110, 16748–53 (2013).
  36. Ahmed, T., Haraldsen, J. T., Zhu, J.-X. & Balatsky, A. V. Next-Generation Epigenetic Detection Technique: Identifying Methylated Cytosine Using Graphene Nanopore. *J. Phys. Chem. Lett.* 5, 2601–2607 (2014).
  37. Sadeghi, H. et al. Graphene sculpturene nanopores for DNA nucleobase sensing. *J. Phys. Chem. B* 118, 6908–14 (2014).
  38. Ahmed, T. et al. Correlation dynamics and enhanced signals for the identification of serial biomolecules and DNA bases. *Nanotechnology* 25, 125705 (2014).
  39. Paulechka, E., Wassenaar, T. A., Kroenlein, K., Kazakov, A. & Smolyanitsky, A. Nucleobase-functionalized graphene nanoribbons for accurate high-speed DNA sequencing. *Nanoscale* 8, 1861–1867 (2016).
  40. De Souza, F. A. L., Amorim, R. G., Scopel, W. L. & Scheicher, R. H. Electrical detection of nucleotides via nanopores in a hybrid graphene/h-BN sheet. *Nanoscale* 9,

- (2017).
41. Han, S.-J. et al. High-Frequency Graphene Voltage Amplifier. *Nano Lett.* 11, 3690–3693 (2011).
  42. Petrone, N., Meric, I., Hone, J. & Shepard, K. L. Graphene Field-Effect Transistors with Gigahertz-Frequency Power Gain on Flexible Substrates. *Nano Lett.* 13, 121–125 (2013).
  43. Song, B. et al. Atomic-scale electron-beam sculpting of near-defect-free graphene nanostructures. *Nano Lett.* 11, 2247–50 (2011).
  44. Xu, Q. et al. Controllable atomic scale patterning of freestanding monolayer graphene at elevated temperature. *ACS Nano* 7, 1566–72 (2013).
  45. Qi, Z. J. et al. Electronic transport of recrystallized freestanding graphene nanoribbons. *ACS Nano* 9, 3510–20 (2015).
  46. Neklyudova, M. et al. Through-membrane electron-beam lithography for ultrathin membrane applications. *Appl. Phys. Lett.* 111, (2017).
  47. Dean, C. R. et al. Boron nitride substrates for high-quality graphene electronics. *Nat. Nanotechnol.* 5, 722–6 (2010).
  48. Blake, P. et al. Making graphene visible. *Appl. Phys. Lett.* 91, 63124 (2007).
  49. Gorbachev, R. V. et al. Hunting for Monolayer Boron Nitride: Optical and Raman Signatures. *Small* 7, 465–468 (2011).
  50. Schneider, G. F., Calado, V. E., Zandbergen, H., Vandersypen, L. M. K. & Dekker, C. Wedging transfer of nanostructures. *Nano Lett.* 10, 1912–6 (2010).





# 2

## GRAPHENE NANODEVICES FOR DNA SEQUENCING

**F**ast, cheap, and reliable DNA sequencing could be one of the most disruptive innovations of this decade, as it will pave the way for personalized medicine. In pursuit of such technology, a variety of nanotechnology-based approaches have been explored and established, including sequencing with nanopores. Owing to its unique structure and properties, graphene provides interesting opportunities for the development of a new sequencing technology. In recent years, a wide range of creative ideas for graphene sequencers have been theoretically proposed and the first experimental demonstrations have begun to appear. Here, we review the different approaches to using graphene nanodevices for DNA sequencing, which involve DNA passing through graphene nanopores, nanogaps, and nanoribbons, and the physisorption of DNA on graphene nanostructures. We discuss the advantages and problems of each of these key techniques, and provide a perspective on the use of graphene in future DNA sequencing technology.

---

This chapter has been published as:  
Stephanie J. Heerema and Cees Dekker, *Nature Nanotechnology*, 11, 127 (2016)



## 2.1 INTRODUCTION

DNA sequencing is an extremely rapidly evolving methodology to read off the sequence of bases in a genome. Given its role in human physiology and development, such sequence information is expected to significantly impact diagnosis and treatment of disease, ultimately facilitating personalized medicine where the right treatment can be applied to individuals. The progress towards cheaper and faster sequencing has been very impressive since the Human Genome Project<sup>1</sup> first sequenced the human genome. That project was largely carried out using the classical Sanger method<sup>2</sup>, a process in which DNA strands are synthesized starting from a known primer sequence and terminated by a specific dideoxy deoxyribonucleoside triphosphate (dNTP), such that the last base in the sequence is known. DNA strands are then size separated by gel electrophoresis for reading off that last base. The Sanger procedure is time consuming due to the slow throughput with DNA fragment separation in gels. The need for cheaper and faster techniques drove both scientists and companies to work on new sequencing technologies<sup>3,4</sup>. Second-generation sequencers involved in vitro amplification of DNA strands and their clustering onto dedicated surfaces as well as sequencing by synthesis<sup>5</sup>, where fluorescently tagged nucleotides are added by a polymerase, which enables a signal for each base to be instantly read off. These improvements substantially increased the degree of parallelism and reduced reagent volumes, leading to much faster and cheaper sequencing. These methods, however, came at the cost of significantly lower read lengths (typically ~100 bp) compared with the Sanger method (>500 bp)<sup>6</sup>.

Yet newer sequencing methods, based on nanotechnology approaches, now focus on single-molecule long-read-length sequencing without any amplification or labelling. For example, Pacific Biosciences uses an array of zero-mode waveguides where each waveguide reads the base sequence by detecting the incorporation of single fluorescent nucleotides in DNA synthesis in real time<sup>7</sup>. This technology is particularly useful for de novo sequencing, as it allows long strands (on average several kbp long) to be read. Although sizeable error rates (~13%) have been reported<sup>8</sup>, these errors are random, in contrast to context-specific errors (for example, palindromic sequences or GC-rich contents) that are generally observed in other techniques, such that multiple lower-quality base calls can be aligned to derive high-quality (de novo) sequence data<sup>9,10</sup>. Another interesting innovation recently emerged from Oxford Nanopore Technologies that built a sequencing device based on biological nanopores<sup>11</sup>. In such nanopore sequencing, one detects the base-dependent changes in the ionic current while a DNA molecule passes through the pore. This powerful technique allows for amplification- and label-free detection that can be scaled up for high-throughput sequencing. The technology was even developed into a portable device that could be ideal for direct use in health centres. First studies report that high-confidence alignments can resolve single-nucleotide variations and that the base reads are up to 85% accurate (that is, they have a very large 15% error on each base calling, but the accuracy

seems to be improving rapidly)<sup>12</sup>. Further development towards next-generation sequencing devices is eagerly awaited, and there is a need for new approaches.

Graphene, a single layer of carbon atoms arranged in a 2D hexagonal lattice, is providing new opportunities. Since its discovery in 2004<sup>13,14</sup>, interest in this material has increased dramatically<sup>15</sup> due to the fact that it combines a number of unique properties: it is atomically thin, stronger than steel<sup>16</sup>, highly flexible<sup>17</sup>, stretchable, and transparent<sup>18</sup>, has tunable optical properties<sup>19</sup>, is impenetrable to ions, and is an excellent thermal<sup>20</sup> and electrical conductor. It has attracted major attention for electronic applications due to its extremely high charge carrier mobilities, even at room temperature ( $1 \times 10^5 \text{ cm}^2 \text{ V}^{-1} \text{ s}^{-1}$ )<sup>21</sup>. Graphene can be produced cheaply in large areas, thus allowing upscaling in a cost-efficient manner. Given the special properties of graphene and its wide range of potential applications<sup>22</sup>, one may ask whether graphene provides novel opportunities for nanodevices for DNA sequencing. Indeed, this is the case, and this is the focus of this Review.

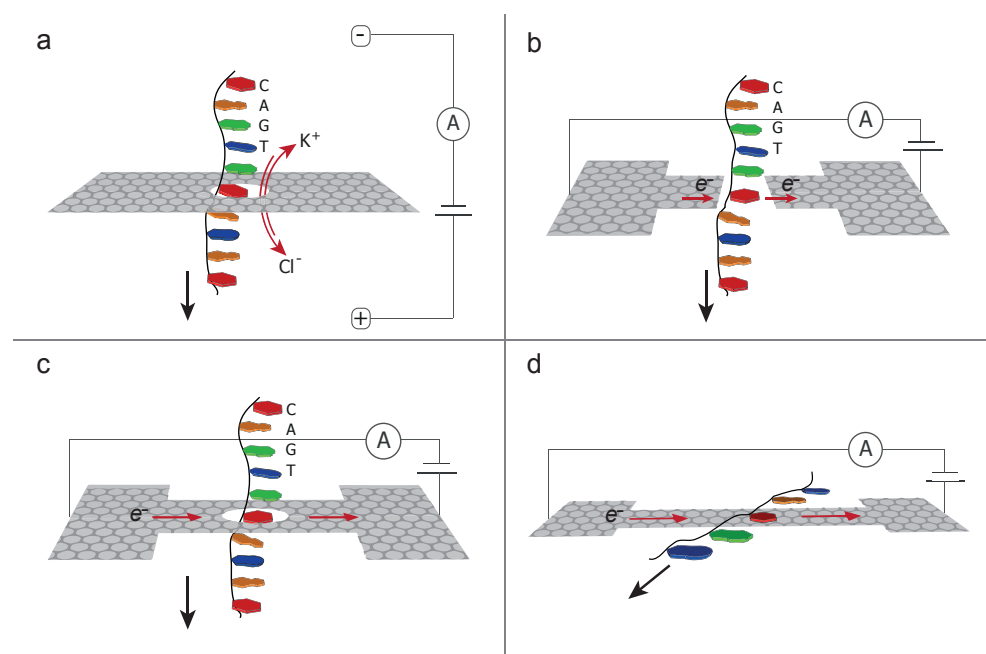


**Figure 2.1: Four new concepts using graphene nanostructures for DNA sequencing.** (a) Detection of changes in the ionic current through a nanopore in a graphene membrane due to the passage of a DNA molecule. (b) Modulations of a tunnelling current through a nanogap between two graphene electrodes due to presence of a DNA molecule. (c) Variations in the inplane current through a graphene nanoribbon due to traversal of a DNA molecule. (d) Changes in a graphene current due to the physisorption of DNA bases onto the graphene.

2 | Many different concepts have recently been proposed to sequence DNA using the special properties of graphene, as summarized in Fig. 2.1. Graphene's atomically thin and ion-impermeable structure, for example, represents the ultimate membrane for nanopore-based sequencing (Fig. 2.1a), where each base of a DNA molecule will block the ionic current through a tiny nanopore in the thin graphene sheet slightly differently. Other innovative proposals employ graphene's conductive properties. As shown in Fig. 2.1b, each base residing within a nanosize gap within a graphene layer may lead to a different tunnelling current across the gap because of the different electronic level structure of the bases. Alternatively, one can monitor the inplane current through a graphene nanoribbon with a nanopore through which a DNA molecule traverses (Fig. 2.1c), as different bases are predicted to modulate the nanoribbon current differently. Finally, a range of techniques rely on changes in graphene currents as a result of physisorption of DNA to the graphene surface (Fig. 2.1d). This Review provides an overview of the various theoretical proposals for graphene-based DNA sequencing and discusses the first experimental efforts in this direction.

As DNA is strongly negatively charged, it can be driven in a head-to-tail fashion through the nanopore by an electric field. While the molecule translocates, it excludes ions from the pore volume, resulting in a temporal decrease in the ionic current. The magnitude and the duration of the current blockade provide information on the diameter and length of the molecule, respectively. For sequencing, each nucleotide should block the ionic current in a unique way that is dependent on its molecular size and shape. Nanopore sequencing is pursued with biological and solid-state nanopores.

Biological nanopores in cell membranes control the transport of molecules from one compartment to the other, and researchers have studied these systems for decades by measuring ion transport<sup>23</sup> and polymer translocations<sup>24,25</sup>. Nucleic acid translocations through  $\alpha$ -haemolysin pores in lipid membranes were measured nearly two decades ago<sup>26</sup>, motivated by the idea to read the consecutive bases of single-stranded DNA molecules in a linear fashion. Since these early days, the nanopore field has grown tremendously, and excitingly, DNA sequencing with nanopores has indeed been realized<sup>27,28</sup>. Solid-state nanopores present some interesting advantages over their biological counterparts, such as high stability, control over pore diameter and channel length, lower sensitivity to external parameters such as pH, temperature, salt concentration, and mechanical stress, and, importantly, they are well suited for massive upscaling and device integration on chip<sup>29</sup>. However, solid-state nanopores also have some disadvantages, such as the lack of true atomic control and increased noise levels. Indeed, so far, DNA sequencing has been realized with biological nanopores, but not yet with solid-state nanopores.

One of the most fascinating new developments has been the employment of graphene

nanopores for DNA sequencing. Even monolayer graphene is impermeable to ions, and due to its strength, graphene can form a freestanding membrane, facilitating the ideal atomically thin membrane for nanopore measurements. The sensing resolution of monolayer graphene has the potential to attain its theoretical optimum, as the effective thickness of the graphene is only  $\sim 0.6$  nm in solution due to ionic screening<sup>30,31</sup>, which is the same length scale as the distance between two adjacent bases ( $\sim 0.6$  nm) of a single-stranded DNA molecule. Although it is not yet known whether single-base resolution can be achieved, this could highly simplify signal processing. This would present a significant advantage compared with the longer pore channels that are present in conventional silicon nitride pores and in protein pores, where complex signal deconvolution and processing is needed, because the ionic signal originates from several neighboring nucleotides in the relevant volume of the pore. Another important advantageous property of graphene is that it is electrically conductive, which opens up the possibility to monitor an inplane current through the membrane when the DNA molecule translocates.

Theorists have studied whether indeed DNA sequencing is possible with ionic current detection through graphene nanopores. Molecular dynamics simulations have been performed to study the movement of DNA molecules through a graphene pore, to evaluate in what way this affects the ionic current<sup>32-34</sup>. Early on, it was found that poly(AT) and poly(GC) can be distinguished at a bias voltage of 1 V (ref. 32). However, the simulations also exposed some problems with the approach, as they revealed that the bases move stochastically through the pore, which would lead to sequencing errors. Also, the current blockades were predicted to be strongly dependent on the local conformation of the DNA bases inside the pore resulting in a strong overlap of the current blockades for the different bases<sup>32,33</sup>. Interestingly, hydrophobic adhesion of bases to the graphene surface right next to the pore was found to significantly reduce the possible single-stranded DNA conformations<sup>33</sup>. These simulations suggested that the best 'stepwise' translocations may occur with a three-layer graphene sheet, such that collective binding and unbinding of the bases on both sides of the membranes is possible, while fluctuations in the DNA base orientations inside the pore are minimized<sup>33</sup>.

In 2010, three independent groups published experimental data of double-stranded DNA translocations through graphene nanopores<sup>30,35,36</sup>. Their approaches were equivalent: 525-nm-diameter pores (Fig. 2.2a,b) were made with a transmission electron microscope in a freestanding graphene membrane on top of a larger hole in a silicon nitride membrane. A large current blockade (that is, the DNA sensor signal) was measured for DNA translocations compared with conventional silicon nitride solid-state pores due to the atomically thin membrane<sup>30,36</sup> (Fig. 2.2c). The signal amplitude was shown to be further maximized by minimizing the pore diameter<sup>31</sup>. In a next step towards sequencing, single-stranded

DNA was detected. To do so, the attractive hydrophobic  $\pi$ - $\pi$  stacking interactions between the nucleobases and graphene were overcome by applying a hydrophilic coating to the graphene to prevent attachment of the DNA to the graphene and the associated clogging of the pore<sup>37</sup>. In another experimental report, the opposite approach was taken and the adsorption and desorption of DNA bases on the graphene was in fact exploited to slow down DNA during translocation. Indeed, longer translocation times were found for single-stranded DNA ( $\sim 5.5 \mu\text{s nt}^{-1}$ ) compared with double-stranded DNA ( $\sim 0.4 \mu\text{s bp}^{-1}$ ) in a graphene/ $\text{Al}_2\text{O}_3$ /graphene sandwich device (Fig. 2.2d), where the slower translocation is likely to be caused by a stick-slip interaction<sup>38</sup>.

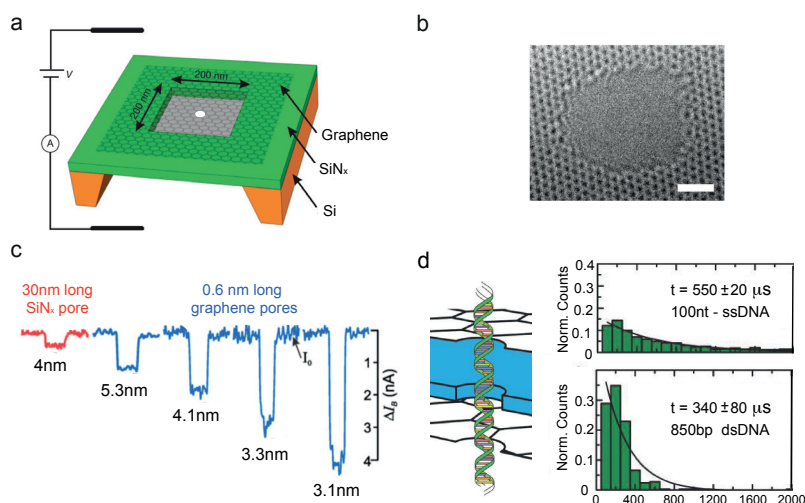


**Figure 2.2: DNA detection with ionic current measurements through graphene nanopores.** (a) Schematic of a typical graphene nanopore device layout, where a small nanopore is created in a graphene membrane that is freestanding over a hole (100–1,000 nm; a  $200 \times 200$  nm aperture is shown in the figure) in a silicon nitride membrane on a silicon chip. (b) Transmission electron microscopy (TEM) image (80 kV) of a 3 nm nanopore with clean and crystalline edge drilled in STEM mode at 600 °C. Scale bar, 1 nm. (c) Double-stranded DNA current blockades (IB) are larger for graphene nanopores (blue) than for SiNx pores (red) due to their thin membranes. The largest blockade signals were measured with the smallest pores of  $\sim 3$  nm.  $I_0$  is the open pore current. (d) Single-stranded DNA (ssDNA) translocations through nanopores in a membrane of stacked layers of graphene/ $\text{Al}_2\text{O}_3$ /graphene have shown that ssDNA does translocate slower than double-stranded DNA (dsDNA) due to interactions between the aromatic groups in the DNA bases and the graphene. Figures adapted with permission from: a, ref. 30, Nature Publishing Group; b, ref. 37, Nature Publishing Group; c, ref. 31, NAS; d, ref. 38, Wiley.

A general challenge for DNA sequencing with solid-state nanopores is the fast translocation time of the DNA molecules, which typically traverse the pore at a speed of 0.01–1.00  $\mu\text{s}$  per base depending on the conditions, which is orders of magnitude too fast given that measurements are generally performed at a bandwidth of only  $\sim 100$  kHz, which is limited

by the high noise in the ionic current<sup>39</sup>. Also, the DNA molecule's movement is not completely confined, leading to positional fluctuations and variation in translocation velocity<sup>40</sup>. As temporal signals are interpreted into spatial information, this could be a serious problem for ionic current detection. Graphene nanopores particularly exhibit high low-frequency 1/f noise, which is probably of mechanical origin<sup>41</sup>. It may be possible to suppress this noise by reducing the area of the freestanding graphene<sup>31</sup>, or by the use of multilayered structures<sup>36,42,43</sup>. Glass-based substrates may furthermore represent a good improvement, as low dielectric materials reduce the capacitive noise<sup>44</sup>.

The solid-state nanopore field is still pushing towards base-discriminating measurements on DNA molecules that move through the pore more slowly, and graphene pores may contribute to these technical advances. It, however, remains a significant challenge to reach single-base resolution given the fast translocation times, the conformational fluctuations, the stochastic translocation of the bases, and the high noise levels. Various groups now look for alternative read-out schemes that are different from ionic current detection, by utilizing the intrinsic conductivity of graphene, as explained below.

### 2.3 TUNNELLING ACROSS A GRAPHENE NANOGAP

We will now discuss DNA sequencing based on tunnelling across a graphene nanoslit. The concept is to measure a tunnelling conductance across two closely spaced graphene electrodes, and to monitor the variations of the current as a DNA molecule passes through the slit. Transmission spectra for tunnelling electrons depend on the electronic structure of the nucleotide and on the coupling of the nucleotide eigenstates to the graphene edges. A distinctive tunnelling current will be observed when the molecular energy level of a base falls within the voltage bias window of the two electrodes. When the molecular eigenlevels are far away from the electrochemical potentials of the graphene edges, tunnelling will be off-resonant and the tunnelling currents will be small. Graphene can be particularly useful in this set-up, because its single-atom thickness facilitates the detection of a single nucleotide that resides in the tunnelling gap. And perhaps most importantly, graphene can represent both the membrane and the electrodes at the same time because of its electrical properties. This greatly eases the fabrication of devices, as the nanogap and the electrodes are automatically aligned in the same plane (Fig. 2.3a)<sup>45</sup>.

This idea was first proposed in 2010, with numerical simulations showing that sequencing should be possible for small gap sizes (1–2 nm)<sup>45</sup>. Similarly, simulations for graphene electrodes embedded within a silicon nitride nanopore reported base-specific detection<sup>46</sup>. Density functional theory (DFT) and non-equilibrium Green's function (NEGF) studies were utilized to study how transport across graphene nanoslits is modulated due to the presence of DNA bases in the slit. Indeed, a DFT–NEGF study on a gap in a zigzag-edged graphene nanoribbon, which is a nanostructured narrow graphene strip with perfect zigzag edges

(Fig. 2.3b), predicted the possibility of base discrimination<sup>47</sup>. However, another study indicated that only the G base can be well distinguished from the other three due to quantum interference effects<sup>48</sup> that may occur from the rotation of bases and due to Fano-type resonances caused by energetic coupling between the discrete energy state of the DNA base and the continuous energy states of the graphene electrode.

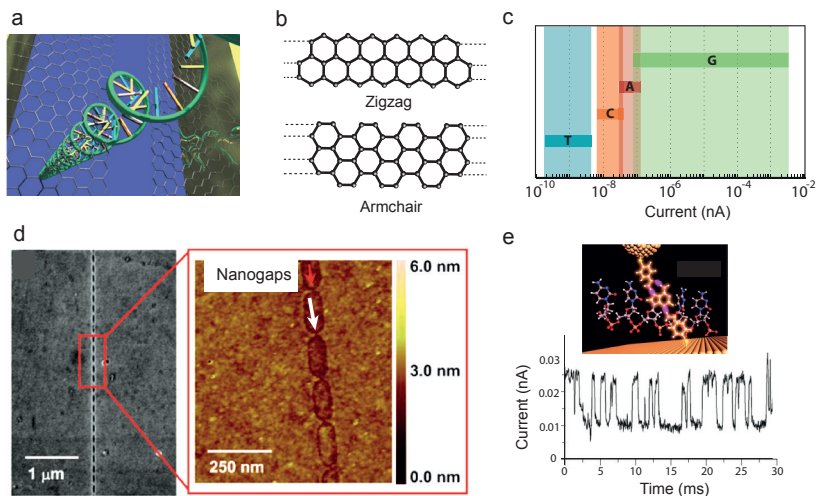


**Figure 2.3: Graphene nanogaps for DNA sequence detection.** (a) Artist's impression of a single-stranded molecule (backbone in green, bases in alternating colours) that translocates through a gap in graphene. (b) Schematic image of two different edge geometries of graphene: zigzag and armchair. (c) Theoretical calculations predict that the four DNA bases can be distinguished from the tunnelling currents across a graphene nanogap. The currents are very small ( $10^{-10}$ – $10^{-3}$  nA) and are widely spread, but show little overlap. (d) Scanning electron microscopy (left) and atomic force microscopy (right) images of an array of graphene gaps (1–10 nm) on silicon dioxide made with electron beam lithography and oxygen plasma etching. (e) Left: Artist's impression of tunnelling electrodes functionalized with recognition agents (benzamide groups) that bind to a single DNA base in the centre. Right: Current spikes produced when deoxyadenosine 5'-monophosphate (dAMP) nucleotides were introduced between the tunnelling electrodes. Figures adapted with permission from: (a) ref. 45, American Chemical Society; (c) ref. 49, American Chemical Society; (d) ref. 64, Wiley; (e) ref. 52, Nature Publishing Group.

As the tunnelling current is exponentially sensitive to changes in distance and orientation, large fluctuations in the tunnelling currents can be expected<sup>45,48–50</sup>. The tunnelling current distributions for the four DNA bases are therefore predicted to be broad (variations over orders of magnitude), yet with little overlap (Fig. 2.3c)<sup>49</sup>. Functionalization of the electrodes, for instance by hydrogenation or by attachment of one of the nucleobases, may provide a way to hold the molecule in a preferred orientation relative to the electrodes, thereby significantly reducing current fluctuations. Such passivation of the electrode edges is also suggested to promote coupling<sup>50,51</sup>, and it may slow down the translocation speed of the

DNA, allowing more time for measuring each individual base<sup>50</sup>. The idea of this ‘recognition tunnelling’ originates from successful experiments performed to slow down DNA while it moves through a gap<sup>52–54</sup> (Fig. 2.3e). Many efforts were focused on measuring DNA with metallic tunnelling electrodes embedded in silicon nitride pores<sup>52,55–59</sup>, and indeed, some sequence information could be extracted when the DNA was pulled through the gap by an electric field<sup>56,57</sup>.

So far, no DNA sequencing experiments using tunnelling through graphene gaps have been reported. However, stable nanogaps of 1–2 nm in few-layer graphene were formed through feedback-controlled electroburning, where heat due to the high current densities locally burns the graphene, and transport through contacted single molecules between the electrodes was measured<sup>60–62</sup>. Other approaches involved beam-based techniques such as helium ion beam lithography<sup>63</sup>, and arrays of graphene nanogaps (1–10 nm) were fabricated using electron beam lithography and oxygen plasma etching (Fig. 2.3d)<sup>64</sup>. There are some significant challenges for this approach, as the tunnelling currents will be small due to the low density of states in graphene, fluctuations will be large due to base fluctuations (position and orientation), and the Brownian motion of ions and water molecules may induce additional noise. Furthermore, as the DNA is electrophoretically driven through the gap, its translocation speed will again be very high, which will make it even more difficult to resolve sequence information. Nevertheless, in view of the promising theoretical proposals and the successes made with fabricating tunnelling electrodes embedded in solid-state nanopores, interesting experimental results on DNA detection using graphene nanogaps may be expected in the near future.

#### 2.4 INPLANE TRANSPORT OF A GRAPHENE NANORIBBON WITH A NANOPORE

The electrical properties of graphene can be exploited in a more direct way for DNA sequencing by monitoring the current through a narrow graphene nanostructure that contains a nanopore through which a DNA molecule translocates. Graphene is a gapless semiconductor<sup>65</sup>, but when structuring the graphene into a nanometer-sized ribbon, its properties change depending on the edge profiles. Theoretical studies show that an armchair ribbon will be semiconducting<sup>66–69</sup> and that a zigzag-edged ribbon is metallic with a current profile that peaks at the edges<sup>66,69–71</sup>. Both armchair and zigzag nanoribbons have been proposed to present promising platforms for DNA sequencing in a large number of theoretical reports<sup>72–79</sup>, and experimentalists have begun to explore this approach<sup>80–85</sup>.

Similar results were obtained from various theoretical calculations, where electronic transport was studied using DFT and NEGF for different types of ribbon (width ~3 nm and pore diameter ~1.5 nm) in the absence and presence of each of the four DNA nucleobases<sup>72–79</sup>. The nanoribbon current was found to be modulated due to electrostatic interactions between the nucleotides and the graphene pore, causing a change in the local density of



states in the graphene near the pore. Base specificity (that is, different nanoribbon currents when different bases are inserted in the pore) is attributed to the different coupling strengths of the bases with the graphene nanoribbon.

The first DFT study on a graphene nanoribbon with a nanopore was published in 2010<sup>72</sup>, where the authors calculated the current through a hydrogen-terminated armchair ribbon with a nanopore. By integrating over the density of states in the presence and absence of the respective DNA bases, this device could discriminate between the four different bases, a result that was found to be insensitive to strand orientation relative to the membrane. Similar calculations were done on a metallic nanoribbon<sup>73</sup>, where the location of the pore was varied between the middle and the edge of the ribbon, and it was proposed that a ribbon with a pore located at the edge will be more suitable for DNA detection. Calculations have shown that edge currents in zigzag ribbons may be beneficial for DNA detection<sup>74,86</sup> (Fig. 2.4a). Base-distinct current variations were found, on the order of  $\sim 1 \mu\text{A}$  at 100 mV bias, much larger than what can be expected for armchair-edged ribbons where these edge currents are absent. These results were, however, contradicted by a self-consistent DFT study on zigzag-edged graphene nanoribbons<sup>75</sup> that showed that the respective bases can only be distinguished when transport is conducted away from the Fermi level. In another interesting study, nanoribbons with a finite width were compared with quantum point contact structures, which essentially are ribbons in the limit of zero width<sup>76</sup>. These point contacts were found to exhibit a greater sensitivity than armchair-edged ribbons provided that the carrier density is enhanced, for example by gating<sup>76</sup>.

Another more complex device, consisting of two nanoribbons stacked on top of one another to form a small overhang ( $\sim 3 \text{ nm}$ ) with a nanopore ( $\sim 1.5 \text{ nm}$  diameter)<sup>78</sup>, yielded again base discrimination. Calculations performed on multilayered structures that facilitate multiple measurements on the same molecule, showed that a cross-correlation analysis between different nanopore scans of the same DNA molecule can yield an enhanced signal-to-noise ratio<sup>79</sup>. Graphene nanoribbons with a nanopore were also proposed to be able to distinguish whether DNA is methylated or not, a crucial biomarker for epigenetics. Methylated and non-methylated bases were shown to lead to characteristic differences in transport through a graphene nanoribbon with a 0.5-nm-wide hydrogenated pore<sup>77</sup>.

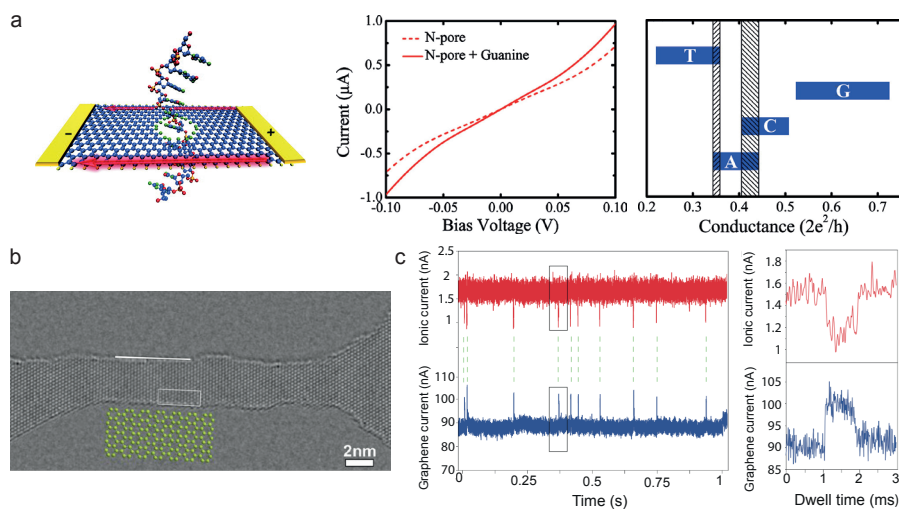


**Figure 2.4: Graphene nanoribbons with a nanopore for DNA sequencing.** (a) Left: Schematic view of a metallic zigzag graphene nanoribbon with a nanopore, where current flows mostly around the zigzag edges (red arrows). Middle: A guanine DNA base in the nanopore is shown to induce a (base-specific)  $\sim\mu\text{A}$  modulation of the edge current. Right: The four different bases yield very different current modulations. Variations in base rotation result in a spread of the conductance modulations. Shaded areas mark the regions of overlap. (b) TEM image of a nanoribbon in monolayer graphene, sculpted at 300 keV at 600 °C and imaged at 80 keV at 600 °C. The graphene was heated to preserve the single crystallinity. The white line indicates an armchair edge. The atomic structure model of the armchair edge highlighted by the white rectangle is shown by the green dots. (c) Simultaneously recorded ionic current (red) and electrical current (blue) through a  $\sim 100\text{-nm}$ -wide graphene nanoribbon with a 10 nm pore during translocations of double-stranded DNA (graphene source-drain voltage 20 mV). Zoomed-in views of correlated event highlighted by black rectangles are shown in panels on the right. Figures adapted with permission from: a, ref. 74, American Chemical Society; b, ref. 85, American Chemical Society; c, ref. 80, NPG.

Although the results of these theoretical studies are exciting, it has to be noted that most calculations on nanoribbons and on nanogaps were performed on simple model systems. The effect of ions and solvent molecules were typically not included and the DNA phosphate backbone was often assumed to be neutral in charge. In more realistic studies, where molecular dynamics simulations were used to model different DNA coordinates, with water molecules and ions included, base distinction appeared to be more difficult<sup>87,88</sup>. Also, the nanoribbon and nanopore edges were considered to be of either armchair or zigzag type, whereas in practice they may consist of a mixture of armchair and zigzag edges.

Experimentally, monolayer graphene nanoribbons can be produced in various ways. The most common techniques include electron beam lithography, (scanning) transmission electron microscopy ((S)TEM), and scanning tunnelling microscopy (STM) lithography. Alternatively, chemical techniques that involve unzipping of of molecular precursors have

2 | been used<sup>89</sup>. Freestanding graphene nanoribbons (of sub-10 nm widths) were made using STEM<sup>82–85</sup>. It was shown that when the graphene is heated to >600 °C, it can be sculpted with near atomic precision, while maintaining pristine defect-free graphene<sup>84</sup>. At such elevated temperatures, self-repair is mediated by mobile carbon adatoms that constantly repair the defects caused by the electron beam. One can control the shape of the edges by cutting along specific crystallographic directions (Fig. 2.4b)<sup>85</sup>. Crystalline ribbons were also obtained using Joule heating, where a large voltage (~3 V) is applied across the ribbon, leading to local heating (>2,000 K) due to the high current densities. This heating recrystallizes the edges of the nanoribbon that rearrange along either a zigzag or armchair profile<sup>90</sup>. With that approach, armchair ribbons down to 0.7 nm in width were made, which were highly conducting and could sustain microampere currents at low voltages<sup>82,83</sup>.

First experimental results on DNA translocation through graphene nanoribbons with nanopores were reported in 2013 (Fig. 2.4c)<sup>80</sup>. For an electron-beam-patterned ~100-nm-wide ribbon with a pore size of ~10 nm, simultaneous current drops in the ionic current and signals in the graphene ribbon during DNA translocation events were presented. These graphene current modulations were however caused by a nonlocal capacitive coupling of the DNA molecules to the ribbon, similar to the field effect described in ref. 91, whereas the effect evaluated in the theoretical proposals is induced by a change in local density of states at the pore. It is to be expected that smaller ribbons will exhibit much higher sensitivity. The currents through graphene nanoribbons are relatively large (much larger than the ionic currents in nanopore measurements and the predicted tunnelling currents across graphene nanogaps), and the resistance will only be on the order of the quantum resistance (that is, much smaller than that of nanopores and nanogaps). Accordingly, it can be expected that it is possible to carry out measurements at much higher bandwidths. This implies that one can potentially measure DNA-sequence information much faster, possibly even at the normal translocation speed of the DNA molecule, which would present a major advantage over conventional nanopore measurements. Given the sizeable efforts to fabricate well-defined small graphene nanostructures, it can be expected that DNA translocation experiments with nanoribbon–nanopore devices will be performed in the coming years, resolving whether one can indeed sequence DNA with this approach.

## 2.5 DETECTION METHODS BASED ON DNA ADSORPTION

The strong binding interactions between the aromatic groups of DNA bases and graphene have prompted researchers to find ways to exploit these interactions for a range of DNA sequencing applications based on current modulations in graphene due to DNA physisorption, or on measurements that rely on differences in electrochemical activity, graphene field-effect transistors (FETs), and optical detection on adsorption and desorption of DNA molecules.

The nature of the binding of DNA bases to graphene is complex. Several mechanisms have been discussed, including  $\pi$ - $\pi$  stacking, electrostatic, van der Waals, and hydrophobic interactions<sup>92</sup>. The main contribution is attributed to  $\pi$ - $\pi$  bonding, which explains why single-stranded DNA binds more strongly to graphene than double-stranded DNA where the bases are hydrogen bonded and stacked within the helical structure<sup>93,94</sup>. The interaction strengths of the different bases with graphene vary as they depend on the polarizability of the DNA bases<sup>93,95</sup>. Both theoretical and experimental studies report that G binds most strongly to graphene while A, T, and C have lower and similar interaction strengths<sup>93,96-100</sup>.

The non-covalent adsorption of DNA bases to graphene was suggested to induce modulations in the current through graphene nanostructures (Fig. 2.5a)<sup>101-104</sup>. To explore its use for DNA sequencing, the effects of DNA base adsorption on a graphene nanoribbon were calculated with DFT and NEGF<sup>101</sup>. The stacking interactions were found to be sufficiently strong to modulate the current and simultaneously sufficiently weak to allow detachment and subsequent attachment of the next base of a DNA molecule that was passing through the armchair nanoribbon (Fig. 2.5a). The interactions were shown to result in base-dependent conductance drops, due to Fano resonances (Fig. 2.5b)<sup>102</sup>. A second report demonstrated that T, G, and C bases that were adsorbed on a graphene ribbon altered the electric current through the ribbon, while a clear signature was lacking for A (ref. 103). It has to be noted that it will be extremely challenging to make ribbons that are narrow enough, such that only a single nucleotide can adsorb at the same time. It is likely that this will only be feasible with ribbons that are fabricated bottom up through chemical synthesis<sup>105</sup>. Base-dependent changes in the local density of states in graphene were confirmed in STM spectroscopy experiments. Calculations of the local tunnelling conductance through DNA bases that were physisorbed on graphene showed distinct peaks (Fig. 2.5c)<sup>106</sup>, and STM spectroscopy on a Cu(111) surface was shown to be able to distinguish G bases within a single-stranded DNA molecule (Fig. 2.5d)<sup>107</sup>.

A wide variety of experimental studies have been reported that exploit graphene-DNA interactions to determine sequence variations, using electrochemical, FET, and fluorescent detection schemes. Although most of these approaches are not suitable for actual de novo sequencing, they have succeeded in measuring DNA mismatches (for example, single or double DNA base mismatches). Graphene is well suited for electrochemical detection methods due to its high electrical conductivity, large surface area, and very fast heterogeneous electron transfer<sup>108</sup>. Single-nucleotide polymorphisms (SNP) were detected<sup>109,110</sup> with electrochemical impedance spectroscopy, where the charge transfer between the solution and the graphene is modified by adsorption or desorption of molecules on the surface. SNPs are sequence variations where a single nucleotide in the genome differs from the wild-type genome. They are widely studied as they relate to many diseases, such as can-

cer and Alzheimer's disease<sup>4</sup>. Electronic measurements on single-stranded DNA adsorption on graphene were also performed in a biochemical FET set-up, where the effect of DNA adsorption and hybridization on the source–drain current in graphene sheets was measured on variation of a gate potential<sup>111,112</sup>. Not surprisingly, single-stranded DNA was found to act as a negative gating agent that increased the hole density in graphene<sup>113,114</sup>. DNA hybridization to immobilized single-stranded DNA probes on chemical vapour deposition graphene could be used to detect single base mismatches<sup>114</sup>. Multiple DNA targets and various mismatched DNA strands were also selectively detected with fluorescence microscopy<sup>115–118</sup>. Fluorescent dyes attached to single-stranded DNA probes adsorbed to a graphene surface were efficiently quenched by graphene oxide, while after hybridization to complementary or mismatched strands, the fluorescent signals reappeared in the double-stranded DNA. A large number of studies have been reported on biosensing with graphene and graphene oxide (sensing amino acids, peptides, glucose, and more), and the interested reader is referred to ref. 119 for an extensive overview.

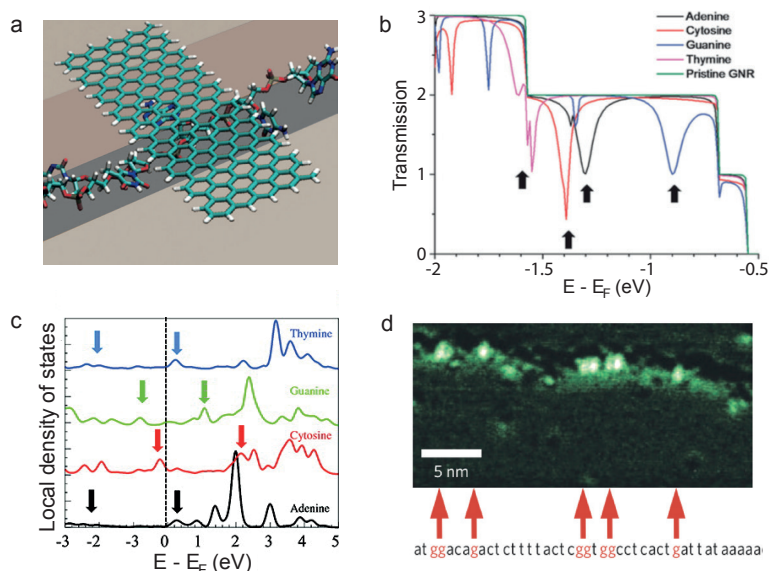


**Figure 2.5: DNA detection methods based on DNA physisorption.** (a) Schematic of a nanochannel device with an armchair graphene nanoribbon (GNR) along which a single-stranded DNA passes. DNA bases temporarily adsorb on the graphene while moving through the channel. (b) DFT results for the structure in a show that base-varying conductance dips appear due to Fano resonance (black arrows) as a result of such DNA adsorption. (c) DFT calculations for single DNA bases adsorbed on to graphene show different tunnelling conductances due to their differences in local density of states. (d) STM image of single-stranded DNA molecules on a Cu(111) surface. The guanine sites are indicated by red characters in the bottom sequence, and by the red arrows. Scale bar, 5 nm. Figures adapted with permission from: a, ref. 101, Nature Publishing Group; b, ref. 102, RSC; c, ref. 106, American Chemical Society; d, ref. 107, Nature Publishing Group.

Adsorption of DNA onto sensitive nanographene structures, such as nanoribbons, can potentially lead to base-specific information. One major advantage in these adsorption studies is that base fluctuations in position and angle are minimized, which could lead to lower noise in the measurements. Further exploration of the approaches described above will reveal whether these techniques may indeed lead to actual DNA sequencing.

## 2.6 OUTLOOK

Many efforts have been directed at developing new DNA sequencing techniques that benefit from graphene's special properties. In this Review, we highlighted the most prominent approaches involving graphene nanopores, nanogaps, nanoribbons, and physisorption on graphene nanostructures.

Despite the clear progress in the nanopore-sensing field, we believe that ionic current detection will not be the ultimate approach that will lead to DNA sequencing using graphene nanodevices. Major challenges remain in slowing down the DNA during translocation, reducing the stochasticity in the translocation velocity, reducing conformational fluctuations of the bases residing within the pore, and lowering noise levels. More promising, in our view, is to employ the conductive properties of graphene, that is, monitoring modulations in the currents running through a graphene nanostructure on interaction with DNA bases. We have discussed a number of theoretical studies that calculated the variations of tunnelling currents across a gap between two graphene electrodes due to the presence of DNA bases residing within that gap. While these theoretical results on simple model systems were promising, no experimental studies on graphene nanogaps for DNA sequencing have been reported so far, probably because of the significant experimental challenges involved (creating and maintaining a few-nanometres gap between graphene electrodes, slowly traversing DNA through it in a controlled way, and performing tunnelling current measurements while base, water, and ion fluctuations yield significant tunnelling current noise). Results on metallic tunnelling electrodes embedded in silicon nitride nanopores<sup>56,57</sup> are encouraging, however, and similar experiments using graphene electrodes are to be expected.

Many theoretical studies on graphene nanoribbons that contained a small nanopore showed that such ribbon devices can electronically discriminate different bases that occupy the pore, thus providing sequencing information if a DNA strand is led through the nanopore. An advantage over tunnelling current detection is that the currents in the nanoribbons are much larger, likely to yield higher signal-to-noise ratios, and that a lower resistance results in faster relaxation times in the electronic circuit, such that one can potentially carry out measurements at much higher bandwidths. It is to be expected that experiments on narrow graphene nanoribbons will resolve the abilities for base discrimination in the near future.

2 | Electrochemical and fluorescent monitoring of adsorption and desorption of DNA on graphene surfaces has already demonstrated discrimination of local DNA sequence variations, such as SNPs. According to several theoretical studies, DNA base adsorption onto the surface of a graphene nanoribbon may even lead to base-distinct current modulations. Fabrication of very narrow crystalline graphene nanostructures is, however, extremely challenging.

This emphasizes the more general point that atomic engineering of graphene will be key to success in realizing graphene-based DNA sequencing devices. The nanodevices that are most promising for DNA sequencing feature narrow graphene nanostructures with crystalline edges that probe the presence of DNA through detection of a tunnelling current or an inplane nanoribbon current. Fabrication of such nanostructures with atomic-scale control is crucial, but poses quite a challenge. Patterning graphene at elevated temperatures (>600 °C) provides a way to minimize defects to preserve graphene's crystallinity<sup>84</sup>. Narrow ribbons with crystalline edges were also produced through Joule heating<sup>83,90</sup> where a voltage of ~2–3 V applied across a ribbon resulted in a local heating of 2,000 K, leading to recrystallization of the edges<sup>90</sup>. Alternatively, narrow bottom-up graphene nanoribbons that are chemically synthesized with perfect zigzag or armchair edges may represent the ultimate approach for ultrasensitive graphene devices<sup>105</sup>. For a more detailed perspective on the importance of defects in graphene nanostructures, the reader is referred to ref. 120.

Another challenge in many DNA sequencing approaches is to control the motion of the DNA molecule while it translocates through or along the graphene nanostructure. Many different solutions are being explored. Lower temperatures and higher buffer viscosities help a bit. Recently, a viscosity gradient, involving an ionic liquid BmimPF<sub>6</sub> on the cis side and a 2 M KCl solution on the trans side, was used to lower the DNA translocation speed by two orders of magnitude<sup>121</sup>. A very different approach is to employ a polymerase or helicase enzyme to open the double-stranded DNA helix and slowly ratchet one of its strands through the pore channel<sup>27,28</sup>. Such protein–graphene hybrids or DNA origami–graphene structures<sup>122–124</sup> could provide means to control the motion of DNA molecules. Yet another alternative is to use plasmonics to control a DNA molecule in a nanopore<sup>125,126</sup>. In this approach, gold nanoantennas around a graphene nanopore are used to trap the DNA in a plasmonic hot spot right at the pore, introducing a 'physical knob' to switch the motion of the DNA through the pore on or off. Moreover, Raman spectroscopy on the DNA bases in the plasmonic hot spot at the pore can provide sequence information while the DNA molecule is stepped through the pore<sup>125,127</sup>.

Graphene is a special material that offers unexpected opportunities. While this Review described a number of promising concrete proposals to sequence DNA with graphene

nanodevices, the coming years may witness even more different approaches, for example, involving DNA in graphene liquid cells<sup>128</sup> or DNA translocation through carbon nanotubes<sup>129,130</sup>. Given the significant efforts on single-molecule sequencing and the fabrication of graphene nanostructures, we are hopeful that DNA sequencing with graphene will indeed materialize.



## REFERENCES

1. Lander, E. S. et al. Initial sequencing and analysis of the human genome. *Nature* 409, 860–921 (2001).
2. Sanger, F., Nicklen, S. & Coulson, A. R. DNA sequencing with chain-terminating inhibitors. *Proc. Natl Acad. Sci. USA* 74, 5463–5467 (1977).
3. Shendure, J. & Ji, H. Next-generation DNA sequencing. *Nature Biotechnol.* 26, 1135–1145 (2008).
4. Metzker, M. L. Sequencing technologies — the next generation. *Nature Rev. Genet.* 11, 31–46 (2010).
5. Ansorge, W. J. Next-generation DNA sequencing techniques. *New Biotechnol.* 25, 195–203 (2009).
6. Steinbock, L. J. & Radenovic, A. The emergence of nanopores in next-generation sequencing. *Nanotechnology* 26, 074003 (2015).
7. Levene, M. J. et al. Zero-mode waveguides for single-molecule analysis at high concentrations. *Science* 299, 682–686 (2003).
8. Quail, M. A. et al. A tale of three next generation sequencing platforms: comparison of Ion Torrent, Pacific Biosciences and Illumina MiSeq sequencers. *BMC Genomics* 13, 341 (2012).
9. Ferrarini, M. et al. An evaluation of the PacBio RS platform for sequencing and de novo assembly of a chloroplast genome. *BMC Genomics* 14, 670 (2013).
10. Sharon, D., Tilgner, H., Grubert, F. & Snyder, M. A single-molecule long-read survey of the human transcriptome. *Nature Biotechnol.* 31, 1009–1014 (2013).
11. Mikheyev, A. S. & Tin, M. M. A first look at the Oxford Nanopore MinION sequencer. *Mol. Ecol. Resour.* 14, 1097–1102 (2014).
12. Jain, M. et al. Improved data analysis for the MinION nanopore sequencer. *Nature Methods* 12, 351–356 (2015).
13. Novoselov, K. S. et al. Electric field effect in atomically thin carbon films. *Science* 306, 666–669 (2004).
14. Novoselov, K. S. et al. Two-dimensional atomic crystals. *Proc. Natl Acad. Sci. USA* 102, 10451–10453 (2005).
15. Geim, A. K. & Novoselov, K. S. The rise of graphene. *Nature Mater.* 6, 183–191 (2007).
16. Lee, C., Wei, X., Kysar, J. W. & Hone, J. Measurement of the elastic properties and intrinsic strength of monolayer graphene. *Science* 321, 385–388 (2008).
17. Schedin, F. et al. Detection of individual gas molecules adsorbed on graphene. *Nature Mater.* 6, 652–655 (2007).
18. Nair, R. R. et al. Fine structure constant defines visual transparency of graphene. *Science* 320, 1308 (2008).
19. Pereira, V., Castro Neto, A. & Peres, N. Tight-binding approach to uniaxial strain in graphene. *Phys. Rev. B* 80, 045401 (2009).
20. Balandin, A. A. et al. Superior thermal conductivity of single-layer graphene. *Nano Lett.* 8, 902–907 (2008).
21. Morozov, S. et al. Giant intrinsic carrier mobilities in graphene and its bilayer. *Phys. Rev. Lett.* 100, 016602 (2008).
22. Ferrari, A. C. et al. Science and technology roadmap for graphene, related two-dimensional crystals, and hybrid systems. *Nanoscale* 7, 4598–4810 (2015).

23. Neher, E. & Sakmann, B. Single-channel currents recorded from membrane of denervated frog muscle fibres. *Nature* 260, 799–802 (1976).
24. Colombini, M. Pore size and properties of channels from mitochondria isolated from *Neurospora crassa*. *J. Membrane Biol.* 53, 79–84 (1980).
25. Krasilnikov, O., Sabirov, R., Ternovsky, V., Merzliak, P. & Muratkhodjaev, J. A simple method for the determination of the pore radius of ion channels in planar lipid bilayer membranes. *FEMS Microbiol. Lett.* 105, 93–100 (1992).
26. Kasianowicz, J. J., Brandin, E., Branton, D. & Deamer, D. W. Characterization of individual polynucleotide molecules using a membrane channel. *Proc. Natl Acad. Sci. USA* 93, 13770–13773 (1996).
27. Cherf, G. M. et al. Automated forward and reverse ratcheting of DNA in a nanopore at 5-Å precision. *Nature Biotechnol.* 30, 344–348 (2012).
28. Manrao, E. A. et al. Reading DNA at single-nucleotide resolution with a mutant MspA nanopore and phi29 DNA polymerase. *Nature Biotechnol.* 30, 349–53 (2012).
29. Dekker, C. Solid-state nanopores. *Nature Nanotech.* 2, 209–215 (2007).
30. Garaj, S. et al. Graphene as a subnanometre trans-electrode membrane. *Nature* 467, 190–193 (2010).
31. Garaj, S., Liu, S., Golovchenko, J. A. & Branton, D. Molecule-hugging graphene nanopores. *Proc. Natl Acad. Sci. USA* 110, 12192–12196 (2013).
32. Sathe, C., Zou, X., Leburton, J.-P. & Schulten, K. Computational investigation of DNA detection using graphene nanopores. *ACS Nano* 5, 8842–8851 (2011).
33. Wells, D. B., Belkin, M., Comer, J. & Aksimentiev, A. Assessing graphene nanopores for sequencing DNA. *Nano Lett.* 12, 4117–4123 (2012).
34. Liang, L. et al. Theoretical study on key factors in DNA sequencing with graphene nanopores. *RSC Adv.* 3, 2445–2453 (2013).
35. Schneider, G. F. et al. DNA translocation through graphene nanopores. *Nano Lett.* 10, 3163–3167 (2010).
36. Merchant, C. A. et al. DNA translocation through graphene nanopores. *Nano Lett.* 10, 2915–2921 (2010).
37. Schneider, G. F. et al. Tailoring the hydrophobicity of graphene for its use as nanopores for DNA translocation. *Nature Commun.* 4, 2619 (2013).
38. Banerjee, S. et al. Slowing DNA transport using graphene–DNA interactions. *Adv. Funct. Mater.* 25, 936–946 (2014).
39. Rosenstein, J. K., Wanunu, M., Merchant, C. A., Drndic, M. & Shepard, K. L. Integrated nanopore sensing platform with sub-microsecond temporal resolution. *Nature Methods* 9, 487–492 (2012).
40. Plesa, C., van Loo, N., Ketterer, P., Dietz, H. & Dekker, C. Velocity of DNA during translocation through a solid-state nanopore. *Nano Lett.* 15, 732–737 (2015).

41. Heerema, S. J. et al. 1/f noise in graphene nanopores. *Nanotechnology* 26, 074001 (2015).
42. Venkatesan, B. M. et al. Stacked graphene-Al<sub>2</sub>O<sub>3</sub> nanopore sensors for sensitive detection of DNA and DNA–protein complexes. *ACS Nano* 6, 441–450 (2012).
43. Banerjee, S. et al. Electrochemistry at the edge of a single graphene layer in a nanopore. *ACS Nano* 7, 834–843 (2013).
44. Lee, M.-H. et al. A low-noise solid-state nanopore platform based on a highly insulating substrate. *Sci. Rep.* 4, 7448 (2014).
45. Postma, H. W. C. Rapid sequencing of individual DNA molecules in graphene nanogaps. *Nano Lett.* 10, 420–425 (2010).
46. Zhao, Q. et al. Nanopore-based DNA analysis via graphene electrodes. *Nanomater.* 2012, 1–5 (2012).
47. Zhang, H. et al. Detection of nucleic acids by graphene-based devices: a first-principles study. *J. Appl. Phys.* 115, 133701 (2014).
48. Jeong, H. et al. Quantum interference in DNA bases probed by graphene nanoribbons. *Appl. Phys. Lett.* 103, 023701 (2013).
49. Prasongkit, J., Grigoriev, A., Pathak, B., Ahuja, R. & Scheicher, R. H. Transverse conductance of DNA nucleotides in a graphene nanogap from first principles. *Nano Lett.* 11, 1941–1945 (2011).
50. Prasongkit, J., Grigoriev, A., Pathak, B., Ahuja, R. & Scheicher, R. H. Theoretical study of electronic transport through DNA nucleotides in a double-functionalized graphene nanogap. *J. Phys. Chem. C* 117, 15421–15428 (2013).
51. He, Y. et al. Enhanced DNA sequencing performance through edge-hydrogenation of graphene electrodes. *Adv. Funct. Mater.* 21, 2674–2679 (2011).
52. Huang, S. et al. Identifying single bases in a DNA oligomer with electron tunnelling. *Nature Nanotech.* 5, 868–873 (2010).
53. Lindsay, S. et al. Recognition tunneling. *Nanotechnology* 21, 262001 (2010).
54. Krishnakumar, P. et al. Slowing DNA translocation through a nanopore using a functionalized electrode. *ACS Nano* 7, 10319–10326 (2013).
55. Ivanov, A. P. et al. DNA tunneling detector embedded in a nanopore. *Nano Lett.* 11, 279–285 (2011).
56. Tsutsui, M., Taniguchi, M., Yokota, K. & Kawai, T. Identifying single nucleotides by tunnelling current. *Nature Nanotech.* 5, 286–290 (2010).
57. Tsutsui, M. et al. Single-molecule sensing electrode embedded in-plane nanopore. *Sci. Rep.* 1, 46 (2011).
58. Bagci, V. M. K. & Kaun, C.-C. Recognizing nucleotides by cross-tunneling currents for DNA sequencing. *Phys. Rev. E* 84, 011917 (2011).
59. Chen, X., Rungger, I., Pemmaraju, C. D., Schwingenschlögl, U. & Sanvito, S. First principles study of high-conductance DNA sequencing with carbon nanotube

- electrodes. *Phys. Rev. B* 85, 115436 (2012).
60. Prins, F. et al. Room-temperature gating of molecular junctions using few-layer graphene nanogap electrodes. *Nano Lett.* 11, 4607–4611 (2011).
  61. Nef, C. et al. High-yield fabrication of nm-size gaps in monolayer CVD graphene. *Nanoscale* 6, 7249–7254 (2014).
  62. Sadeghi, H. et al. Conductance enlargement in picoscale electroburnt graphene nanojunctions. *Proc. Natl Acad. Sci. USA* 112, 2658–2663 (2015).
  63. Island, J. O. et al. Fabrication of hybrid molecular devices using multi-layer graphene break junctions. *J. Phys. Condens. Matter* 26, 474205 (2014).
  64. Cao, Y. et al. Building high-throughput molecular junctions using indented graphene point contacts. *Angew. Chem.* 124, 12394–12398 (2012).
  65. Wallace, P. The band theory of graphite. *Phys. Rev.* 71, 622–634 (1947).
  66. Fujita, M., Wakabayashi, K., Nakada, K. & Kusakabe, K. Peculiar localized state at zigzag graphite edge. *J. Phys. Soc. Jpn* 65, 1920–1923 (1996).
  67. Wakabayashi, K., Fujita, M., Ajiki, H. & Sigrist, M. Electronic and magnetic properties of nanographite ribbons. *Phys. Rev. B* 59, 8271–8282 (1999).
  68. Ezawa, M. Peculiar width dependence of the electronic properties of carbon nanoribbons. *Phys. Rev. B* 73, 045432 (2006).
  69. Brey, L. & Fertig, H. Electronic states of graphene nanoribbons studied with the Dirac equation. *Phys. Rev. B* 73, 235411 (2006).
  70. Nakada, K., Fujita, M., Dresselhaus, G. & Dresselhaus, M. Edge state in graphene ribbons: nanometer size effect and edge shape dependence. *Phys. Rev. B* 54, 17954–17961 (1996).
  71. Sasaki, K.-i., Murakami, S. & Saito, R. Gauge field for edge state in graphene. *Phys. Soc. Jpn* 75, 074713 (2006).
  72. Nelson, T., Zhang, B. & Prezhd, O. V. Detection of nucleic acids with graphene nanopores: ab initio characterization of a novel sequencing device. *Nano Lett.* 10, 3237–3242 (2010).
  73. Ouyang, F.-P., Peng, S.-L., Zhang, H., Weng, L.-B. & Xu, H. A biosensor based on graphene nanoribbon with nanopores: a first-principles devices-design. *Chinese Phys. B* 20, 058504 (2011).
  74. Saha, K. K., Drndić, M. & Nikolić, B. K. DNA base-specific modulation of microampere transverse edge currents through a metallic graphene nanoribbon with a nanopore. *Nano Lett.* 12, 50–55 (2012).
  75. Avdoshenko, S. M. et al. Dynamic and electronic transport properties of DNA translocation through graphene nanopores. *Nano Lett.* 13, 1969–1976 (2013).
  76. Girdhar, A., Sathe, C., Schulten, K. & Leburton, J.-P. Graphene quantum point contact transistor for DNA sensing. *Proc. Natl Acad. Sci. USA* 110, 16748–16753 (2013).

- 2 |
77. Ahmed, T., Haraldsen, J. T., Zhu, J.-X. & Balatsky, A. V. Next-generation epigenetic detection technique: identifying methylated cytosine using graphene nanopore. *J. Phys. Chem. Lett.* 5, 2601–2607 (2014).
  78. Sadeghi, H. et al. Graphene sculpturene nanopores for DNA nucleobase sensing. *J. Phys. Chem. B* 118, 6908–6914 (2014).
  79. Ahmed, T. et al. Correlation dynamics and enhanced signals for the identification of serial biomolecules and DNA bases. *Nanotechnology* 25, 125705 (2014).
  80. Traversi, F. et al. Detecting the translocation of DNA through a nanopore using graphene nanoribbons. *Nature Nanotech.* 8, 939–945 (2013).
  81. Lu, Y., Merchant, C. A., Drndić, M. & Johnson, A. T. C. In situ electronic characterization of graphene nanoconstrictions fabricated in a transmission electron microscope. *Nano Lett.* 11, 5184–5188 (2011).
  82. Puster, M., Rodríguez-Manzo, J. A., Balan, A. & Drndić, M. Toward sensitive graphene nanoribbon-nanopore devices by preventing electron beam-induced damage. *ACS Nano* 7, 11283–11289 (2013).
  83. Qi, Z. J. et al. Correlating atomic structure and transport in suspended graphene nanoribbons. *Nano Lett.* 14, 4238–4244 (2014).
  84. Song, B. et al. Atomic-scale electron-beam sculpting of near-defect-free graphene nanostructures. *Nano Lett.* 11, 2247–2250 (2011).
  85. Xu, Q. et al. Controllable atomic scale patterning of freestanding monolayer graphene at elevated temperature. *ACS Nano* 7, 1566–1572 (2013).
  86. Chang, P.-H., Liu, H. & Nikolić, B. K. First-principles versus semi-empirical modeling of global and local electronic transport properties of graphene nanopore-based sensors for DNA sequencing. *J. Comput. Electron.* 13, 847–856 (2014).
  87. Lagerqvist, J., Zwolak, M. & Di Ventra, M. Influence of the environment and probes on rapid DNA sequencing via transverse electronic transport. *Biophys. J.* 93, 2384–2390 (2007).
  88. Feliciano, G. T. et al. Capacitive DNA detection driven by electronic charge fluctuations in a graphene nanopore. *Phys. Rev. Appl.* 3, 034003 (2015).
  89. Jia, X., Campos-Delgado, J., Terrones, M., Meunier, V. & Dresselhaus, M. S. Graphene edges: a review of their fabrication and characterization. *Nanoscale* 3, 86–95 (2011).
  90. Qi, Z. J. et al. Electronic transport of recrystallized freestanding graphene nanoribbons. *ACS Nano* 9, 3510–3520 (2015).
  91. Xie, P., Xiong, Q., Fang, Y., Qing, Q. & Lieber, C. M. Local electrical potential detection of DNA by nanowire-nanopore sensors. *Nature Nanotech.* 7, 119–125 (2012).
  92. Oliveira Brett, A. M. & Chiorcea, A.-M. Atomic force microscopy of DNA immobilized onto a highly oriented pyrolytic graphite electrode surface. *Langmuir*

- 19, 3830–3839 (2003).
93. Gowtham, S., Scheicher, R., Ahuja, R., Pandey, R. & Karna, S. Physisorption of nucleobases on graphene: density-functional calculations. *Phys. Rev. B* 76, 033401 (2007).
  94. Akca, S., Foroughi, A., Frochtzwajg, D. & Postma, H. W. C. Competing interactions in DNA assembly on graphene. *PLoS ONE* 6, e18442 (2011).
  95. Lee, J.-H., Choi, Y.-K., Kim, H.-J., Scheicher, R. H. & Cho, J.-H. Physisorption of DNA nucleobases on h-BN and graphene: vdW-corrected DFT calculations. *J. Phys. Chem. C* 117, 13435–13441 (2013).
  96. Antony, J. & Grimme, S. Structures and interaction energies of stacked graphene–nucleobase complexes. *Phys. Chem. Chem. Phys.* 10, 2722–2729 (2008).
  97. Varghese, N. et al. Binding of DNA nucleobases and nucleosides with graphene. *ChemPhysChem* 10, 206–210 (2009).
  98. Das, A. et al. Binding of nucleobases with single-walled carbon nanotubes: theory and experiment. *Chem. Phys. Lett.* 453, 266–273 (2008).
  99. Umadevi, D. & Sastry, G. N. Quantum mechanical study of physisorption of nucleobases on carbon materials: graphene versus carbon nanotubes. *J. Phys. Chem. Lett.* 2, 1572–1576 (2011).
  100. Le, D., Kara, A., Schröder, E., Hyldgaard, P. & Rahman, T. S. Physisorption of nucleobases on graphene: a comparative van der Waals study. *J. Phys. Condens. Matter* 24, 424210 (2012).
  101. Min, S. K., Kim, W. Y., Cho, Y. & Kim, K. S. Fast DNA sequencing with a graphene-based nanochannel device. *Nature Nanotech.* 6, 162–165 (2011).
  102. Cho, Y., Min, S. K., Kim, W. Y. & Kim, K. S. The origin of dips for the graphene-based DNA sequencing device. *Phys. Chem. Chem. Phys.* 13, 14293–14296 (2011).
  103. Song, B., Cuniberti, G., Sanvito, S. & Fang, H. Nucleobase adsorbed at graphene devices: enhance bio-sensorics. *Appl. Phys. Lett.* 100, 063101 (2012).
  104. Bobadilla, A. D. & Seminario, J. M. Assembly of a noncovalent DNA junction on graphene sheets and electron transport characteristics. *J. Phys. Chem. C* 117, 26441–26453 (2013).
  105. Cai, J. et al. Atomically precise bottom-up fabrication of graphene nanoribbons. *Nature* 466, 470–473 (2010).
  106. Ahmed, T. et al. Electronic fingerprints of DNA bases on graphene. *Nano Lett.* 12, 927–931 (2012).
  107. Tanaka, H. & Kawai, T. Partial sequencing of a single DNA molecule with a scanning tunnelling microscope. *Nature Nanotech.* 4, 518–522 (2009).
  108. Davies, T. J., Hyde, M. E. & Compton, R. G. Nanotrench arrays reveal insight into graphite electrochemistry. *Angew. Chem. Int. Ed.* 44, 5121–5126 (2005).
  109. Bonanni, A. & Pumera, M. Graphene platform for hairpin-DNA-based impedimetric

- genosensing. *ACS Nano* 5, 2356–2361 (2011).
110. Zainudin, N., Mohd Hairul, A. R., Yusoff, M. M., Tan, L. L. & Chong, K. F. Impedimetric graphene-based biosensor for the detection of *Escherichia coli* DNA. *Anal. Methods* 6, 7935–7941 (2014).
111. Heller, I. et al. Identifying the mechanism of biosensing with carbon nanotube transistors. *Nano Lett.* 8, 591–595 (2008).
112. Heller, I. et al. Influence of electrolyte composition on liquid-gated carbon nanotube and graphene transistors. *J. Am. Chem. Soc.* 132, 17149–17156 (2010).
113. Lin, J. et al. Gating of single-layer graphene with single-stranded deoxyribonucleic acids. *Small* 6, 1150–1155 (2010).
114. Dong, X., Shi, Y., Huang, W., Chen, P. & Li, L.-J. Electrical detection of DNA hybridization with single-base specificity using transistors based on CVD-grown graphene sheets. *Adv. Mater.* 22, 1649–1653 (2010).
115. Lu, C., Yang, H., Zhu, C., Chen, X. & Chen, G. A graphene platform for sensing biomolecules. *Angew. Chem.* 121, 4879–4881 (2009).
116. He, S. et al. A graphene nanoprobe for rapid, sensitive, and multicolor fluorescent DNA analysis. *Adv. Funct. Mater.* 20, 453–459 (2010).
117. Balapanuru, J. et al. A graphene oxide-organic dye ionic complex with DNA-sensing and optical-limiting properties. *Angew. Chem.* 122, 6699–6703 (2010).
118. Tao, Y., Lin, Y., Huang, Z., Ren, J. & Qu, X. DNA-templated silver nanoclusters-graphene oxide nanohybrid materials: a platform for label-free and sensitive fluorescence turn-on detection of multiple nucleic acid targets. *Analyst* 137, 2588–2592 (2012).
119. Hu, Y., Li, F., Han, D. & Niu, L. *Biocompatible Graphene for Bioanalytical Applications* (Springer, 2014).
120. Vicarelli, L., Heerema, S. J., Dekker, C. & Zandbergen, H. W. Controlling defects in graphene for optimizing the electrical properties of graphene nanodevices. *ACS Nano* 9, 3428–3435 (2015).
121. Feng, J. et al. Identification of single nucleotides in MoS<sub>2</sub> nanopores. *Nature Nanotech.* 10, 1070–1076 (2015).
122. Wei, R., Martin, T. G., Rant, U. & Dietz, H. DNA origami gatekeepers for solid-state nanopores. *Angew. Chem.* 124, 4948–4951 (2012).
123. Bell, N. A. W. et al. DNA origami nanopores. *Nano Lett.* 12, 512–517 (2012).
124. Plesa, C. et al. Ionic permeability and mechanical properties of DNA origami nanoplates on solid-state nanopores. *ACS Nano* 8, 35–43 (2014).
125. Jonsson, M. P. & Dekker, C. Plasmonic nanopore for electrical profiling of optical intensity landscapes. *Nano Lett.* 13, 1029–1033 (2013).
126. Nam, S. et al. Graphene nanopore with a self-integrated optical antenna. *Nano Lett.* 14, 5584–5589 (2014).

127. Belkin, M., Chao, S.-H., Jonsson, M. P., Dekker, C. & Aksimentiev, A. Plasmonic nanopores for trapping, controlling displacement, and sequencing of DNA. *ACS Nano* 9, 10598–10611 (2015).
128. Chen, Q. et al. 3D motion of DNA–Au nanoconjugates in graphene liquid cell electron microscopy. *Nano Lett.* 13, 4556–4561 (2013).
129. Liu, H. et al. Translocation of single-stranded DNA through single-walled carbon nanotubes. *Science* 327, 64–67 (2010).
130. Siwy, Z. S. & Davenport, M. Making nanopores from nanotubes. *Nature Nanotech.* 5, 174–175 (2010).





# 3

## CONTROLLING DEFECTS IN GRAPHENE FOR OPTIMIZING THE ELECTRICAL PROPERTIES OF GRAPHENE NANODEVICES

**S**tructural defects strongly impact the electrical transport properties of graphene nanostructures. Here, we give a brief overview of different types of defects in graphene and their effect on transport properties. We discuss recent experimental progress on graphene self-repair of defects, with a focus on in-situ transmission electron microscopy studies. Finally, a future outlook for graphene self-repair and in-situ experiments is presented.

---

This chapter was published as: Leonardo Vicarelli, Stephanie J. Heerema, Cees Dekker and Henny W. Zandbergen, ACS Nano 9, 3428–3435 (2015)

### 3.1 DEFECTS AND ELECTRICAL TRANSPORT IN GRAPHENE

3 | Ideal graphene is a one-atom-thick layer of carbon atoms that are perfectly arranged in a two-dimensional honeycomb lattice. Each carbon atom is coordinated with other three carbon atoms, with identical  $120^\circ$  in-plane bonding angles. The presence of structural defects breaks this perfect symmetry, and opens a whole research area for studying their effect on mechanical, electrical, chemical and optical properties of graphene. Sometimes their effect is beneficial. For example, defects are essential in chemical and electro-chemical studies, where they create preferential bonding sites for adsorption of atoms and molecules, which can be used for gas and liquid sensing. On the other hand, defects pose a problem for electronics applications such as Field-Effect Transistors and electrical interconnects, because they can significantly lower the charge carrier mobility and thus increase the resistivity of graphene<sup>1-4</sup>. While this is the general rule, there are also some exceptions where defects can be engineered in regular arrays to yield metallic or insulating states<sup>5,6</sup>.

Given their crucial impact on graphene properties, it is important to control defect formation and, if possible, find ways to repair existing defects. Important progress in this direction has recently been reported, where several in-situ Transmission Electron Microscopy (TEM) experiments have observed self-repair of graphene heated at high temperatures ( $>500^\circ\text{C}$ )<sup>7-9</sup>. TEM is, in fact, the perfect tool for this kind of studies, as it combines atomic resolution with capabilities such as in-situ heating and in-situ electrical measurements. With this approach, correlating defects and electronic transport becomes a manageable task, as the experimenter can determine defects with atomic resolution and simultaneously measure the conductivity.

In this issue of ACS Nano<sup>9</sup>, Qi and co-workers fully exploit this potential of in-situ TEM and observe, in real-time and with atomic resolution, the effects of edge recrystallization induced by Joule heating on the conductivity of a single graphene nanoribbon. Details on this study are summarized in the second part of this Perspective, where they are accompanied by three other recent experiments on graphene self-repair. But first, we provide an overview of the types of defects that are present in graphene, and we briefly discuss their effect on the electron transport properties with an emphasis on graphene nanoribbons.

#### 3.1.1 DEFECTS IN GRAPHENE

In graphene, we can distinguish vacancy, impurity and topological defects. In a vacancy defect, one or more atoms are removed from the lattice. In an impurity defect, one carbon atom is replaced by another atom of a different element. In a topological defect, no atom is removed from the lattice, but the bonding angles between the carbon atoms are rotated. Vacancy defects in graphene are not easily formed. The energy required to sputter (or “knock on”) a single atom out of the lattice is 18-20 eV<sup>10</sup>. Such energy can be provided by

bombarding ions in a plasma, or by electrons with an energy  $>86$  keV, which is typically achievable in a TEM (high energy electrons are needed because the cross section for Coulomb scattering with a carbon atom is very small). This kind of vacancy defects act as strong scattering centers for the charge carriers in graphene, decreasing the localization length and disrupting the ballistic nature of electronic transport in graphene. For a low and medium vacancy defect density ( $10^{10}$ - $10^{12}$  cm<sup>-2</sup>, or 0.01-0.1% of the total area), mobility reduction is generally observed<sup>11</sup>. For a high defect density ( $>10^{13}$  cm<sup>-2</sup>, 1% of the area), Anderson insulating behavior is predicted to develop<sup>4</sup>.

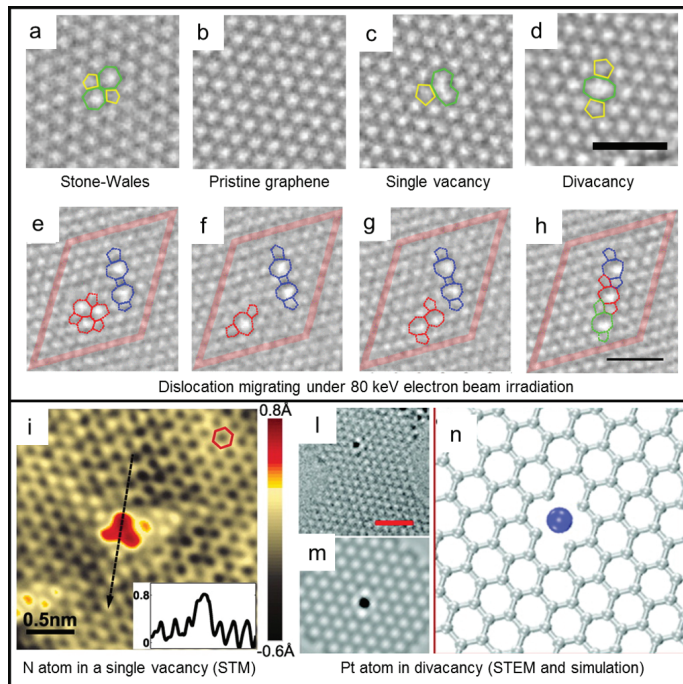


**Figure 3.1. Structural defects in graphene.** (a-d) HRTEM images of (a) Stone-Wales defect, (b) defect-free graphene, (c) single vacancy with 5-9 rings, (d) divacancy with 5-8-5 rings. Scale bar is 1 nm. (e-h) HRTEM image sequence of divacancy migration observed at 80 keV. Scale bar is 1 nm. Reprinted with permission from ref 13. Copyright 2011 American Physical Society. (i) STM image of a single N atom dopant in graphene on a copper foil substrate. (Inset) Line profile across the dopant shows atomic corrugation and apparent height of the dopant. Reprinted with permission from ref 15. Copyright 2011 American Association for the Advancement of Science. (l,m) HRTEM images of a Pt atom trapped in divacancy and (n) simulated HRTEM image for the Pt-vacancy complex. Scale bar is 1 nm. Reprinted from ref 14.

An example of a single-atom vacancy is shown in Figure 3.1c. The missing atom causes the lattice to rearrange in a 5 carbon atom ring (5-ring) plus a 9-ring. The sp<sup>2</sup> hybridization is broken, leaving one dangling bond unsaturated. Single vacancies can migrate and merge in divacancies. Such migration has a low activation energy (1.3 eV) and should already be

3 | observed at 200°C<sup>12</sup> (to our knowledge, single vacancy migration has not been recorded in any experiment yet). Instead, divacancies (shown in Figure 3.1d) need to overcome a larger energy barrier to migrate (5-6 eV), which makes them much more stable than single vacancies<sup>12,13</sup>. Divacancy migration was observed by Kotakoski et al.,<sup>13</sup> under the influence of an 80 keV electron beam in a TEM (see Figures 3.1e-h). The migration involved only carbon bond rotation, no additional vacancies were created.

Whenever a vacancy is formed in graphene, an external element can replace the missing atom and fill the void in the lattice, forming an impurity defect. Single vacancies are ideal trapping sites for the small atoms, such as B and N, while noble and transition metals, with larger atomic radii, prefer to rest on multi-vacancies<sup>14</sup> Zhao et al.<sup>15</sup> obtained chemical-vapor deposition (CVD) graphene with N impurities by adding ammonia (NH<sub>3</sub>) as a precursor during the growth process. A high density of N atoms was obtained (0.34% of C atoms), which resulted in a considerable n-type doping of graphene. As it can be seen from the STM images shown in Figure 3.1i, each N atom replaced a single C atom in the lattice, creating a perturbation in the local density of states which rapidly decayed in space (~7 Å radius around the N atom). Conversely, Wang et al.<sup>14</sup> created vacancies in graphene with pulsed laser deposition and implanted different elements (Pt, Co, and In) afterwards. In this case, the doping has been theoretically predicted to depend on the work function of the guest element (p-type if higher than the graphene work-function, n-type otherwise). Figures 3.1j-n show an example of a Pt atom trapped in a di-vacancy. The binding energy of the platinum atom in this configuration is 6 eV, which also makes it stable for prolonged TEM observation at low voltage (60 keV).

Finally, we consider topological defects in graphene. The simplest one is a single disclination, i.e., the presence of a 5- or 7-ring that alters the regular 6-ring structure (see Figures 3.2a,b). Isolated disclinations are highly unlikely to develop in single layer graphene, because they require an out-of-plane bulging of the graphene sheet, and therefore have a high formation energy<sup>16</sup>. Dislocations are a combination of two or more complementary disclinations. The most basic dislocation is composed by a 5-7 ring pair, as shown in Figure 3.2c. Another interesting and frequently occurring dislocation is the Stone-Wales defect, which is composed of two 5-7 ring pairs (shown in Figure 3.1a).

The most prominent example of extended dislocations are grain boundaries (GB). GBs are formed in graphene whenever two separate domains (grains), with a different crystallographic orientation, are linked together. Figures 3.2d,e show examples of a GB that connects two grains which are rotated by 32.3° and 27°, respectively. Experiments conducted on CVD grown graphene have shown that GBs degrade the electronic transport in graphene. Tsen et al.<sup>2</sup> have measured that a single GB has a resistivity of 0.5 to 4 kΩ.μm, depending on the position of the Fermi level in the graphene grains. GBs are usually intrinsic

sically n-type doped, while the surrounding graphene can be either n- or p- type. In the latter case, a sharp p-n junction is formed, which leads to a yet larger resistance. A special case of GB with zero rotation angle (see Figure 3.2f) was experimentally investigated by Lahiri et al<sup>5</sup>. In this case the GB resembles a linear, periodic chain of 5-8 rings and it has a metallic nature (i.e., non-zero density of states at the Fermi level). The interested reader can find more information on structural defects in graphene in three recent reviews on the topic<sup>12,16,17</sup>.

3

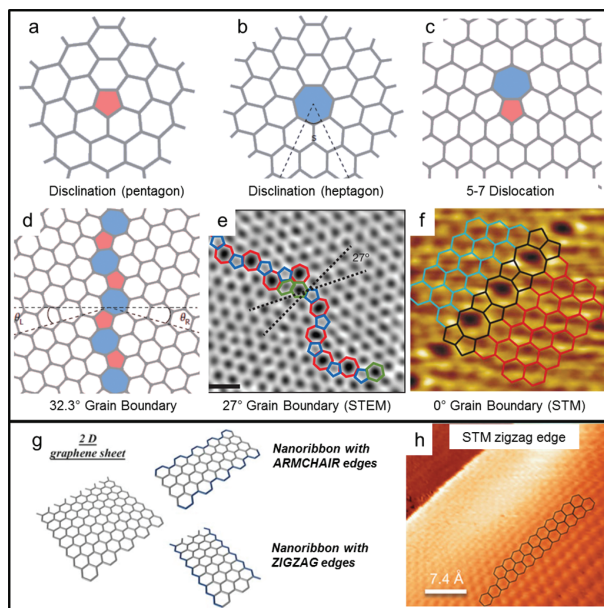


**Figure 3.2. (a-f) Topological defects in graphene.** (a,b) 5 ring and 7 ring disclinations, (c) 5-7 dislocation, (d) grain boundary with  $\theta=32.3^\circ$  misorientation angle. Reprinted with permission from ref 16. Copyright 2014 Nature Publishing Group. (e) Aberration-corrected annular dark-field scanning TEM of a grain boundary with  $\theta=27^\circ$  misorientation angle. Scale bar is 0.5 nm. Reprinted with permission from ref 28. Copyright 2011 Nature Publishing Group. (f) STM image of a  $0^\circ$  grain boundary, formed by 5 and 8 carbon atom rings. Reprinted with permission from ref 5. Copyright 2010 Nature Publishing Group. (g) Zig-zag and armchair edges in monolayer graphene nanoribbons. Reprinted with permission from ref 20. Copyright 2010 Royal Society of Chemistry. (h) Atomic resolution STM image of graphene edge structure on the sloped sidewall of SiC. Reprinted with permission from ref 19. Copyright 2014 Nature Publishing Group.

### 3.1.2 EDGE DEFECTS IN GRAPHENE NANORIBBONS

A graphene nanoribbon (GNR) is a narrow strip of graphene (width ranging from 1 to 100 nm) with a large length to width ratio. When the width of the nanoribbon is reduced below 20 nm, a sizeable band gap can be opened in the band structure. The size of this band gap has been theoretically predicted to be in the 0.2-1.5 eV range<sup>18</sup>, depending both on the GNR width and on its edge orientation (zig-zag or armchair, see Figure 3.2g). The presence of a band gap makes GNRs good candidates for replacing traditional semiconductors in

electronic devices such as Field Effect Transistors, tunnel barriers, and quantum dots.

3 | Depending on the method adopted for GNRs fabrication, the experimental band gap and mobility differ quite radically from the predicted values. The explanation for this behavior is mainly given by the presence of defects on the GNR edges, which alter the normal zig-zag or armchair edge profiles and create localized states along the length of the GNR. This happened for example in fabrication using electron-beam lithography, followed by oxygen plasma etching, which yields GNRs with rough edges. Stampfer et al.<sup>3</sup> have shown that a GNR fabricated following such method behaves as a series of quantum dots, which gives an “effective energy band gap” of 110-340 meV, roughly ten times higher than the predicted value (8 meV) in a 45 nm wide GNR. On the other hand, a recent experiment by Baringhaus et al.<sup>19</sup> showed ballistic transport in GNR grown on the sidewalls of etched steps in SiC. As revealed by STM images (see Figure 3.2h), these GNRs have a well-defined edge orientation and are mostly defect-less, which means that the charge carriers can travel a long distance (mean free path  $\sim 16 \mu\text{m}$ ) before undergoing inelastic scattering. These, and many other experiments, highlight the importance of controlling the quality, and the orientation, of GNR edges. For more details on GNRs, their edges and fabrication methods, we point the reader to specific reviews<sup>20,21</sup>.

## 3.2 GRAPHENE SELF-HEALING AND RECRYSTALLIZATION

Graphitization of thin carbon films (i.e., the process of graphite formation from amorphous carbon) was extensively studied in the 1980's<sup>22</sup>. These experiments were carried out ex-situ, where each sample was individually heated at a fixed temperature and imaged afterwards in a TEM. It was found that graphitization takes place progressively in a temperature range of 2000°C- 3000°C. Almost 30 years later, prompted by the renewed interest in graphene, the topic of lattice recrystallization (or “healing”) was addressed with more modern, practical, in-situ approaches. Here we present four recent in-situ (S)TEM experiments that use different approaches to achieve graphene lattice recrystallization. These include ultra-high vacuum (UHV) healing<sup>23</sup>, silicon-assisted growth<sup>7</sup>, high-temperature healing<sup>24</sup> and recrystallization by Joule heating<sup>9</sup>. We emphasize that, to achieve atomic resolution imaging, graphene is always freestanding in these experiments.

### 3.2.1 GRAPHENE ULTRA-HIGH VACUUM HEALING AND METAL CATALYZED ETCHING AT ROOM-TEMPERATURE

In the research conducted by Zan and collaborators<sup>23</sup>, Ni and Pd metal particles were evaporated on top of CVD graphene and imaged with a STEM microscope in UHV ( $6 \times 10^{-9}$  mbar). Under the effect of 60 keV electron beam scanning, these metal particles acted as catalysts for etching holes in the graphene surface (see Figures 3.3a,b). In fact, the low energy of the electron beam itself would not be sufficient to create new vacancies in the

bulk lattice (as the threshold for knock-on damage of single carbon atoms in graphene is  $86\text{keV}^{10}$ ), but it could be enough to displace atoms at graphene edges. The threshold for removing atoms at the edges has been calculated to be  $62\text{keV}$  (zig-zag profile)<sup>25</sup>, which could be further lowered by the presence of the metal catalysts.

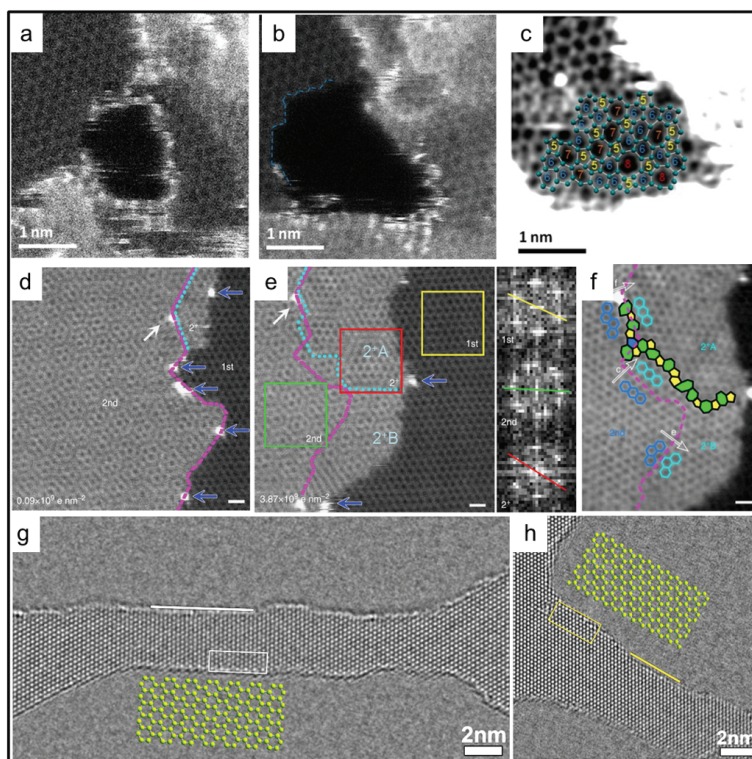


**Figure 3.3. Graphene self-repair experiments.** (a-c) Aberration-corrected high-angle annular dark-field scanning TEM (@60 keV) images showing (a) a hole etched in graphene that is decorated with Pd atoms, (b) the stabilization of the hole in the absence of Pd atoms at the edge, and (c) the hole refilling with 5,6,7 and 8 carbon atom rings. The sample is at room temperature, in ultra-high vacuum. Reprinted with permission from ref 23. (d-f) Aberration-corrected annular dark-field scanning TEM (@60 keV) images showing (d) a graphene area which is single layer on the right side and bilayer on the left, (e) the same area after a cumulative electron dose of  $3.87 \times 10^{19} \text{ e nm}^{-2}$ . The inset shows the Fourier transform images corresponding to the 1st (yellow box), 2nd (green box) and 2+ (red box) layer of graphene. (f) A detail of the previous picture, showing the grain boundary formed between the newly grown graphene (2+A and 2+B) and the original 2nd layer. The sample is heated to  $500^\circ\text{C}$ . Scale bar is 0.5 nm. Reprinted with permission from ref 7. Copyright 2014 Nature Publishing Group. (g-h) HRTEM images of nanoribbons in monolayer graphene sculpted at 300 keV at  $600^\circ\text{C}$  and imaged at 80 keV at  $600^\circ\text{C}$ . The ribbons in (g) and (h) are oriented respectively along the  $\langle 1\bar{1}00 \rangle$  and  $\langle 1\bar{2}00 \rangle$  direction. White and yellow lines indicate armchair and zig-zag edges, respectively. Atom structure models for armchair and zig-zag edges, outlined with open frames in the corresponding images, are enlarged and overlaid. Reprinted with permission from ref 24.



Without the metal particles, the authors observed re-filling and repairing of the holes, under the same electron beam irradiation. As the whole experiment was conducted at room temperature, any heat-related repair process can be discarded. The authors concluded that the scanning electron beam could dislodge carbon adatoms from the graphene surface, and drag them to the edge of the holes. There, they could rearrange in a random combination of 5,6,7 or 8 carbon atom rings and refill the hole (see Figure 3.3c).

### 3.2.2 SILICON-ASSISTED GROWTH OF GRAPHENE AT HIGH TEMPERATURE

In another experiment, Liu et al.<sup>7</sup> observed silicon-catalyzed graphene growth. A STEM microscope (operated at 60 keV) in high vacuum ( $1 \times 10^{-7}$  mbar) was used to image CVD bilayer graphene, and simultaneously heated to 500°C with an in-situ TEM heating holder. The carbon needed for the growth originated from the hydrocarbons in the vacuum chamber of the microscope, after being decomposed on graphene by the electron beam (no growth was observed in areas not exposed by the electron beam). In contrast to the previously discussed experiment<sup>23</sup>, room temperature imaging did not result in hole re-filling, but simply in amorphous carbon deposition. This can be explained by the different vacuum conditions of the two microscopes: in worse vacuum conditions there are more hydrocarbons available, resulting in a higher beam-induced carbon deposition rate. If this rate is too high, carbon atoms cannot form covalent bonds and keep accumulating in amorphous layers. Water molecules on graphene surface (not completely removed in high-vacuum) may also play a role in this process, catalyzing the deposition of amorphous carbon.

An example of the observed graphene growth is shown in Figures 3.3d-f. Looking at Figure 3.3d, the 1st layer area on the right is gradually covered by a 2nd layer of graphene, extending from the left side. Silicon atoms (blue arrows) catalyze the growth and are pushed to the outermost edges of the newly formed graphene. As the authors explain, the graphene can either grow in the same crystal orientation as the seeding layer (layer 2+B in Figures 3.3e,f), or it can be rotated by 30° (layer 2+A). In the latter case, a grain boundary is formed. The rotation is caused by the presence of 5-7 edge defects in the original seeding layer, before the growth had started. This proves that in few-layer graphene heated at 500°C, the growing orientation mainly follows the edge structure, rather than the energetically favorable AB stacking.

### 3.2.3 GRAPHENE STEM SCULPTING AT HIGH TEMPERATURE

In the third experiment that we present, Xu et al.<sup>24</sup> used the STEM electron beam to sculpt graphene nanoribbons with 2 nm width and crystalline edges with defined orientation. In this case, the microscope was operated at 300 keV in order to physically knock the carbon atoms away from the lattice. Graphene was simultaneously heated to 600° C using a dedicated in-situ TEM holder. During the imaging process, the electron beam scanned the graphene surface with a short dwell time (10 μs). This only rarely created vacancies in the

lattice, which were instantly repaired by refilling with carbon adatoms (highly mobile at 600°C) present on the surface of graphene. When the dwell time was increased (10 ms), the beam-induced damage extended beyond repair, and a hole was formed in the graphene. Using a computer script to slowly move the beam along a pre-defined path, the authors could pattern graphene nanoribbons and nanopores with sub-nm accuracy. The edges of the patterned nanostructures maintained their crystalline structure because of the 600°C temperature. Figures 3.3g,h show an example of two graphene nanoribbons, sculpted following either zig-zag or armchair direction, exhibiting atomically sharp edges. This chapter, rather than presenting a new graphene repair mechanism, exploits the high-temperature healing effects to achieve mask-less, resist-free and defect-free graphene patterning. With a few modifications, the method could also be extended to industrial e-beam lithography machines.

#### 3.2.4 GRAPHENE NANORIBBON EDGE RECRYSTALLIZATION INDUCED BY JOULE HEATING

In this issue of ACS Nano<sup>9</sup>, Qi and his co-workers correlate, in real-time, the conductivity of a graphene nanoribbon with its crystallinity, which is monitored at the atomic scale with High Resolution TEM imaging. Starting from an 8 nm wide multilayer graphene nanoribbon with rough edges (see Figure 3a in ref 9), an increasing voltage (2-3 V) is applied across it, resulting in Joule heating and local temperatures that exceed 2000 K. This heating induces recrystallization of the nanoribbon edges, which rearrange along either zig-zag or armchair profile (see Figure 3.3b-d in ref 9). As the voltage is increased and the temperature rises, the edges become smoother, the ribbon width shrinks, and the number of layers decreases (see Figure 3e-g in ref 9). This recrystallization resulted in an overall increase in conductivity, despite the reduced width of the ribbon (see Figure 5a,b in ref 9). This is an important, direct experimental confirmation of the influence of edge roughness and lattice crystallinity on graphene electronic transport.

To further explain the mechanism of edge smoothing induced by Joule heating, Monte-Carlo simulations were implemented. It was found that junctions between edges with different orientation (zig-zag or armchair) develop a larger electrical resistance, which results in a higher local heat dissipation and thus, temperature. Consequently, any edge protrusion was subject to a fast recrystallization, and promptly flattened into a smooth edge.

One consequence of recrystallization induced by heating (either external or Joule), is the systematic formation of bonded edges (see Figure 6a in ref 9). Any open edge in a bilayer, or multilayer, graphene sheet will “fuse” with the closest free edge available, as shown in Figure 3.2a-f from ref 9. For electro-chemical studies, this could represent a disadvantage because there are no dangling bonds available for chemical functionalization. On the other

hand, bilayer graphene nanoribbons with closed edges could, in theory, have a finite band gap (up to 0.25 eV), depending on the twist angle between the two layers.

As a final remark, we note that a similar experiment was performed a few years ago by Jia et al.<sup>26</sup>. However, in that experiment there was no correlation between width and conductivity of the sample, nor any consideration on the number of graphene layers or the presence of bonded edges.

### 3.3 OUTLOOK AND FUTURE CHALLENGES

Different repair mechanisms of defects in graphene have been observed. Most of them are based on high temperature annealing (>500°C) and they require a carbon source to be initiated. The carbon is usually available as free ad-atoms on graphene surface, but it can also be provided by the hydrocarbons present in the vacuum chamber of the TEM. Controlled Joule heating can be used to recrystallize the rough edges of plasma etched graphene nanoribbons, where the current flowing through the nanoribbons is regulated in order to induce self-repair, without causing physical breakdown.

The results obtained by Qi et al.<sup>9</sup> highlight that in-situ TEM is the optimal instrument to study the effects of lattice repair on graphene conductivity. With small modifications, the experiment could be repeated on single layer graphene and other two-dimensional materials, such as layered transition metal dichalcogenides ( $\text{MoS}_2$ ,  $\text{WSe}_2$ ,  $\text{MoSe}_2$ ,  $\text{WS}_2$ , etc.), phosphorene, silicene, and many others.

While the current focus of the field is on controlling the annealing processes in such a way that one can make defect-free graphene nanostructures, a next stage will likely be to deliberately create single defects within perfect graphene (e.g., a small pore, a single step in a zigzag edge, or replacing a single C atom by a Pt atom) with the same level of perfection. This opens up many applications from electronic devices to catalysis. For example, with STEM one could create a vacancy inside a graphene nanoribbon at a pre-chosen site, refill it by a Si or Pt adatom, and subsequently explore the interaction of a single Pt atom with  $\text{H}_2$  or other gases in an environmental TEM. To fabricate graphene nanostructures, the fine probe of STEM can be optimally used for sculpting on an atomic level and in any shape, with higher precision than conventional TEM. To verify what has been made, one can use the same STEM, but with a voltage below the knock-on energy. Thus, for optimal operation one needs a STEM that can rapidly switch from 100 keV (sculpting) to 60 keV (imaging). An interesting geometry to sculpt in graphene would be a nanoribbon with a nanopore in its center. In fact, it has been hypothesized that this configuration could be used for sequencing DNA with single-base resolution<sup>27</sup>.

These and other future experiments will pave the way for the fabrication of reliable,

defect-controlled graphene devices. In-situ TEM plays a crucial role in this expedition, as it provides a wonderful workbench for real-time graphene engineering.

## REFERENCES

1. Haskins, J.; Kinaci, A.; Sevik, C.; Sevinçli, H.; Cuniberti, G.; Çain, T. Control of Thermal and Electronic Transport in Defect-Engineered Graphene Nanoribbons. *ACS Nano* 2011, 5, 3779–3787.
2. Tsen, A. W.; Brown, L.; Levendorf, M. P.; Ghahari, F.; Huang, P. Y.; Havener, R. W.; Ruiz-Vargas, C. S.; Muller, D. A.; Kim, P.; Park, J. Tailoring Electrical Transport Across Grain Boundaries in Polycrystalline Graphene. *Science* 2012, 336, 1143–1146.
3. Stampfer, C.; Güttinger, J.; Hellmüller, S.; Molitor, F.; Ensslin, K.; Ihn, T. Energy Gaps in Etched Graphene Nanoribbons. *Phys. Rev. Lett.* 2009, 102, 056403.
4. Lherbier, A.; Dubois, S. M.-M.; Declerck, X.; Niquet, Y.-M.; Roche, S.; Charlier, J.-C. Transport Properties of Graphene Containing Structural Defects. *Phys. Rev. B* 2012, 86, 075402.
5. Lahiri, J.; Lin, Y.; Bozkurt, P.; Oleynik, I. I.; Batzill, M. An Extended Defect in Graphene as a Metallic Wire. *Nat. Nanotechnol.* 2010, 5, 326–329.
6. Zazyev, O. V.; Louie, S. G. Electronic Transport in Polycrystalline Graphene. *Nat. Mater.* 2010, 9, 806–809.
7. Liu, Z.; Lin, Y.-C.; Lu, C.-C.; Yeh, C.-H.; Chiu, P.-W.; Iijima, S.; Suenaga, K. In Situ Observation of Step-Edge in-Plane Growth of Graphene in a STEM. *Nat. Commun.* 2014, 5.
8. Song, B.; Schneider, G. F.; Xu, Q.; Pandraud, G.; Dekker, C.; Zandbergen, H. Atomic-Scale Electron-Beam Sculpting of Near-Defect-Free Graphene Nanostructures. *Nano Lett.* 2011, 11, 2247–2250.
9. Qi, Z. J.; Daniels, C.; Hong, S. J.; Park, Y. W.; Meunier, V.; Drndić, M.; Johnson, A. T. C. Electronic Transport of Recrystallized Freestanding Graphene Nanoribbons. *ACS Nano* 2015.
10. Smith, B. W.; Luzzi, D. E. Electron Irradiation Effects in Single Wall Carbon Nanotubes. *J. Appl. Phys.* 2001, 90, 3509–3515.
11. Chen, J.-H.; Cullen, W. G.; Jang, C.; Fuhrer, M. S.; Williams, E. D. Defect Scattering in Graphene. *Phys. Rev. Lett.* 2009, 102, 236805.
12. Banhart, F.; Kotakoski, J.; Krasheninnikov, A. V. Structural Defects in Graphene. *ACS Nano* 2011, 5, 26–41.
13. Kotakoski, J.; Krasheninnikov, A. V.; Kaiser, U.; Meyer, J. C. From Point Defects in Graphene to Two-Dimensional Amorphous Carbon. *Phys. Rev. Lett.* 2011, 106, 105505.
14. Wang, H.; Wang, Q.; Cheng, Y.; Li, K.; Yao, Y.; Zhang, Q.; Dong, C.; Wang, P.; Schwingenschlögl, U.; Yang, W.; et al. Doping Monolayer Graphene with Single Atom Substitutions. *Nano Lett.* 2012, 12, 141–144.

15. Zhao, L.; He, R.; Rim, K. T.; Schiros, T.; Kim, K. S.; Zhou, H.; Gutiérrez, C.; Chockalingam, S. P.; Arguello, C. J.; Pálová, L.; et al. Visualizing Individual Nitrogen Dopants in Monolayer Graphene. *Science* 2011, 333, 999–1003.
16. Yazyev, O. V.; Chen, Y. P. Polycrystalline Graphene and Other Two-Dimensional Materials. *Nat. Nanotechnol.* 2014, 9, 755–767.
17. Cummings, A. W.; Duong, D. L.; Nguyen, V. L.; Van Tuan, D.; Kotakoski, J.; Barrios Vargas, J. E.; Lee, Y. H.; Roche, S. Charge Transport in Polycrystalline Graphene: Challenges and Opportunities. *Adv.Mater.* 2014, 26, 5079–5094.
18. Son, Y.-W.; Cohen, M. L.; Louie, S. G. Energy Gaps in Graphene Nanoribbons. *Phys. Rev. Lett.* 2006, 97, 216803.
19. Baringhaus, J.; Ruan, M.; Edler, F.; Tejada, A.; Sicot, M.; Taleb-Ibrahimi, A.; Li, A.-P.; Jiang, Z.; Conrad, E. H.; Berger, C.; et al. Exceptional Ballistic Transport in Epitaxial Graphene Nanoribbons. *Nature* 2014, 506, 349–354.
20. Jia, X.; Campos-Delgado, J.; Terrones, M.; Meunier, V.; Dresselhaus, M. S. Graphene Edges: A Review of Their Fabrication and Characterization. *Nanoscale* 2011, 3, 86–95.
21. Ma, L.; Wang, J.; Ding, F. Recent Progress and Challenges in Graphene Nanoribbon Synthesis. *ChemPhysChem* 2013, 14, 47–54.
22. Goma, J.; Oberlin, M. Graphitization of Thin Carbon Films. *Thin Solid Films* 1980, 65, 221–232.
23. Zan, R.; Ramasse, Q. M.; Bangert, U.; Novoselov, K. S. Graphene Reknits Its Holes. *Nano Lett.* 2012, 12, 3936–3940.
24. Xu, Q.; Wu, M.-Y.; Schneider, G. F.; Houben, L.; Malladi, S. K.; Dekker, C.; Yucelen, E.; Dunin-Borkowski, R. E.; Zandbergen, H. W. Controllable Atomic Scale Patterning of Freestanding Monolayer Graphene at Elevated Temperature. *ACS Nano* 2013, 7, 1566–1572.
25. Kotakoski, J.; Santos-Cottin, D.; Krasheninnikov, A. V. Stability of Graphene Edges under Electron Beam: Equilibrium Energetics versus Dynamic Effects. *ACS Nano* 2012, 6, 671–676.
26. Jia, X.; Hofmann, M.; Meunier, V.; Sumpter, B. G.; Campos-Delgado, J.; Romo-Herrera, J. M.; Son, H.; Hsieh, Y.-P.; Reina, A.; Kong, J.; et al. Controlled Formation of Sharp Zigzag and Armchair Edges in Graphitic Nanoribbons. *Science* 2009, 323, 1701–1705.
27. Saha, K. K.; Drndić, M.; Nikolić, B. K. DNA Base-Specific Modulation of Microampere Transverse Edge Currents through a Metallic Graphene Nanoribbon with a Nanopore. *Nano Lett.* 2012, 12, 50–55.
28. Huang, P. Y.; Ruiz-Vargas, C. S.; van der Zande, A. M.; Whitney, W. S.; Levendorf, M. P.; Kevek, J. W.; Garg, S.; Alden, J. S.; Hustedt, C. J.; Zhu, Y.; et al. Grains and Grain Boundaries in Single-Layer Graphene Atomic Patchwork Quilts. *Nature* 2011, 469, 389–392



# 4

## 1/f NOISE IN GRAPHENE NANOPORES

Graphene nanopores are receiving great attention due to their atomically thin membrane and intrinsic electrical properties that appear greatly beneficial for biosensing and DNA sequencing. Here, we present an extensive study of the low-frequency  $1/f$  noise in the ionic current through graphene nanopores, and compare it to noise levels in silicon nitride pore currents. We find that the  $1/f$  noise magnitude is very high for graphene nanopores, typically two orders of magnitude higher than for silicon nitride pores. This is a drawback as it significantly lowers the signal-to-noise ratio in DNA translocation experiments. We evaluate possible explanations for these exceptionally high noise levels in graphene pores. From examining the noise for pores of different diameters and at various salt concentrations, we find that, in contrast to silicon nitride pores, the  $1/f$  noise in graphene pores does not follow Hooge's relation. In addition, from studying the dependence on the buffer pH, we show that the increased noise cannot be explained by charge fluctuations of chemical groups on the pore rim. Finally, we compare single and bilayer graphene to few-layer and multi-layer graphene and boron nitride (h-BN), and we find that the noise reduces with layer thickness for both materials, which suggests that mechanical fluctuations may be the underlying cause of the high  $1/f$  noise levels in monolayer graphene nanopore devices.

---

This chapter has been published as: S.J. Heerema, G.F. Schneider, M. Rozemuller, L. Vicarelli, H.W. Zandbergen and C. Dekker. *Nanotechnology* 26, 074001 (2015).



## 4.1 INTRODUCTION

The nanopore field is mainly driven by the demand for a single-molecule DNA sequencing technique that reads DNA bases in a label-free, fast and accurate fashion. Although promising proof-of-principle results have been published using biological pores like MspA<sup>1</sup>, solid-state nanopores provide some important advantages over biological pores, such as stability, adjustable geometry, and the ability of integration into device<sup>2,3</sup>. Graphene is a special advantageous type of solid-state nanopore as it is electrically conducting and atomically thin and therefore potentially provides the capability to reach single-nucleotide resolution in detection. Indeed, various theoretical proposals indicate that its intrinsic electrical properties can be exploited to distinguish different DNA bases<sup>4-12</sup>.

In nanopore experiments, charged biomolecules (like DNA) in an ionic solution are driven through a nanometer-sized hole by an applied trans-membrane voltage. The applied bias voltage induces an ion current that prevails due to reversible electrochemical reactions at the electrodes on either side of the membrane. During translocation, the molecule partially blocks the pore, resulting in a temporal change in the ion current, representing the signal. To maximize the signal-to-noise ratio in translocation experiments, any baseline current fluctuations should be minimized, and in order to do so, the origin of these fluctuations should be understood. For these reasons, current noise in biological pores as well as in solid-state nanopores has been extensively studied<sup>13-19</sup>. Noise studies in graphene nanopores, however, have so far been rare<sup>20</sup>

In order to evaluate the current fluctuations in pore currents, one calculates the current power spectral density  $S_I$ , which represents the current power distribution over frequency. Generally, the noise spectrum in nanopore systems is divided into a low-frequency regime ( $f < \sim 1$  kHz) and a high-frequency regime ( $f > \sim 1$  kHz). Whereas the high-frequency noise power is dominated by the membrane capacitance<sup>21</sup>, the low-frequency noise in solid-state nanopores as well as in biological nanopores is characterized by a  $1/f$  dependence<sup>13,15,22</sup>. Such low-frequency  $1/f$  noise is a ubiquitous phenomenon, characterised by an inverse dependence of current spectral density on frequency  $S_I \sim 1/f^\gamma$  where  $f$  is frequency and  $\gamma \sim 1$ <sup>23</sup>. Because of its prominent occurrence in most electronic systems (and its implications for their performance),  $1/f$  noise has been profoundly studied over the past decades. Despite all these studies, the origin of  $1/f$  noise is often still under debate. It is generally accepted that there is not a single physical mechanism that generates this type of noise<sup>24</sup>. Models propose that  $1/f$  noise is related to fluctuations in the number of charge carriers ( $N$ ), in the mobilities of charge carriers ( $\mu$ ), or in both<sup>25</sup>.

Larger current leads to larger current fluctuations, and therefore to higher noise. To obtain a measure for the noise magnitude that can compare the noise levels for various bias con-

ditions, one divides the current power spectral density  $S_I$  by the squared current amplitude:

$$\frac{S_I}{I^2} = \frac{C_{LF}}{f} \quad (1)$$

where  $C_{LF}$  represents the low-frequency noise amplitude. A very commonly used relation in 1/f studies is Hooge's empirical relation  $C_{LF} = \alpha_H/N$ , which inversely relates the relative noise magnitude  $C_{LF}$  to the relevant number of charge carriers  $N$  via Hooge's parameter  $\alpha_H$ <sup>26</sup>. This model has been shown to provide a fair description of the noise in many different electronic circuits as well as for ionic current systems<sup>27</sup>. Importantly, the relation was also shown to provide a good description for the 1/f noise in silicon nitride nanopores<sup>15</sup>.

Here, we discuss the low-frequency noise in graphene nanopores and compare it to noise in silicon nitride pores. We did an extensive study in which we analysed 45 graphene pores, 24 silicon nitride pores, and 7 boron nitride pores. We show that the 1/f noise for graphene nanopores is on average 2 orders of magnitude higher than for silicon nitride pores. We discuss possible explanations for this high 1/f noise in graphene pores. In order to do so, we assess whether Hooge' relation holds by examining the noise properties at various pore sizes and salt concentrations. Additionally, we probe for charged edge interactions by varying the buffer pH. Finally, we discuss the effect of graphene layer thickness and compare it to that of another layered material, boron nitride.

## 4.2 RESULTS AND DISCUSSION

Graphene nanopores were fabricated by high-temperature TEM drilling, see Methods. Figure 4.1a provides two typical ionic current traces for a monolayer graphene pore ( $R=12.2 \text{ M}\Omega$ ,  $d=10\text{nm}$ ) and a silicon nitride pore ( $R=7.8 \text{ M}\Omega$ ,  $d=20\text{nm}$ ). Both traces are recorded at 100mV bias voltage and processed in exactly the same way (low-pass filtered with an 8-pole Bessel filter at 10kHz, and smoothed by calculation of the moving average of four data points in logarithmic space). It is very clear that the graphene pore current exhibits pronounced noise in the ionic current. Figure 4.1b shows the corresponding noise spectra, where the current power spectral densities  $S_I$  are plotted against frequency in logarithmic space. The noise spectrum of the graphene pore is found to be dominated by a 1/f dependence, extending up to the filter frequency of 10kHz. Note that, by contrast, the 1/f regime for the silicon nitride pore halts at about 400 Hz, where thermal noise becomes dominant. For reference, we also show the background noise of the amplifier that is recorded at 0mV. The noise in the graphene pore current is observed to be more than two orders of magnitude higher than that for the silicon nitride current. Figure 4.1c plots the current power spectral densities  $S_I$  at varying voltage levels for the same graphene pore. As expected, the noise levels depend on the magnitude of the current, i.e. larger currents lead to higher 1/f noise levels. Indeed, as is shown in Figure 4.1d, the normalised power spectral densities ( $S_I/I^2$ ) exhibit the same

low-frequency noise magnitude. The  $1/f$  regimes are linearly fitted in logarithmic space, where the fit intercept at 1Hz ( $S_i(1\text{Hz})/I^2$ ) represents the dimensionless low-frequency noise coefficient  $C_{LF}$ , which is the magnitude of the pore-specific low-frequency  $1/f$  noise.

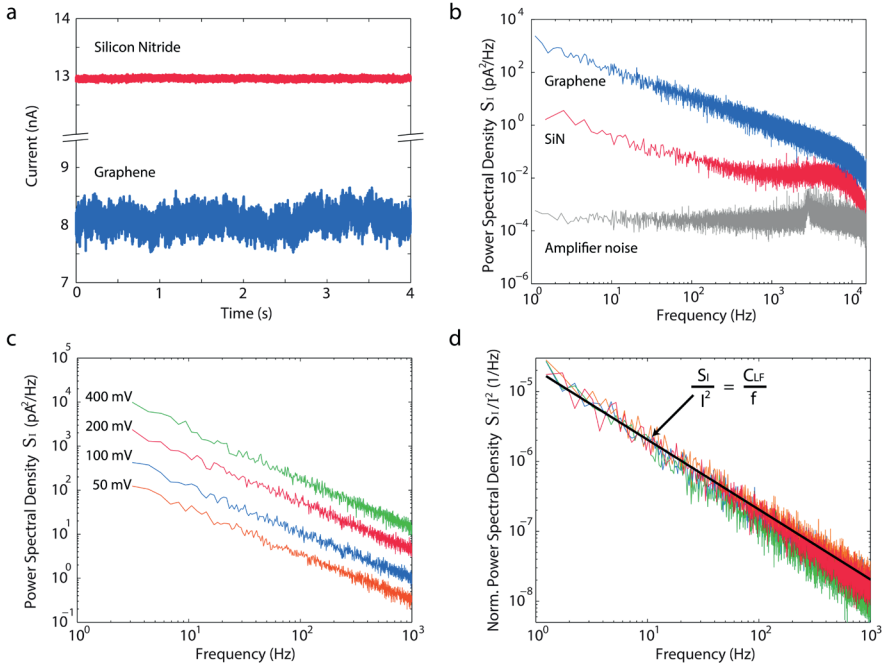


**Figure 4.1:  $1/f$  noise in graphene nanopores and silicon nitride pores.** (a) Typical current traces for a graphene pore ( $R=12.2$  M $\Omega$ ,  $d=10$ nm) in blue and a silicon nitride pore ( $R=7.8$  M $\Omega$ ,  $d=20$ nm) in red. The ionic current through the graphene pore shows significant low-frequency variations. (b) Spectral densities of the graphene and silicon nitride pores from panel a. The  $1/f$  frequency in the silicon nitride pore is about two orders of magnitude lower and stretches up to 400 Hz, whereas the graphene pore shows  $1/f$  noise up to the low-pass filter frequency 10 kHz. For presentation, the data were smoothed by calculation of a walking average of 20 data points (c) Spectral densities at various bias voltages for the same graphene pore. As expected, the curves are bias-voltage dependent. (d) The normalized spectral densities  $S_i/I^2$  collapse onto the same curve. A linear fit of these curves yields the low-frequency noise coefficient  $C_{LF}$  that represents the magnitude of the  $1/f$  noise. The curves in panel c and d were smoothed by a walking average of 40 data points.

With the noise characterization method in place, we can now compare the low-frequency  $1/f$  noise magnitude  $C_{LF}$  for a variety of pores and measurement conditions. We compared 45 mono- and bilayer graphene pores to 24 silicon nitride pores. All current traces are recorded at 100mV at 1M KCl salt concentration and 10mM Tris-HCl at pH 8.1. The results of all  $1/f$  noise analyses are presented in histograms in Figure 4.2a. The black curves depict log-normal distributions exhibiting an average  $1/f$  coefficient  $\langle C_{LF} \rangle = 6.3 \times 10^{-6}$  for graphene pores, and an average  $1/f$  coefficient  $\langle C_{LF} \rangle = 4.4 \times 10^{-8}$  for silicon nitride pores. On average, the  $1/f$  noise in graphene pores thus is about two orders of magnitude higher

than in silicon nitride pores. In logarithmic space, the averages of the distributions are represented as  $\log(\langle C_{LF} \rangle) = -5.2 \pm 0.6$  for graphene and  $\log(\langle C_{LF} \rangle) = -7.4 \pm 0.9$  for silicon nitride. The width of the distribution for the silicon nitride samples is larger, which likely is due to a larger variance in pore shape associated with the three-dimensional geometry of the pore.

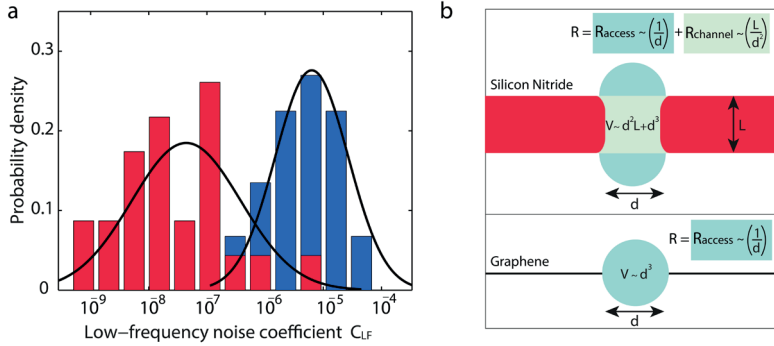


**Figure 4.2:** (a) Probability distributions of low-frequency noise coefficients  $C_{LF}$  of silicon nitride (red) and graphene nanopores (blue). We compare 24 silicon nitride pores to 45 graphene pores. Linear fits of  $S_f/I^2$  are made over the  $1/f$  regimes (For graphene pores this band is 1-1000Hz; in silicon nitride pores the  $1/f$  regime stretches only up to  $\sim 200$ Hz, where thermal noise starts to become dominant). We find average values of  $C_{LF} = 4.4 \times 10^{-8}$  for silicon nitride and  $C_{LF} = 6.3 \times 10^{-6}$  for graphene pores, a difference of more than two orders of magnitude. All measurements are done at 1M KCl, 10mM Tris-HCl, pH 8.1. (b) Schematic representation of the geometrical differences between silicon nitride and graphene nanopores. Expressions for the pore volume  $V$  and pore resistance  $R$  are indicated.

What explains this significant difference in  $1/f$  noise amplitudes between graphene and silicon nitride nanopores? Conductance fluctuations are most likely caused inside or nearby the pore as this dominates the circuit's resistance. The geometries of the two different types of pores are sketched in Figure 4.2b. For silicon nitride pores the resistance can be approximated by  $R = \sigma^{-1} \left[ \frac{4L}{\pi d^2} + \frac{1}{d} \right]$ , where  $\sigma$  represents the bulk conductivity,  $L$  is the pore length, and  $d$  the pore diameter<sup>28</sup>. The first term represents the pore channel resistance that relates to both the pore length and diameter. The second term denotes the total access resistance that accounts for the convergence of field lines by the pore for both membrane sides<sup>29</sup>. In graphene pores, the resistance is completely dominated by the access resistance  $R = \sigma^{-1} \frac{1}{d}$ . The relevant pore volume for silicon nitride pores consists of the cylindrical volume  $d^2L$  and a term that represents the volumes adjacent to the pore mouths. For each side, this can be regarded to roughly resemble a hemisphere with a size that is set by the pore diameter, located at the centre of the pore mouth. Hence, we consider the effective volume of silicon nitride pores to be determined by  $V \sim d^2L + d^3$ . For graphene pores the pore length approximates zero, and we thus regard the relevant volume to simply scale as  $V \sim d^3$ .

We investigated the dependence of the  $1/f$  noise on pore geometry for graphene pores. Figure 4.3a plots the  $1/f$  noise as a function of pore diameter. The diameters are determined from TEM images obtained directly after drilling. Although there is appreciable scatter in the data, there seems to be a correlation between size and  $1/f$  noise, where large pores have lower noise. A linear fit in logarithmic space yields a dependence of  $C_{LF} \sim d^{-\gamma_1}$ , with  $\gamma_1 = 1.8 \pm 0.6$ . Additionally, we investigated how the noise scales with the pore resistance, where the resistance values were obtained by linear fitting of recorded IV curves. Figure 4.3b plots the noise coefficients versus resistance in logarithmic space and a corresponding linear fit yields  $C_{LF} \sim R^{\gamma_2}$  with  $\gamma_2 = 1.4 \pm 0.4$ . The Hooge model predicts that the number of charge carriers  $N$  inside the pore is the important variable, which should be given by the number of ions in the pore volume that determines the resistance. According to Hooge's relation the  $1/f$  noise thus should scale to both the pore diameter and pore resistance with a power law of  $\gamma_1 = \gamma_2 = 3$ , which is not observed in the data where we observe  $\gamma_1 = 1.8 \pm 0.6$  and  $\gamma_2 = 1.4 \pm 0.4$ .

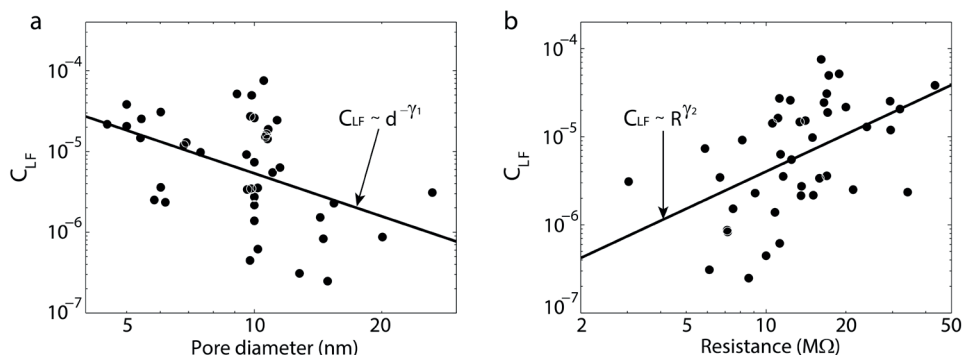


**Figure 4.3** (a)  $C_{LF}$  vs pore diameter, plotted double logarithmically. The black line represents a linear fit of the data, yielding  $\gamma_1 = 1.8 \pm 0.6$ . (b)  $C_{LF}$  vs pore resistance in logarithmic space. The linear fit of the data yields  $\gamma_2 = 1.4 \pm 0.4$ .

Another approach to investigate whether the noise amplitude scales inversely with the number of charge carriers in the pore volume is to vary the density of charge carriers by changing the salt level of the buffer. A recent report indeed suggested such a dependence for graphene nanopores<sup>20</sup>. We studied the  $1/f$  noise at salt concentrations between 10 mM and 1 M KCl, see Figure 4.4a. The grey lines represent results from individual pores with different pore diameters, ranging between 4 and 20 nm.  $1/f$  noise levels are seen to slightly increase towards lower salt concentrations. The averages of  $C_{LF}$  at 10, 100 and 1000 mM salt are shown in red. Experimentally, we find only a weak dependence of the  $1/f$  noise on salt concentration ( $C_{LF} \sim N^{-0.27 \pm 0.02}$ ). Hooge's relation, however, presented in blue, would predict a much stronger salt dependence ( $C_{LF} \sim N^{-1}$ ). Although the noise thus slightly

increases towards lower salt concentrations, our results thus do not follow Hooge's relation.

Next, we examine an alternative explanation for the increased noise levels in graphene nanopores and discuss whether it can be explained by charge fluctuations in the pore rim that would induce noise in the ionic current. To address this, we attempted to modify chemical groups at the pore edge that may switch between a charged and neutral form, by varying the pH of the buffer. Carboxyl groups, for example, are expected to be formed at the pore rim and may toggle between their protonated and de-protonated state, with a pKa around 5. We hypothesized that these charge fluctuations may cause an increase in low-frequency noise. To test this, we recorded the currents of individual pores at pH values ranging between pH 1 and 10 at 1M KCl (Figure 4.4b). As before, the grey lines represent measurements of individual pores and the red line corresponds to their averages. We find that  $C_{LF}$  is unaffected by pH and thus conclude that charge fluctuations due to carboxyl groups at the pore rim do not constitute a dominant source of 1/f noise.

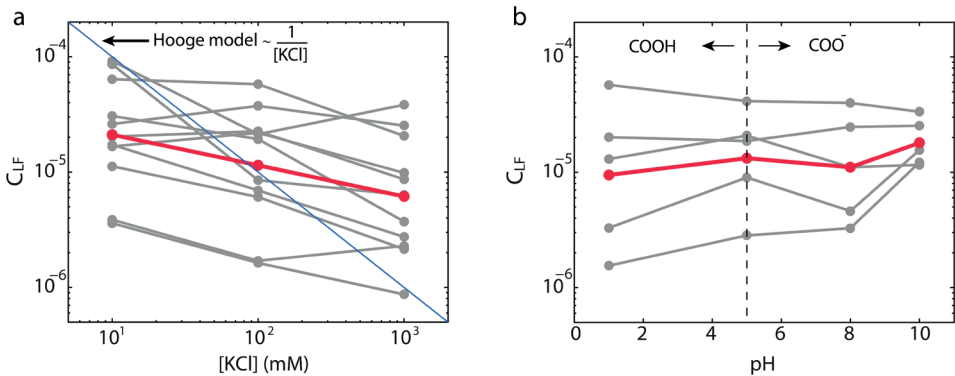


**Figure 4.4** (a) Low-frequency 1/f noise ( $C_{LF}$ ) dependence on salt (KCl) concentration. The grey lines represent results from 10 different pores with diameters between 4 and 20 nm. The red line connects the averages of these at 10mM, 100mM and 1M KCl, all at pH 8.1. Although we find a weak trend ( $N^{-0.27 \pm 0.02}$ ), Hooge's relation is not followed. (b) Low-frequency 1/f noise dependence on pH, measured at pH = 1, 5, 8, 10, for individual pores with pore diameters ranging between 4 and 20nm. We find no correlation between pore diameter and 1/f noise dependence on pH. In the case of toggling of carboxyl (pKa = 5) between its protonated and de-protonated state, one could expect the noise to peak around pH 5, which is not observed.

Finally, we studied the noise levels for different membrane thicknesses, by comparing  $C_{LF}$  of samples with different layer thicknesses. Several multilayer graphene pores (blue) are compared to the monolayer and bilayer graphene pores (black) in Figure 4.5. An increased number of graphene layers leads to lower noise levels. We augmented the dataset by inclusion of boron nitride (h-BN) nanopore data. h-BN is structurally very similar to graphene, with boron and nitride in a honeycomb lattice, forming a similar sp<sup>2</sup> bonded

2-dimensional lattice. We find that the noise in few-layer h-BN is of same order of magnitude as for graphene pores. For multilayers the noise again reduces strongly, about 1.5 orders of magnitude in going from a monolayer to 20 layers. Such a dependence suggests that mechanical properties of graphene may underlie the noise characteristics, with thinner, more flexible layers yielding more noise than thicker and stiffer layers.

4

How should the results for the thickness dependence be interpreted? Few-layered graphene and h-BN, like other two-dimensional membranes, are known to be highly flexible<sup>30</sup>. Mechanical resonators of 1-5 micrometer suspended layered materials have been shown to behave membrane-like for few-layers and plate-like for multilayers<sup>31</sup>. This is likely relevant to our nanopore devices, which have free-standing graphene covering a circular hole with 1  $\mu\text{m}$  diameter. Membrane oscillations can possibly induce fluctuations in the ion flux due to the membrane's movement relative to the ions. In that case, thin 'slack' graphene membranes could induce appreciable low-frequency noise whereas stiff multilayers would exhibit higher frequency oscillations and less low-frequency conductance fluctuations. Molecular dynamics simulations have shown that, related to ion bombardment, fluctuations of the graphene membrane may appear close to the pore<sup>32</sup>. Mechanical resonators of layered materials have been shown to have a 1<sup>st</sup> mode resonance peak in the order of 10 MHz in air<sup>31</sup>. However, such membrane oscillations will be heavily damped due to the water mass that moves along with the membrane. If and in what way such damped oscillations can lead to an increased low-frequency  $1/f$  spectrum, remains a subject for further theoretical studies on the mechanical properties of graphene membranes.

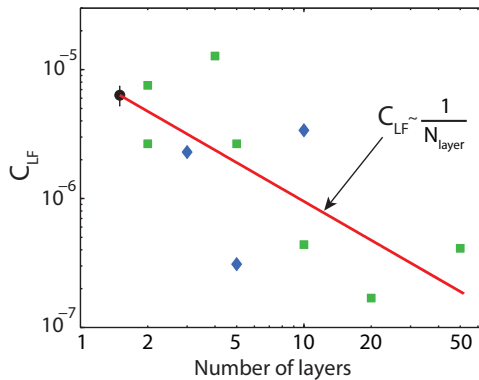


**Figure 4.5: Layer dependence of  $1/f$  noise in graphene and h-BN nanopores.** The black dot represents the mean low frequency coefficient of all monolayer and bilayer graphene nanopores ( $6.3 \times 10^{-6}$ ). The blue dots (diamonds) yield few-layer graphene pores, showing reduced  $1/f$  noise compared to the mean value of monolayer and bilayer graphene pores. The noise in few-layer h-BN pores (green squares) is of same order of magnitude as the few-layer graphene pores. The noise is found to decrease strongly as the layer thickness increases to 20, consistent with a  $C_{LF} \sim 1/N_{\text{layer}}$  dependence (red line). All few-layer and multi-layer pores were 10nm in diameter.

A number of other studies also point in the direction of mechanical fluctuations as the source of the high noise. For example, an experimental study reported that atomic layer deposition (ALD) of several nanometers of titanium oxide reduces the 1/f noise of graphene pores by two orders of magnitude<sup>33</sup>. Similarly, stacked layers of Al<sub>2</sub>O<sub>3</sub> and graphene were shown to exhibit lower noise than pure graphene membranes<sup>34</sup>. The disadvantage of such multilayer or stacked structures is that they elude the single-atom layer thickness, which is one of graphene's greatest advantages to potentially measure at single-nucleotide resolution. In another work, it was apparently possible to reduce the 1/f noise by scaling down the area of suspended graphene to 20nm in diameter, although this was only shown in comparing two individual current traces, it would again point to underlying mechanical fluctuations of the membrane<sup>35</sup>.

### 4.3 CONCLUSION

Here, we have shown that the 1/f noise in monolayer and bilayer graphene nanopores is about two orders of magnitude larger ( $\langle C_{LF} \rangle = 6.3 \times 10^{-6}$ ) than in silicon nitride pores ( $\langle C_{LF} \rangle = 4.4 \times 10^{-8}$ ). In order to explain the high 1/f noise in graphene pores, we studied how it depends on a set of variables. Hooge's model predicts that the 1/f noise is inversely related to the number of charge carriers inside the pore volume, which was shown to describe the noise in silicon nitride nanopores quite well<sup>15</sup>. Remarkably, we found that the 1/f noise in graphene nanopores does not scale with  $d^{-3}$  or  $R^3$ , as Hooge's model would predict. An additional study, in which we varied the salt concentration of the buffer, revealed only a weak dependence of the noise on the number of charge carriers ( $\sim N^{-0.27}$ ), which further disproved Hooge's relation, where a  $N^{-1}$  dependence is expected. Alternatively, we hypothesized that charge fluctuations due to protonation and de-protonation of carboxyl groups at the pore rim could induce noise. In order to test this, we altered the buffer pH between 1 and 10. However, we found that pH has no influence on the noise level and concluded that pH-dependent charge fluctuations at the pore edge do not form the dominant source of noise. Finally, we have shown that 1/f noise in graphene and h-BN pore currents significantly decreases with layer thickness (about 1.5 orders of magnitude in going from a monolayer to 20 layers). We propose that bending fluctuations of the highly flexible graphene or boron nitride membrane may cause the high 1/f noise in the nanopore current.

In conclusion, we have studied the origin of the significant low-frequency 1/f noise in graphene nanopores, and suggest that mechanical fluctuations of the graphene membrane may be the underlying cause. Although this needs to be examined in more detail, it provides a guideline to overcome the high 1/f noise in graphene nanopores and increase signal-to-ratios in further experimental studies, which may accelerate the progress towards a graphene biosensor or sequencer.



#### 4.4 METHODS

**SiN chip fabrication.** A 200nm thick platinum heating coil was deposited on a 200nm low stress silicon nitride layer (LPCVD) on a silicon substrate. Next, a second silicon nitride layer was deposited on top of the platinum coil. After KOH etching a 600x600 micron free-standing SiN membrane was obtained. 1  $\mu\text{m}$ -sized holes were drilled in the silicon nitride membranes with a focussed gallium beam (300 pA) (FEI DualBeam Strata 235). **Graphene transfer.** Monolayer and bilayer graphene flakes were obtained by mechanical exfoliation of natural graphite (NGS Naturgraphit) onto plasma cleaned ( $\text{O}_2$ , Diener) silicon-silicon oxide wafers (90nm) (Graphene Supermarket) using adhesive tape (Nitto - SWT20+). Inspection of monolayer and bilayer graphene was done by optical interference microscopy. Layer thicknesses for few-layered flakes were determined using by optical contrast. Multilayer flake thicknesses were determined by AFM measurements. The flakes were transferred onto the micro-fabricated SiN chips according to the wedging transfer technique, described in [36]. The flakes were transferred onto the silicon nitride membranes. The same procedure was followed for boron nitride pore fabrication.

**TEM drilling of nanopores.** The nanopores were drilled using a FEI Titan 80-300 in STEM mode, operating at an acceleration voltage of 300kV, with a beam diameter of 0.1 nm and a beam current of 0.15 nA. Importantly, graphene was heated at 600°C in order to prevent carbon contamination on the surface and to maintain the crystalline structure up to the pore edge, in order to do so a 10 mA current was passed through the platinum heating coil<sup>37</sup>. Pore diameters varied between 4 and 30 nm, and were measured from the TEM images obtained right after drilling. SiN pores were fabricated as described previously<sup>38</sup>. **Current recording** Chips were cleaned with ethanol and subsequently mounted in a polyether ether ketone (PEEK) flowcell separating two aqueous chambers into which Ag/AgCl electrodes were inserted. Buffers contained 1M KCl solution, 10mM Tris-HCl, pH 8.1 at room temperature. The buffers for the pH measurements contained 1 M KCl and 55mM HCl (pH=1), 0.4 mM NaAc and 4  $\mu\text{M}$  AcAc (pH=5), and 1.6 mM NaOH (pH=10) (Sigma Aldrich). All currents were recorded in absence of DNA in the chambers. Ionic currents were detected using an Axopatch 200B amplifier at 100kHz bandwidth and digitized with a DAQ card at 500 kHz. The current traces were filtered using an 8-pole Bessel filter at 10kHz in Clampfit.

**Data analysis** Power spectral densities were calculated by taking the Fourier transform of the autocorrelation function, divided by the sampling frequency and the sample length. For normalization, the power spectral densities were divided by the mean current of the corresponding traces. In general, the 1/f noise was fitted from 1-1000 Hz for graphene pores and between 1-200 Hz for silicon nitride pores. For data presentation, the curves were smoothed by calculation of a walking average of 4-40 nearest neighbour points. All analyses and fitting is done in Matlab.

## REFERENCES

1. A. H. Laszlo, I. M. Derrington, B. C. Ross, H. Brinkerhoff, A. Adey, I. C. Nova, J. M. Craig, K. W. Langford, J. M. Samson, R. Daza, K. Doering, J. Shendure, and J. H. Gundlach, "Nanopore Sequencing of the phi X 174 genome," p. 11, Jun. 2014.
2. C. Dekker, "Solid-state nanopores.," *Nat. Nanotechnol.*, vol. 2, no. 4, pp. 209–15, Apr. 2007.
3. G. F. Schneider and C. Dekker, "DNA sequencing with nanopores.," *Nat. Biotechnol.*, vol. 30, no. 4, pp. 326–8, Apr. 2012.
4. H. W. C. Postma, "Rapid sequencing of individual DNA molecules in graphene nanogaps.," *Nano Lett.*, vol. 10, no. 2, pp. 420–5, Feb. 2010.
5. T. Nelson, B. Zhang, and O. V. Prezhdo, "Detection of nucleic acids with graphene nanopores: ab initio characterization of a novel sequencing device.," *Nano Lett.*, vol. 10, no. 9, pp. 3237–42, Sep. 2010.
6. S. K. Min, W. Y. Kim, Y. Cho, and K. S. Kim, "Fast DNA sequencing with a graphene-based nanochannel device.," *Nat. Nanotechnol.*, vol. 6, no. 3, pp. 162–5, Mar. 2011.
7. S. M. Avdoshenko, D. Nozaki, C. Gomes da Rocha, J. W. González, M. H. Lee, R. Gutierrez, and G. Cuniberti, "Dynamic and electronic transport properties of DNA translocation through graphene nanopores.," *Nano Lett.*, vol. 13, no. 5, pp. 1969–76, May 2013.
8. K. K. Saha, M. Drndić, and B. K. Nikolić, "DNA base-specific modulation of microampere transverse edge currents through a metallic graphene nanoribbon with a nanopore.," *Nano Lett.*, vol. 12, no. 1, pp. 50–5, Jan. 2012.
9. D. B. Wells, M. Belkin, J. Comer, and A. Aksimentiev, "Assessing graphene nanopores for sequencing DNA.," *Nano Lett.*, vol. 12, no. 8, pp. 4117–23, Aug. 2012.
10. J. Prasongkit, A. Grigoriev, B. Pathak, R. Ahuja, and R. H. Scheicher, "Transverse conductance of DNA nucleotides in a graphene nanogap from first principles.," *Nano Lett.*, vol. 11, no. 5, pp. 1941–5, May 2011.
11. A. Girdhar, C. Sathe, K. Schulten, and J.-P. Leburton, "Graphene quantum point contact transistor for DNA sensing.," *Proc. Natl. Acad. Sci. U. S. A.*, vol. 110, no. 42, pp. 16748–53, Oct. 2013.
12. W. Qiu and E. Skafidas, "Graphene nanopore field effect transistors," *J. Appl. Phys.*, vol. 116, no. 2, p. 023709, Jul. 2014.
13. I. Bezrukov, S.M. Vodyannoy, "Noise in Biological Membranes and Relevant Ionic Systems - Biomembrane Electrochemistry - Advances in Chemistry (ACS Publications)," *Biomembr. Electrochem.*, pp. 375–399, 1994.
14. F. Wohnsland and R. Benz, "1/ f -Noise of Open Bacterial Porin Channels," *J.*

Membr. Biol., vol. 158, no. 1, pp. 77–85, Jul. 1997.

15. R. M. M. Smeets, U. F. Keyser, N. H. Dekker, and C. Dekker, “Noise in solid-state nanopores,” *Proc. Natl. Acad. Sci. U. S. A.*, vol. 105, no. 2, pp. 417–21, Jan. 2008.
16. R. M. M. Smeets, N. H. Dekker, and C. Dekker, “Low-frequency noise in solid-state nanopores,” *Nanotechnology*, vol. 20, no. 9, p. 095501, Mar. 2009.
17. D. P. Hoogerheide, S. Garaj, and J. A. Golovchenko, “Probing Surface Charge Fluctuations with Solid-State Nanopores,” *Phys. Rev. Lett.*, vol. 102, no. 25, p. 256804, Jun. 2009.
18. M. R. Powell, I. Vlassiouk, C. Martens, and Z. S. Siwy, “Nonequilibrium  $1/f$  noise in rectifying nanopores,” *Phys. Rev. Lett.*, vol. 103, no. 24, p. 248104, Dec. 2009.
19. M. R. Powell, N. Sa, M. Davenport, K. Healy, I. Vlassiouk, S. E. Létant, L. A. Baker, and Z. S. Siwy, “Noise Properties of Rectifying Nanopores,” *J. Phys. Chem. C*, vol. 115, no. 17, pp. 8775–8783, May 2011.
20. A. Kumar, K.-B. Park, H.-M. Kim, and K.-B. Kim, “Noise and its reduction in graphene based nanopore devices,” *Nanotechnology*, vol. 24, no. 49, p. 495503, Dec. 2013.
21. J. K. Rosenstein, M. Wanunu, C. A. Merchant, M. Drndic, and K. L. Shepard, “Integrated nanopore sensing platform with sub-microsecond temporal resolution,” *Nat. Methods*, vol. 9, no. 5, pp. 487–92, May 2012.
22. P. Chen, T. Mitsui, D. B. Farmer, J. Golovchenko, R. G. Gordon, and D. Branton, “Atomic Layer Deposition to Fine-Tune the Surface Properties and Diameters of Fabricated Nanopores,” *Nano Lett.*, vol. 4, no. 7, pp. 1333–1337, Jun. 2004.
23. J. Johnson, “The Schottky Effect in Low Frequency Circuits,” *Phys. Rev.*, vol. 26, no. 1, pp. 71–85, Jul. 1925.
24. F. N. Hooge, “ $1/f$  noise sources,” *IEEE Trans. Electron Devices*, vol. 41, no. 11, pp. 1926–1935, 1994.
25. A. A. Balandin, “Low-frequency  $1/f$  noise in graphene devices,” *Nat. Nanotechnol.*, vol. 8, no. 8, pp. 549–55, Aug. 2013.
26. F. N. Hooge, “ $1/f$  noise is no surface effect,” *Phys. Lett. A*, vol. 29, no. 3, pp. 139–140, Apr. 1969.
27. F. N. Hooge, “noise in the conductance of ions in aqueous solutions,” *Phys. Lett. A*, vol. 33, no. 3, pp. 169–170, Oct. 1970.
28. S. W. Kowalczyk, A. Y. Grosberg, Y. Rabin, and C. Dekker, “Modeling the conductance and DNA blockade of solid-state nanopores,” *Nanotechnology*, vol. 22, no. 31, p. 315101, Aug. 2011.
29. J. E. Hall, “Access resistance of a small circular pore,” *J. Gen. Physiol.*, vol. 66, no. 4, pp. 531–532, Oct. 1975.
30. C. Lee, X. Wei, J. W. Kysar, and J. Hone, “Measurement of the elastic properties and intrinsic strength of monolayer graphene,” *Science*, vol. 321, no. 5887, pp.

- 385–8, Jul. 2008.
31. A. Castellanos-Gomez, R. van Leeuwen, M. Buscema, H. S. J. van der Zant, G. a Steele, and W. J. Venstra, "Single-layer MoS(2) mechanical resonators," *Adv. Mater.*, vol. 25, no. 46, pp. 6719–23, Dec. 2013.
  32. C. Sathe, X. Zou, J.-P. Leburton, and K. Schulten, "Computational investigation of DNA detection using graphene nanopores.," *ACS Nano*, vol. 5, no. 11, pp. 8842–51, Dec. 2011.
  33. C. A. Merchant, K. Healy, M. Wanunu, V. Ray, N. Peterman, J. Bartel, M. D. Fischbein, K. Venta, Z. Luo, A. T. C. Johnson, and M. Drndić, "DNA translocation through graphene nanopores.," *Nano Lett.*, vol. 10, no. 8, pp. 2915–21, Aug. 2010.
  34. B. M. Venkatesan, D. Estrada, S. Banerjee, X. Jin, V. E. Dorgan, M.-H. Bae, N. R. Aluru, E. Pop, and R. Bashir, "Stacked graphene-Al<sub>2</sub>O<sub>3</sub> nanopore sensors for sensitive detection of DNA and DNA-protein complexes.," *ACS Nano*, vol. 6, no. 1, pp. 441–50, Jan. 2012.
  35. S. Garaj, S. Liu, J. A. Golovchenko, and D. Branton, "Molecule-hugging graphene nanopores.," *Proc. Natl. Acad. Sci. U. S. A.*, vol. 110, no. 30, pp. 12192–6, Jul. 2013.
  36. G. F. Schneider, V. E. Calado, H. Zandbergen, L. M. K. Vandersypen, and C. Dekker, "Wedging transfer of nanostructures.," *Nano Lett.*, vol. 10, no. 5, pp. 1912–6, May 2010.
  37. B. Song, G. F. Schneider, Q. Xu, G. Pandraud, C. Dekker, and H. Zandbergen, "Atomic-scale electron-beam sculpting of near-defect-free graphene nanostructures.," *Nano Lett.*, vol. 11, no. 6, pp. 2247–50, Jul. 2011.
  38. X. J. A. Janssen, M. P. Jonsson, C. Plesa, G. V. Soni, C. Dekker, and N. H. Dekker, "Rapid manufacturing of low-noise membranes for nanopore sensors by trans-chip illumination lithography.," *Nanotechnology*, vol. 23, no. 47, p. 475302, Dec. 2012.



# 5

## THROUGH-MEMBRANE ELECTRON-BEAM LITHOGRAPHY FOR ULTRATHIN MEMBRANE APPLICATIONS

We present a technique to fabricate ultrathin (down to 20 nm) uniform electron transparent windows at dedicated locations in SiN membranes for *in situ* transmission electron microscopy (TEM) experiments. Electron-beam (e-beam) resist is spray-coated on the back side of the membrane in a KOH-etched cavity in silicon, and subsequently patterned using through-membrane electron-beam lithography (EBL). This is a controlled way to make transparent windows in membranes, whilst the top sides of the membranes remain undamaged and retain their flatness. The approach was optimized for MEMS-based heating chips, but can be applied to any chip design. We show two different applications of this technique for (1) fabrication of a nanogap electrode by means of electromigration in a thin freestanding metal film and (2) making low-noise graphene nanopore devices.

---

This chapter has been published as: M. Neklyudova, A.K. Erdamar, L. Vicarelli, S. J. Heerema, T. Rehfeldt, G. Pandraud, Z. Kolahdouz, C. Dekker and H. W. Zandbergen, *Appl. Phys. Lett.* 111, (2017)

## 5.1 INTRODUCTION

5 | For *in situ* TEM heating and biasing experiments, chips with less than 20 nm-thick amorphous membranes are needed in order to obtain a good electron transparency<sup>1,2</sup>. Once the freestanding area of the membrane needs to be larger than several microns, or when the membrane design is more complex (*i.e.* includes metal electrodes), it becomes very difficult to maintain the membranes intact. One way to obtain thin windows in membranes, is to pattern a mask (such as a resist layer) on the top side of the SiN and etch the material down to the silicon, followed by deposition of a thin layer of SiN using LPCVD. This approach has one big disadvantage: the thin windows are formed at the bottom of the thick SiN membrane (see Fig. 5.5 in the supplementary section), meaning that the SiN window top side is located in a deep cavity compared to the top surface of the membrane. Such deep cavity-shaped membrane windows are inconvenient for various measurements, such as liquid *in situ* TEM experiments. Also, additional deposition of electrical contacts for biasing *in situ* TEM experiments on these recessed surfaces is impossible. To address such issues, we have developed a technique where the SiN is locally removed from the back side, such that the top side of the membrane remains undamaged.

Performing EBL from the back side of the membrane is not trivial with conventional lithography systems since it stands at the bottom of a 300-500  $\mu\text{m}$ -deep KOH-etched cavity. The resist mask should cover the surface that is to be patterned, with the distance of less than 100  $\mu\text{m}$  to the lens of the EBL machine to avoid defocusing issues. In the method that is described here, e-beam resist is spray coated on the back side of the SiN membrane, and exposed with an e-beam from the top side, through the membrane and the structures on top of it. In this way, the defocus problem is solved, since the lens will be in close enough proximity to the resist layer. After explanation of the full procedure, we present two examples of applications of this approach.

Fabrication of the MEMS-based heaters consists of several steps. First, we start with 300-500  $\mu\text{m}$  thick Si wafers and deposit 200 nm-thick SiN by low pressure chemical vapor deposition (LPCVD) technique as an isolation layer between the metal and Si substrate. Heater coils are made of tantalum (Ta)/platinum (Pt) metal layers with 20/180 nm thicknesses, respectively, deposited by e-beam evaporation and etched by ion etching. After the second deposition of 200 nm-thick LPCVD SiN, the heater is embedded in a 400-600 nm-thick SiN. The freestanding SiN membranes are obtained by KOH-etching of the silicon.

Next, e-beam resist (PMMA:PGMEA:MEK) is sprayed in multiple steps on the back side of the chips with an EVG101 spray-coater. The main challenge of this method is to obtain uniform resist coverage on the back side of SiN membranes due to the topography of 300-500  $\mu\text{m}$ -deep KOH-etched cavity (shown schematically in figure 5.1a). The optimized recipe results in a 12  $\mu\text{m}$ -thick PMMA resist layer. The resist is exposed from the top side of the

chip by 100 kV electrons penetrating through the 400-600 nm-thick SiN membrane with a Leica 5000+ EBL machine. After resist development the membrane is etched by reactive ion etching (RIE) in Ar/CHF<sub>3</sub>-based plasma with anisotropic etching. The etching rate and time are critical to obtain the required thickness of the SiN in RIE. Here a Leybold RIE machine was used, with a power of 50W (Ar:CHF<sub>3</sub> 25:25 sccm), to obtain an etch rate of 18 nm/min. The membrane thickness is monitored using optical microscopy, where the SiN thickness is estimated based on comparison of SiN color with LPCVD SiN color chart. After etching, the resist is removed by PRS3000 (positive resist stripper) and O<sub>2</sub>-plasma. Depending on the application of this technique, additional fabrication steps might be required.

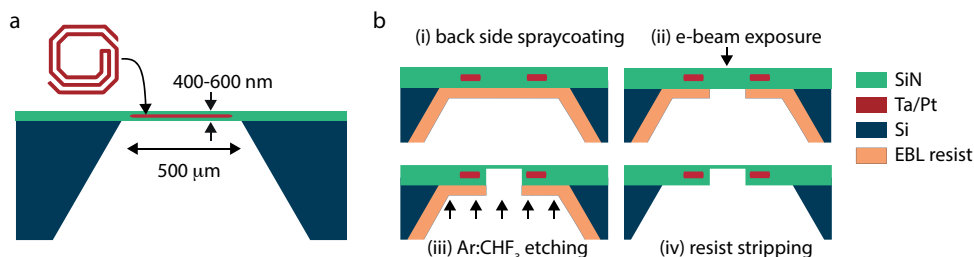


**Figure 5.1 Schematics of the heater chip and the lithography procedure.** (a) A freestanding silicon nitride membrane with a thickness of 400-600nm spans 500x500μm, supported by a silicon chip. The platinum heater coil is embedded in the SiN membrane (b) (i) Spray-coating of e-beam resist on the back side of the chip (ii) through-membrane e-beam exposure and development (iii) Ar:CHF<sub>3</sub> plasma etching of SiN from the back, up to required thickness, (iv) removal of the resist.

The first example of an application of through-membrane lithography technique is for in situ TEM biasing experiments, in particular, the fabrication of a nanogap electrode in gold (Au) nanobridges by electromigration.

## 5.2 ELECTRON MIGRATION IN THIN SiN WINDOWS

Electrodes that are separated by a nanogap of only a few nanometers (1-10 nm) are called nanogap electrodes. They are used to characterize material properties at the nanometer scale, and form building blocks in molecular-scale devices and circuits<sup>3</sup>. Nanogap electrodes can be fabricated by different methods such as mechanical break junctions<sup>4</sup>, EBL<sup>5</sup>, feedback controlled electromigration (FCE)<sup>6</sup>, shadow mask evaporation<sup>7</sup>, etc. All these methods show promising results and provide a desired configuration of the electrodes. Here, we present the fabrication of nanogap electrodes in a gold nanobridge by the FCE technique, while this is monitored *in situ* with TEM. *In situ* TEM enables the direct observation of nanogap formation in real-time and the possibility to control of the final size of the nanogap<sup>8</sup>. First, through-membrane EBL is used to pattern thin windows in the silicon nitride windows of the heater chips. The thin membranes facilitate the visualization of the nanobridge formation, with the subsequent shaping into a nanogap electrodes, which



is required for the characterization of trapped nano particles. A thick SiN support would induce a noisy background, impeding TEM visualization of the specimen behavior under an applied stimulus. The interest to fabricate these nanogap electrodes on top of the heater chips is to perform TEM characterization of nanomaterials (low-dimensional nanocrystals, phase change nanoparticles, individual molecules, etc.), while simultaneously applying a bias voltage and local heating. For this experiment, heating up to 120-140°C prevented e-beam-induced carbon contamination during *in situ* visualization of the nanogap formation.

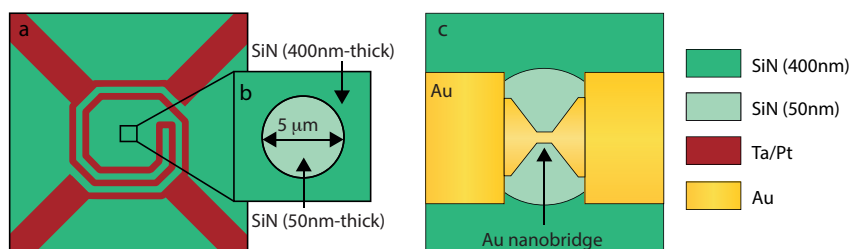


**Figure 5.2** (a) Schematic illustration of MEMS-based heater with a flat 400 nm-thick SiN center. (b) Central part of the heating coil showing a 50 nm-thick SiN window with a diameter of 5 μm. (c) The configuration of fabricated device onto 50 nm-thick SiN window containing 20 nm-thick Au nanobridge and 200 nm-thick Au contact pads.

A schematic illustration of MEMS-based heater with a flat 400 nm-thick SiN center is shown in figure 5.2a. Through-membrane EBL followed by RIE was applied to obtain 50 nm-thick SiN circular windows with a 5 μm diameter, in the center of Pt heating coil (Fig. 5.2b). Au bridges with a length of 700 nm, width of 250 nm and thickness of 20 nm were made on top of the 50 nm-thick SiN area using EBL followed by e-beam evaporation of gold. Contact pads to the nanobridge were patterned in a second step of EBL followed by metal evaporation, where of a 250 nm-thick layer of Au on a 5 nm-thick adhesion layer of Cr was deposited. The configuration of a device is schematically presented in figure 5.2c. To further reduce the thickness of SiN at the location of Au nanobridge, SiN was etched from the back side of MEMS-based heater using RIE with  $\text{CHF}_3/\text{O}_2$  gases with a flow ratio of 50 sscm and 2.5 sscm, respectively. The MEMS-based heater with Au nanobridge was placed into home-built TEM holder containing six contacts, which enables the combination of heating experiments and electrical measurements. Four contacts are used for heating. Electrical measurements are done by applying a voltage to the remaining two contacts. The heater spiral was calibrated with a pyrometer before the experiment.

The FCE process in Au nanobridges was studied *in situ* with TEM using a FEI Titan microscope operating at 300 keV. In FCE mode, the bridge conductance was constantly monitored while the voltage was ramped up. If there was a sudden decrease in conductance,

the voltage was reduced to a lower value. The process was restarted after a new reference conductance was defined. The program stopped when a predefined conductance value was reached. To avoid e-beam-induced carbon contamination, which can result in spurious conductance, the electromigration experiments were performed at 120°C temperature.

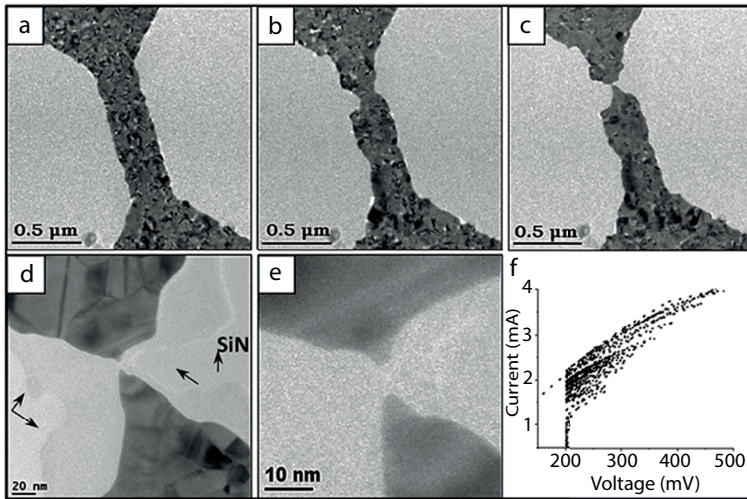


**Figure 5.3. Snapshots taken from an in situ TEM movie recorded during FCE process in Au nanobridge.** (a) The original bridge. (b)-(c) TEM images showing the formation of nanogap in the Au bridge during FCE. (d) TEM image acquired after nanogap formation; arrows indicate the areas with a thin SiN layer. (e) Enlarged area of (d) showing Au electrodes separated with 5.26 nm nanogap. (f) I-V curve of the FCE process.

Figure 5.3 shows snapshots of a typical *in situ* TEM movie recorded during the nanogap formation in the FCE process. The initial configuration of the bridge is shown in figure 5.3a. When the current was passed through the bridge, we observed grain growth prior to electromigration. The grain growth occurred due to the temperature rise in the bridge caused by current-induced Joule-heating. In figure 5.3b, the bridge started to thin close to the cathode side forming a constriction. When the electromigration was observed, the current density was about  $7 \times 10^7$  A/cm<sup>2</sup>. In the last stage of the electromigration a narrow constriction was formed as shown in figure 5.3c and the constriction was further narrowed at low voltage values (around 200 mV). Finally, a nanogap electrode was produced (see Fig. 5.3d). The size of the just formed nanogap, which was about 2-3 nm, increased to 5-6 nm during continuous illumination by the e-beam within several seconds. Figure 5.3e presents a TEM image acquired at higher magnification of the final configuration of the nanogap with the size of 5.26 nm, which did not change for at least several minutes of e-beam irradiation. At the moment when the nanogap electrode was initially formed, the tips of the electrodes were sharp. However, after several seconds, when the gap size increased, the shape of the electrode tips became more smooth, which is likely due to surface tension of the gold. This

observation is in agreement with the previous reports of Zandbergen et al.<sup>9</sup> on continued relaxation of gold nanogaps formed by e-beam bombardment even after the intense irradiation is completed, also with the report of Strachan et al.<sup>10</sup> on the evolution of Au nanogap electrodes. A typical I–V curve of FCE process in Au nanobridges is shown in figure 5.3f.

In figure 5.3d, one can see a thin layer of SiN around the nanogap. Comparing to standard fabrication methods of nanogaps on top of SiN membranes with the thicknesses of 100 nm<sup>11</sup>, this technique allows to fabricate nanogap electrodes with a thin SiN layer beneath it. In order to remove the SiN completely, we applied a vaporized HF by SPTS etch vapor system, using a 190 sccm HF flow that enabled to etch remained 2-3 nm SiN completely without damaging the metal lines (see Fig. 5.6 in the supplementary section). After applying the HF treatment we observed no SiN near the metal structures.

### 5.3 LOW-NOISE GRAPHENE NANOPORE DEVICES

Graphene nanopores represent a promising tool for fast and direct sequencing of DNA molecules<sup>12</sup>. In nanopore sensing, a tiny hole ('nanopore') in a membrane that separates two compartments of electrolyte solution is the only pathway for ions and molecules to pass. When a voltage is applied over the membrane, an ionic current is induced with a resistance that is set by the pore length and width, and negatively charged DNA molecules will move towards the positive pole. When a DNA molecule traverses through the nanopore, it impedes the ionic current, which leads to a resistive spike in the ionic current baseline (in the order of ~1 nA). The two great advantages of graphene nanopores, to the more commonly used SiN solid-state nanopores, are that the graphene is atomically thin, which optimizes the sensing resolution as the pore hosts a minimum number of bases at the same time, and its conductive nature facilitates new modes of base detection.

One downside of these graphene nanopore systems is that the noise levels in the ionic current are relatively high (about two orders of magnitude higher than in SiN pores<sup>13</sup>). The noise in the graphene nanopore ionic current is characterized by a 1/f dependence (Fig. 5.4c, blue curve). It has been shown that increasing the number of graphene layers<sup>13</sup>, the use of additional layers of other materials<sup>14,15</sup> or reducing the area of freestanding graphene can lower the noise levels in the graphene nanopore currents<sup>16</sup>. Reducing the area of freestanding graphene (diameter~100 nm) provides the most elegant approach to the noise reduction as the atomically thin membrane is retained.

As in the heater chip layout described above, a Pt heater is embedded in the supporting SiN membrane, which is used to heat up the graphene during STEM sculpting of the graphene nanopore<sup>17,18</sup>, leading to a total membrane thickness of 400-600 nm (Fig. 5.4a). The formation of a narrow (d~100 nm) access channel in such a 'thick' membrane would add a

large channel resistance to the circuit. This is an unwanted effect, as in the ideal case the graphene nanopore exclusively sets the resistance and thus behaves as the sensing probe. To reduce the area of freestanding graphene diameter to  $\sim 100$  nm, while preventing the addition of a huge channel resistance, the fabrication of a thin window in the SiN membrane is needed. Using the through-membrane EBL technique and RIE that is described in this chapter,  $5 \times 5 \mu\text{m}^2$  windows of  $\sim 50$ - $150$  nm thickness were fabricated, after which pores with diameters of  $\sim 50$ - $150$  nm in diameter were made using focused ion beam drilling. Graphene flakes were subsequently transferred onto these chips<sup>19</sup>, and finally  $\sim 10$  nm pores were sculpted in the graphene using high-temperature sculpting with STEM<sup>17,18</sup>.

We measured and analyzed ionic current baselines of 24 thin window devices with reduced areas of freestanding graphene ( $\sim 50$ - $150$  nm in diameter) and compared their noise levels to those of 45 devices with  $600$  nm-thick windows containing  $\sim 1 \mu\text{m}$  diameter freestanding graphene. All traces were recorded at  $100$  mV at a KCl or LiCl salt concentration of  $1$  M. Two representative current baselines are plotted in figure 5.4b. These clearly show that the blue curve originating from a device with a large area of freestanding graphene ( $d \sim 1 \mu\text{m}$ ) is fluctuating more than the red curve belonging to a reduced area of freestanding graphene ( $d \sim 100$  nm). This occurs at all bandwidths, but the difference is much more pronounced for a lower bandwidth (cf. the traces in light blue and grey in figure 5.4b). The current power spectral densities that correspond to the traces from figure 5.4b are compared in figure 5.4c. The two types of devices clearly expose different power spectral density curves. The noise from the device with large area of freestanding graphene ( $d \sim 1 \mu\text{m}$ ) (blue) is characterized by a  $1/f$  dependence up to the filter cut-off frequency of  $10$  kHz, whereas for the back side etched samples, the  $1/f$  dependence only holds up to a few hundred Hz. To determine the low-frequency noise coefficient ( $C_{\text{LF}}$ ) per device, representing the  $1/f$  noise level, the power spectral density functions were normalized by the squares of their mean currents and linear fits to the curves between  $1$ - $200$  Hz were applied on logarithmic scales (see ref. 12 for more details on the analysis). The results for  $C_{\text{LF}}$  are plotted in figure 5.4d, we find that the  $1/f$  noise levels in thin window devices are on average reduced by one order of magnitude ( $C_{\text{LF}(d \sim 100 \text{nm})} \sim 5 \times 10^{-7}$  versus  $C_{\text{LF}(d \sim 1 \mu\text{m})} \sim 6 \times 10^{-6}$ ).

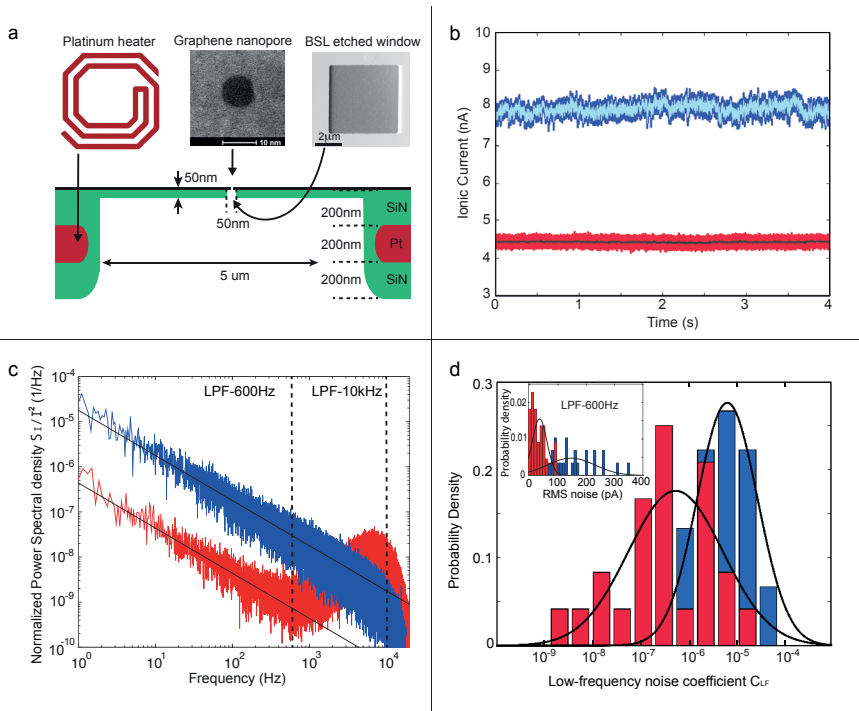


**Figure 5.4. Graphene nanopores fabricated on thin SiN windows with smaller SiN pore sizes exhibit lower noise due to a reduced area of freestanding graphene.** (a) Scheme of a graphene nanopore device with a  $5 \times 5 \mu\text{m}^2$  and 50 nm-thick window, etched from the back side of a 600 nm-thick SiN membrane. (b) Ionic current baselines of a device with a large area of freestanding graphene ( $\sim 1 \mu\text{m}$  in diameter) on a 600 nm SiN membrane (blue) and of a device with a back side etched window (as in Fig. 5.3a) with a small area of freestanding graphene ( $\sim 100 \text{ nm}$  in diameter) (red). (c) Normalized power spectral density curves of the ionic current baselines from figure 5.3b. The  $1/f$  noise level is determined by linear fitting of the logarithmic values between 1-200 Hz (black curves). (d) Probability distributions of the  $1/f$  noise coefficients CLF of the two different device layouts, the  $1/f$  noise levels in thin window devices are on average reduced by one order of magnitude. Inset: RMS noise levels at a filter frequency of 600 Hz, where the thin window devices with reduced area of freestanding graphene (red) expose a factor of  $\sim 4$  lower RMS noise.

Secondly, we quantified the  $I_{\text{rms}}$  levels (representing the deviations from the mean of the current) of 24 thin window devices with reduced freestanding graphene areas (red) and compared those to 29 ‘thick’ membrane samples with larger freestanding graphene area (blue). As can be read from the power spectral density curves in figure 5.4c, the noise is particularly reduced in the low-frequency regime ( $< 600 \text{ Hz}$ ), which is observed by the comparison of the light blue and dark grey traces in figure 5.4b that were low-pass filtered at 600 Hz. The  $I_{\text{rms}}$  values at a bandwidth of 600 Hz for both device types are represented in the histogram in the inset in figure 5.4d, showing that the  $I_{\text{rms}}$  noise is reduced by a factor of  $\sim 4$  (from  $146 \pm 16 \text{ pA}$  to  $35 \pm 5 \text{ pA}$ ). At 10 kHz, the  $I_{\text{rms}}$  noise is reduced by a factor of  $\sim 2.7$  ( $162 \pm 16 \text{ pA}$  to  $59 \pm 4$ ).

The noise reduction that we have shown here is relevant for DNA sensing with graphene nanopores as it enables to improve the signal-to-noise, although other challenges need to be overcome as well. Various research groups are currently exploring alternative detection methods that use the conductive nature of the graphene<sup>12</sup>. In these setups, a good signal-to-noise ratio is also important as the nanopore principle is still used, both to drive the DNA molecule along the sensor and to confirm its passage.

With the use of back side spray coating and through-membrane e-beam exposure, it was possible to fabricate thin electron transparent SiN windows in a membrane, while the flatness of the top side of the membrane was maintained. In nanogap formation, we have demonstrated that this unique fabrication technique enables to obtain a very thin SiN layer. The application of additional etching steps (with vaporized HF) allows to remove the membrane completely for further applications of nanogap electrodes. In the second application, the thin windows are used to fabricate low-noise nanopores in graphene to improve the signal-to-noise levels in DNA sensing experiments. This development is beneficial for further graphene nanopore measurements and for graphene-based DNA sequencing. In addition to these demonstrated applications, having an ultrathin SiN electron transparent window on the top of the membrane will have advantages on *in situ* TEM liquid cell, nanoreactor and battery studies since it offers a flat surface on the top that enables smooth liquid flow for liquid cell studies and controllable lift off materials after deposition.

#### 5.4 SUPPLEMENTARY INFORMATION

Figure 5.5 presents a schematic illustration of the chip for *in situ* TEM heating experiments. Figure 5.6 shows a metallic structure with a thin SiN layer after plasma etching, which is removed after vaporized HF treatment.

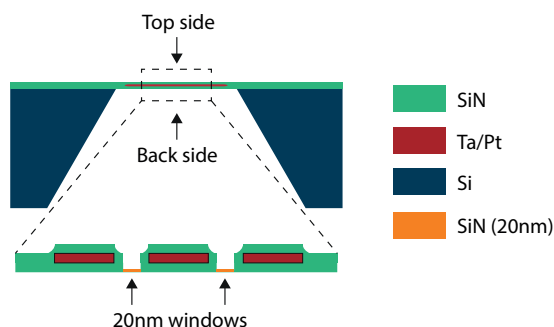


**Figure 5.5** (a) A schematic illustration of a chip for *in situ* TEM heating experiments, where thin windows are etched from the top side. Below a magnified area of a SiN membrane showing the thick (in total 420 nm) and thin (20 nm) SiN membrane areas, where the SiN is etched from the top of the membrane.

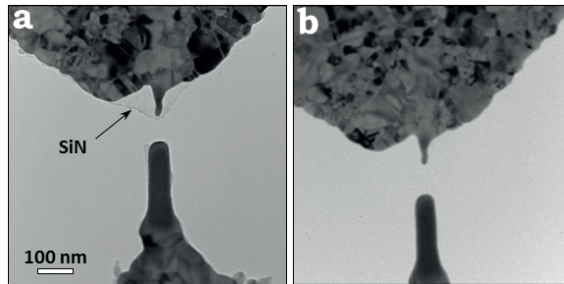


**Figure 5.6** (a) Thin layer of SiN is present after plasma etching. (b) After SiN etching with vaporized HF, the SiN is completely removed.

REFERENCES

1. Van Huis, M. A. *et al.* Atomic imaging of phase transitions and morphology transformations in nanocrystals. *Adv. Mater.* **21**, 4992–4995 (2009).
2. Neklyudova, M., Sabater, C., Erdamar, A. K., Van Ruitenbeek, J. M. & Zandbergen, H. W. In situ transmission electron microscope formation of a single-crystalline Bi film on an amorphous substrate. *Appl. Phys. Lett.* **110**, (2017).
3. Li, T., Hu, W. & Zhu, D. Nanogap Electrodes. *Adv. Mater.* **22**, 286–300 (2010).
4. Reed, M. A., Zhou, C., Muller, C. J., Burgin, T. P. & Tour, J. M. Conductance of a molecular junction. *Science (80-. )*. **278**, 252–254 (1997).
5. Chen, W., Ahmed, H. & Nakazoto, K. Coulomb blockade at 77 K in nanoscale metallic islands in a lateral nanostructure. *Appl. Phys. Lett.* **66**, 3383 (1995).
6. Park, J. *et al.* Coulomb blockade and the kondo effect in single-atom transistors. *Nature* **417**, 722–725 (2002).
7. Kubatkin, S. *et al.* Single-electron transistor of a single organic molecule with access to several redox states. *Nature* **425**, 698–701 (2003).
8. Rudneva, M. *et al.* In situ transmission electron microscopy imaging of electromigration in platinum nanowires. *Microsc. Microanal.* **19**, 43–48 (2013).
9. Zandbergen, H. W. *et al.* Sculpting nanoelectrodes with a transmission electron beam for electrical and geometrical characterization of nanoparticles. *Nano Lett.* **5**, 549–553 (2005).
10. Strachan, D. R. *et al.* Clean electromigrated nanogaps imaged by transmission electron microscopy. *Nano Lett.* **6**, 441–444 (2006).
11. Neklyudova, M. *PhD thesis*. Casimir PhD-series 2016-14, 2016.
12. Heerema, S. J. & Dekker, C. Graphene nanodevices for DNA sequencing. *Nat. Nanotechnol.* **11**, 127–136 (2016).
13. Heerema, S. J. *et al.* 1/f noise in graphene nanopores. *Nanotechnology* **26**, 74001 (2015).
14. Merchant, C. A. *et al.* DNA translocation through graphene nanopores. *Nano Lett.* **10**, 2915–21 (2010).
15. Venkatesan, B. M. *et al.* Stacked graphene-Al<sub>2</sub>O<sub>3</sub> nanopore sensors for sensitive detection of DNA and DNA-protein complexes. *ACS Nano* **6**, 441–50 (2012).
16. Garaj, S., Liu, S., Golovchenko, J. A. & Branton, D. Molecule-hugging graphene nanopores. *Proc. Natl. Acad. Sci. U. S. A.* **110**, 12192–6 (2013).
17. Song, B. *et al.* Atomic-scale electron-beam sculpting of near-defect-free graphene nanostructures. *Nano Lett.* **11**, 2247–50 (2011).
18. Xu, Q. *et al.* Controllable atomic scale patterning of freestanding monolayer graphene at elevated temperature. *ACS Nano* **7**, 1566–72 (2013).
19. Schneider, G. F., Calado, V. E., Zandbergen, H., Vandersypen, L. M. K. & Dekker, C. Wedging transfer of nanostructures. *Nano Lett.* **10**, 1912–6 (2010).





# 6

## PROBING DNA TRANSLOCATIONS WITH INPLANE CURRENT SIGNALS IN A GRAPHENE NANORIBBON WITH A NANOPORE

Many theoretical studies predict that DNA sequencing should be feasible by monitoring the transverse current through a graphene nanoribbon while a DNA molecule translocates through a nanopore in that ribbon. Such a readout would benefit from the special transport properties of graphene, provide ultimate spatial resolution because of the single-atom layer thickness of graphene, and facilitate high-bandwidth measurements. Previous experimental attempts to measure such transverse inplane signals were however dominated by a trivial capacitive response. Here, we explore the feasibility of the approach using a custom-made differential current amplifier that discriminates between the capacitive current signal and the resistive response in the graphene. We fabricate well-defined short and narrow (30nmx30nm) nanoribbons with a 5nm nanopore in graphene with a high-temperature scanning transmission electron microscope to retain the crystallinity and sensitivity of the graphene. We show that, indeed, resistive modulations can be observed in the graphene current due to DNA translocation through the nanopore, thus demonstrating that DNA sensing with inplane currents in graphene nanostructures is possible. The approach is however exceedingly challenging due to low yields in device fabrication connected to the complex multistep device layout.

---

This chapter has been published as: S.J. Heerema, L. Vicarelli., S. Pud, R.N. Schouten, H.W. Zandbergen, C. Dekker. ACS Nano DOI 10.1021/acs.nano.7b08635, February 23, 2018.

## 6.1 INTRODUCTION

Nanopores have proven to be powerful biomolecular sensors as they allow detection and characterization of even single molecules solely *via* an electronic readout with no need for amplification or labels. In nanopore sensing, the molecule of interest is pulled by an electric field through a nanometer-sized hole in a thin membrane in a head-to-tail fashion while structural features of the molecule can be consecutively read<sup>1</sup>. The traversal of a DNA molecule leads to a blockade in the ionic current through the nanopore that is monitored, *i.e.* what is commonly measured as the sensing signal. DNA sequencing using biological nanopores within a lipid membrane has successfully been shown<sup>2</sup> and recently even commercialized<sup>3,4</sup>.

6 | Solid-state nanopores<sup>5</sup> present some advantages over biological pores, such as their robustness, thermal, mechanical and chemical versatility, and potential for device integration in wafer-scale integrated circuits<sup>6</sup>. Whereas solid-state nanopores have enabled numerous interesting biophysics studies of proteins and nucleic acids<sup>7,8</sup>, calling individual bases along a DNA molecule traversing through such a nanopore – a prerequisite for sequencing – remains to be shown yet. Conventional solid-state nanopores suffer from poor spatial resolution, as the length of these nanopores is set by the thickness of the membranes used, typically 10-30nm, resulting in an ionic current blockade that is constituted by ~100 bases that collectively reside in the pore. For that reason, the use of a two-dimensional membrane material, such as graphene, is clearly appealing, as only one or a few bases can occupy the pore volume at the same time. Various attempts have been reported on the use of graphene and related layered materials to probe DNA, with partial success<sup>9-20</sup>. Individual DNA molecules could well be distinguished but challenges remain. For example, detailed features were hard to resolve because the ionic currents through these nanopores exhibited high levels of 1/f-noise<sup>21</sup>. Furthermore, the fast translocation speed of the DNA molecules (0.01-1  $\mu$ s/base) sets a need for >MHz sampling rates, at which the noise is too high to resolve the blockade signals, let alone sequence information.

Since graphene is a conducting material<sup>22</sup>, an interesting alternative to the ionic-current readout is the measurement of the transverse (*i.e.* perpendicular to the DNA molecule) current through a graphene nanoribbon with a nanopore through that ribbon, see Fig. 6.1a. Many theoretical and computational studies on transport in graphene nanoribbons (GNRs) and graphene quantum point contacts with a nanopore have shown that the presence of the DNA bases inside the nanopore can lead to base-specific modulations in the electronic current through the graphene nanostructure, thus in principle enabling measurement of the DNA sequence as the molecule passes through the nanopore<sup>23-34</sup>. These studies show that non-electrostatic base-specific interactions between the DNA bases and the graphene nanoribbon result in alterations of the local density of states around the nanopore leading

to resistive changes of the nanoribbon that can be measured in the inplane current running through the ribbon. An important advantage of this approach is the relatively large current magnitude in these nanoribbons (A), and the flat frequency response to high megahertz frequencies<sup>35,36</sup>, facilitating high-bandwidth measurements, *i.e.*, opening up the possibility to sequence at the translocation speed that is typically observed with solid-state nanopores.

A simplified schematic of the proposed experiment is presented in the Fig. 6.1b. The traversal of DNA through a nanopore in a graphene nanoribbon is monitored by the inplane current measurement. The voltage that is applied to the ionic current electrodes to drive DNA through the nanopore simultaneously acts as an electrolytic gate that modulates the current through the graphene nanoribbon. The graphene current dependence on the gate voltage, the so-called Dirac curve (Fig. 6.1c), yields the transconductance  $g_m$  that indicates the sensitivity of the graphene conductance to external voltage fluctuations.

Similar approaches have been reported before with wider graphene nanoribbons<sup>37,38</sup> and silicon nanowires<sup>39</sup> for DNA detection. Importantly, the current signals measured with these systems were shown to originate in a capacitive coupling of the potential change at the nanopore that occurs during DNA translocation to the local capacitance of the sensor at the nanopore<sup>39</sup>. These capacitive signals were studied in detail, and were shown to increase with smaller pore diameters and thinner membranes and can be maximized through the introduction of a buffer salt gradient<sup>37-41</sup>. Importantly, while this capacitive signal reveals the local presence of DNA in the nanopore, it does not represent the theoretically predicted resistive modulation in the graphene current discussed above. In this study, we aim to elucidate whether or not it is feasible to measure a non-capacitive response of DNA translocations in the transverse current through a graphene nanoribbon.

What signals can be expected in the graphene transverse current due to the presence of DNA in the nanopore? We distinguish between three different types of signals, which are schematically shown in Fig. 6.1d, e, and f. Firstly, as mentioned above, we expect to measure a capacitive signal (Fig. 6.1d), which is expected to be similar irrespective of the choice of the DC operating point on the Dirac curve (indicated by \* and • in Fig. 6.1c), and its magnitude should be independent of the bias voltage applied to the graphene<sup>38</sup>. This signal can be defined as  $I_c = C_g \times \frac{\Delta V_l}{\Delta t}$ , with  $\Delta V_l$  the local potential change at the nanopore due to DNA translocation,  $\Delta t$  the time scale over which this change is realized, and  $C_g$  the capacitance of the graphene to the electrolyte at the nanopore. Second, we expect that electrostatic interactions will modify the Fermi level of the graphene nanostructure (Fig. 6.1e).

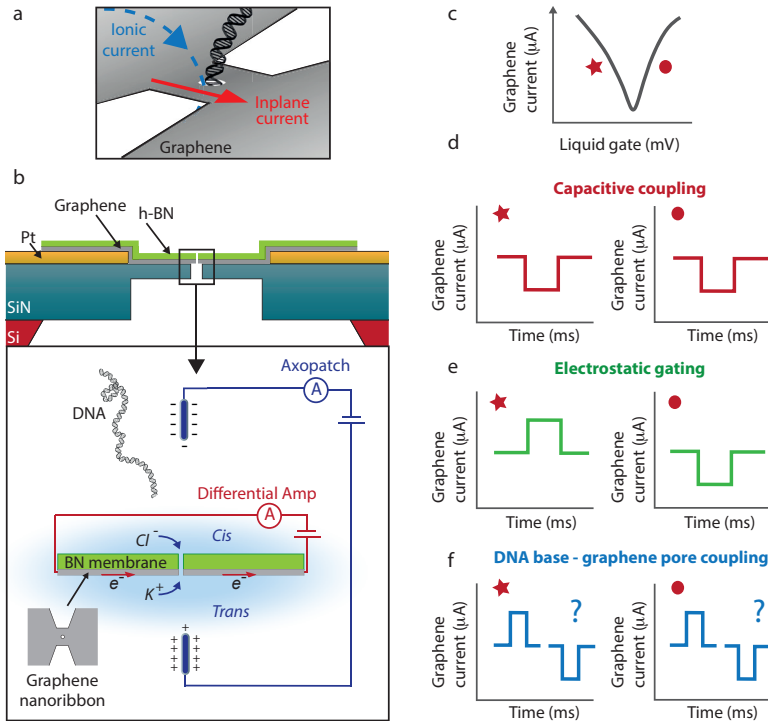


**Figure 6.1: Transverse current measurement for DNA detection.** (a) Concept of the experiment: Both the inplane current through a graphene nanoribbon and an ionic current through the nanopore are measured while a DNA molecule translocates through a nanopore in that ribbon. (b) Schematic representation (not to scale) of the device (top) and measurement setup (bottom). A silicon nitride membrane and platinum electrodes acts as substrate for the graphene nanoribbon, which is covered by a top-layer of h-BN, with a nanopore drilled through the BN/graphene stack. The graphene nanoribbon is exposed to the liquid on the trans side (bottom). In the experiment, both the ionic current through a nanopore and the graphene transverse electronic current are measured. The ionic voltage probes that are used to drag the DNA through the nanopore, are concurrently used to gate the nanostructure. (c) With the liquid gate, the potential of the graphene can be swept such that the Dirac curve is obtained, revealing the ambipolar nature of the charge carriers in graphene. The DC operating point of the graphene device can be tuned to the left wing of the Dirac curve (star), representing negative transconductance, and to the right wing (circle), representing positive transconductance value. Three different types of signals can be measured: (d) Capacitive signals, which will always be of the same sign and will be independent on the Fermi level of the graphene. (e) Electrostatic interactions, either due to the negative charge of the DNA backbone or due to a potential change at the nanopore caused by DNA translocation. These will result in different signals on both sides of the Dirac curve: a current increase when the current is carried by holes (left wing), and a current decrease when electrons are the dominant carriers (right wing). (f) Current fluctuations due to non-electrostatic local interactions between the DNA bases and the graphene nanopore, which can lead to current enhancements or decreases. The question mark denotes that the sign of this signal is not *a priori* known, as different theories predict different outcomes, depending on device parameters.

Current modulations will depend on the type of carriers, where transport dominated by holes will lead to negative transconductance  $g_m$  (left wing of Dirac curve in Fig.6.1c), and transport dominated by electrons will result in positive transconductance  $g_m$  (right

wing of Dirac curve in Fig.6.1c). This electrostatic signal can be defined as  $I_e = g_m \Delta V_e$ , where  $\Delta V_e$  is a potential change that can have two possible origins. The first originates in the negative charge of the DNA backbone  $\Delta V_{e,1} = \Delta V_Q = \frac{Q_{eff}}{C_g}$ , with  $Q_{eff}$  the effective charge of the DNA<sup>42</sup>. And secondly, a contribution  $\Delta V_{e,2} = \Delta V_l$  due to a local potential change evoked by a perturbation in the electric field at the nanopore due to insertion of DNA into the nanopore, as already mentioned above<sup>39</sup>. Thirdly, we expect current signals due to non-electrostatic DNA base-graphene interactions (Fig. 6.1f). As calculated in a great number of theoretical reports<sup>23-34</sup>, the presence of a DNA base can lead to substantial current modulations that increase with the bias voltage applied to the graphene. However, the magnitude and sign of the current change that is induced depend on multiple factors, including the width of the structure, the position and size of the nanopore, the edge structure of the ribbon (zigzag or armchair), and the Fermi level of the graphene, and is therefore not known *a priori*.

The particular size of the graphene nanostructure that probes the presence of the DNA in the nanopore is of great importance. While previous theoretical work focused on sub-10nm wide ribbons, early experiments probed the transport only for 600-1000nm long and 50-200nm wide ribbons<sup>37,38</sup>. Here we measure on short and narrow graphene nanoribbons (minimum width  $w$ ) to maximize the sensitivity for effects near the nanopore. We also argue that short ribbon lengths ( $L$ ) are beneficial, because long ribbons are more prone to edge damage. Previous studies have shown that roughness and disorder along the edges may result in transport that is characterized by a series of quantum dots rather than by a single nanoribbon<sup>43,44</sup>. In addition, shorter nanoribbons feature a higher conductance. Therefore, we realized short and narrow nanoribbons of 30x30nm that were as small as experimentally feasible while explicitly also striving for a minimal amount of defects, which is nontrivial since most top-down patterning strategies (e.g. focused ion beams or etching/e-beam lithography<sup>43</sup>) lead to defect layers of tens of nanometers near the edges.

## 6.2 RESULTS

### 6.2.1 FABRICATION WORKFLOW AND DEVICE CHARACTERIZATION

We first describe the extensive fabrication protocol of our devices. The workflow is indicated in Fig.6.2a. Device fabrication is started with a wafer of silicon chips, with 500nm thick SiN membranes containing embedded platinum heaters. We spray coated e-beam resist from the backside and employed through-membrane e-beam lithography, to RIE etch 5x5 $\mu$ m windows of 100nm thickness in the silicon nitride membranes<sup>45</sup>. Platinum electrodes were deposited on top of the membranes, in which we patterned 400nm holes (panel (i) in Fig. 6.2a) to suspend graphene, which later enables sculpting of freestanding graphene. An exfoliated graphene flake (typically 10x10 $\mu$ m) is transferred on top of the SiN

6 | membrane (panel ii). Subsequently, the graphene is patterned using e-beam lithography and oxygen plasma etching into a 200x200nm square with four leads that each contact a platinum electrode (panel iii). This layout ensures that currents run nowhere else than through the graphene nanostructure. Then, a 30x30nm graphene nanoribbon is sculpted using high-temperature STEM at 300-600 °C with high precision<sup>46</sup> (panel iv). At such high temperatures, carbon ad-atoms knocked out by the e-beam or originating from C-rich contaminations in the environment, diffuse at high rates and instantly reoccupy vacancies in the graphene lattice, preventing carbon deposition and, importantly, preserving the crystallinity of the graphene<sup>47</sup>. The bottom row in Fig. 6.2a presents an example of the consecutive sculpting steps performed in the STEM, where the graphene (grey) can be distinguished from vacuum (black). An automated script is used to move the electron beam along predefined paths to make cutting lines (see Methods section for details), visualized by the dark lines in the STEM images. In between the sculpting, we switch to imaging for which we use a fast scanning e-beam with short dwell times ( $\mu\text{s}$ ) to be able to correct for drift in the microscope. A thin flake (3-7 layers) of h-BN is subsequently transferred on top of the nanoribbon as a support, and, more importantly, to represent the membrane for the nanopore experiments, *i.e.*, to enforce the DNA to translocate through the nanopore and not next to the sides of the graphene square. To prevent parasitic electrochemical currents during the nanopore measurements, a thick (1.5 $\mu\text{m}$ ) layer of polyimide is placed on top of the stack to coat the electrodes (panel vi). A 5x5  $\mu\text{m}$  area is exposed using e-beam lithography, such that after development a circular area with a diameter of approximately 10 $\mu\text{m}$  at the nanostructure uncovered. Finally, a 5nm nanopore is drilled with STEM at the center of the nanoribbon-BN stack (panel vii). Note that, using STEM imaging, the graphene can still be distinguished from the h-BN.

The resistances of the graphene nanoribbons were measured in a 2-probe configuration immediately after STEM sculpting (Fig. 6.2b). The structures demonstrated linear current-voltage characteristics (Fig. 6.2b) featuring an average resistance of  $R = 194 \pm 35 \text{ k}\Omega$  (mean  $\pm$  s.e.m.)(Fig. 6.2c). After high-temperature patterning in TEM, the contact resistances between the platinum and graphene were found to be low ( $\sim 1 \text{ k}\Omega$ ) and therefore not accounted for in the resistance determination. The graphene conductivity  $\sigma$  can be deduced from the conductance  $G$ , using the relation  $G = \frac{1}{R} = \sigma \frac{w}{L}$  (see Fig.6.6 for the conductance *versus* conductivity for our devices). The theoretical planar conductivity of graphene<sup>48</sup> is  $\frac{4e^2}{h}$ , with  $e$  the electron charge and  $h$  Planck's constant. However, experimental studies on graphene nanoribbons so far revealed conductivities closer to  $\frac{e^2}{h}$ , with narrower ribbons typically exposing (much) lower conductivities,<sup>49,50</sup> which likely can be attributed to damage in the graphene induced during nanopatterning. Figure 6.2d shows the data for our graphene nanoribbons (N=51), with a highest conductivity of 89  $\mu\text{S}$  ( $2.3 \frac{e^2}{h}$ ) and a median of  $17 \pm 2 \mu\text{S}$  ( $\pm$  s.e.m.) ( $0.44 \frac{e^2}{h}$ ).

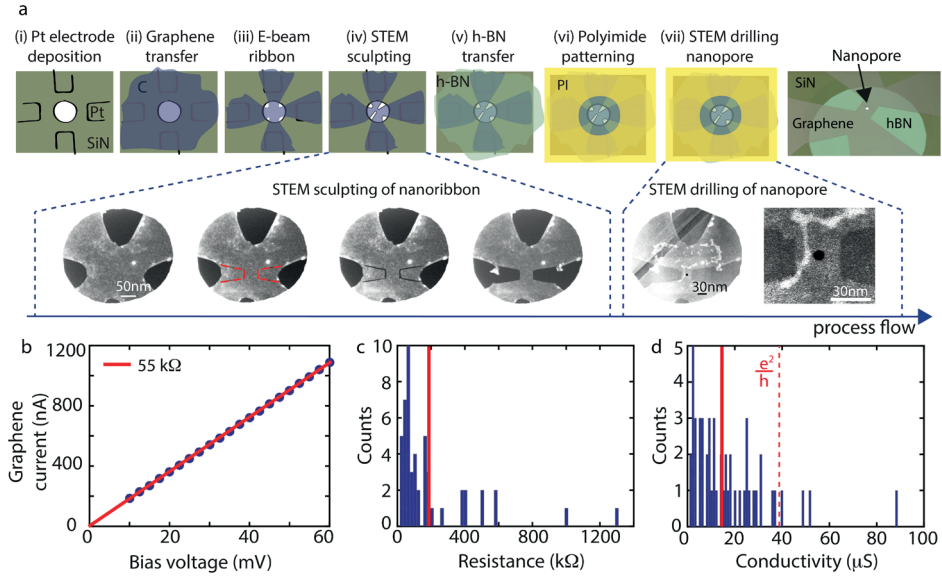


**Figure 6.2: Fabrication procedure and device characterization** (a) Process work flow of the device fabrication. Top: schematic images showing the sequential patterning steps. Bottom: STEM images of a single nanoribbon device, where grey represents the graphene and black is vacuum. In the second image the cutting lines that are to be made with STEM are marked with a red dotted line. When the cutting lines are subsequently connected, the graphene is removed. After the BN transfer, some wrinkles of the h-BN flake are visible. After the polyimide patterning, a 5nm nanopore is drilled through the stack of graphene and h-BN. (b) Example of a current-voltage measurement. (c) Ribbon resistances as measured directly after sculpting at room temperature. We find an average resistance of  $194 \pm 35 \text{ k}\Omega$  ( $\pm$  s.e.m.) (indicated by the vertical red line), deduced from 51 ribbons. (d) Conductivity of the graphene nanostructures, as calculated from  $G \sim \sigma \frac{w}{L}$  for 51 STEM ribbons. The average conductivity measured in this study was  $17 \pm 2 \mu\text{S}$  ( $\pm$  s.e.m.) (indicated by the vertical red line). For reference, the red dotted line indicates  $\frac{e^2}{h} \sim 38 \mu\text{S}$ .

### 6.2.2 DECOUPLING OF CAPACITIVE SIGNALS USING A DIFFERENTIAL CURRENT AMPLIFIER

We developed a custom-made differential current amplifier to be able to discriminate between signals in the graphene current generated by capacitive coupling, and signals due to electrostatic gating or modulations in the density of states. As explained in Fig. 6.3a, capacitive currents  $I_{C1,2}$  are created when temporal potential fluctuations couple to capacitances between the electrolyte and the conducting channel of the sensor, where the index 1,2 indicates the coupling to the left and right electrode of the graphene device, respectively. Here we distinguish between two relevant capacitance terms. First, the capacitance between the electrolyte and the graphene right at the nanopore ( $C_g$ ). And second, the capacitances that couple within the several micrometers range distance from the nanopore. The latter are represented by the capacitance between the electrolyte and the graphene that extends from the nanoribbon connecting the electrodes, and between the electrolyte



and the electrodes, which we combine in one term  $C_{lead}$  (see Fig. 6.3a). Any local change of the potential  $\Delta V_i$  at the nanopore couples to the sensor's capacitance  $C_g$  to constitute a current  $I_{C1,2} = C_g \times \frac{\Delta V_i}{\Delta t}$ . Potential fluctuations that are not strongly localized at the nanopore,  $\Delta V_{nl}$ , for instance due to a jump in the applied gate potential, will couple non-locally to both  $C_g$  and  $C_{lead}$ :  $I_{C1,2} = (C_g + C_{lead}) \times \frac{\Delta V_{nl}}{\Delta t}$ . Capacitive currents are inherent to all nanopore sensors that are combined with a second electronic readout, such as transverse or tunneling currents. Our differential amplifier applies opposite potentials to the two electrodes connected to the graphene nanoribbon, see Fig. 6.3ab, (+) to electrode 1 on the left and (-) to electrode 2 on the right, with respect to the ground potential of the liquid. All capacitive currents are independent of the electrode potential, and thus of equal sign at both electrodes, while, by contrast, any resistance modulation leading to a current signal in the graphene nanostructure ( $I_g$  in Fig. 6.3a) will be of opposite sign at each voltage electrode (Fig. 6.3c). The differential current amplifier is designed such that we detect only current contributions that are dissimilar at the two measurement electrodes, while all induced signals that are equal in sign will be subtracted (see Fig. 6.3c).

Through this differential measurement, we thus eliminate all capacitive contributions to the inplane current while retaining any contributions due to resistive modulations of the graphene nanoribbon current. To show the principle of the differential current measurement, we performed SPICE simulations (Fig.6.7). DNA events were simulated by 1ms-duration voltage steps of 100mV, and graphene resistance modulations were simulated by 1ms-duration resistance increases. The current at each electrode was measured by a separate op-amp, each obtaining a unique signal. After the subtraction of the two current signals measured at the two electrodes, the differential current signal solely represented the resistance modulation in the graphene, while the addition of the two responses yielded the capacitive signal (see Fig.6.7). In reality, the amplifier eliminates the capacitive component from the inplane current signals, while also measuring the common mode DC potentials of the graphene conducting channel with respect to ground at the two electrodes. From this common-mode potential measurement in  $V_{com}$  we can deduce the capacitive currents, which are related to all potential fluctuations, local and non-local, where  $C_{lead}$  is in parallel with  $C_g$ .

As it is exposed to the electrolyte solution, the graphene nanoribbon is gated by the applied voltage  $V_{ion}$  on the trans ionic reservoir. Since  $V_{ion}$  thus has a dual role, viz., it is necessary for controlling DNA translocations as well as changes the DC operating point of the graphene nanoribbon, we equipped the amplifier with additional 'knob' to adjust the gate voltage,  $V_{lift}$ , which lifts the DC operating potential of the graphene nanostructure with respect to ground (Fig. 6.3b). As both  $V_{ion}$  and  $V_{lift}$  affect the transconductance of the nanoribbon (Fig.6.3d), the effective gating potential at the graphene nanostructure can

be defined as  $V_{gate} = V_{ion} - V_{lift}$ . This is advantageous, since this provides the ability to gate the sensor through  $V_{lift}$ , readjusting the operating point to optimize  $g_m$  each time that the  $V_{ion}$  potential changed. As  $V_{lift}$  acts opposite to  $V_{ion}$ , the Dirac curves measured as a function of  $V_{lift}$  or  $V_{ion}$  are mirrored about the y-axis (Fig. 6.3d). The combination of the DC bias voltage  $V_{bias}$ , which sets the in-plane current in the graphene nanoribbon, and  $V_{ion}$  and  $V_{lift}$  can be chosen such that we perform the DNA measurements at the highest transconductance.

\

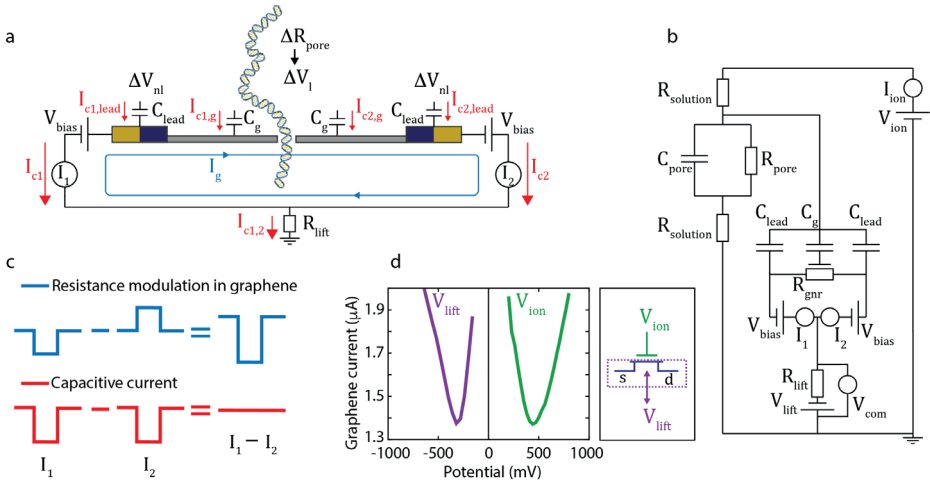


**Figure 6.3: Capacitive coupling and the differential current amplifier** (a) Potential fluctuations couple to the graphene signal through the capacitance  $C_g$  between the electrolyte and the graphene nanosensor (grey), which is in parallel with the lead capacitance  $C_{lead}$  between the electrolyte and the graphene leads contacting the electrodes (dark blue) and to the electrodes themselves (yellow)). We distinguish local potential fluctuations  $\Delta V_l$  that are induced by DNA translocations, from non-local potential fluctuations  $\Delta V_{nl}$  due to modulations in the gate voltage. On the two electrodes (electrode 1 on the left and electrode 2 on the right), a voltage of opposite sign but equal magnitude is applied ( $V_{bias}$ ). Resistive current modulations in the graphene  $I_g = g_m \Delta V$  are indicated in blue. (b) Equivalent circuit diagram of the setup.  $V_{ion}$  is the applied potential during DNA measurements which simultaneously gates the graphene;  $V_{lift}$  is used as extra ‘knob’ to tune the gate voltage to a favorable point on the Dirac curve;  $V_{bias}$  sets the bias potential at the electrodes;  $I_{ion}$  represents the ionic current (Axopatch 200B);  $I_1$  and  $I_2$  are the lead graphene currents that are used in the differential graphene current measurement; and  $V_{com}$  measures the DC potential of the graphene. (c) Principle of the differential current measurement. Due to the opposite potentials at the two electrodes, resistive modulations in the graphene will yield currents  $I_1$  and  $I_2$  of opposite polarity. The capacitive currents are, however, independent of the electrode potentials and thus hold the same polarity. Subtraction of the two current measurements  $I_1$  and  $I_2$  leads to the differential measurement, where the capacitive-current contribution vanishes whereas the graphene resistance modulations are maintained. (d) Graphene current versus applied gate potential. The purple trace was obtained by sweeping  $V_{lift}$  at  $V_{ion} = 0\text{mV}$ ; the green trace was acquired by sweeping  $V_{ion}$  while  $V_{lift} = 0\text{mV}$ . During the experiments,  $V_{lift}$  and  $V_{ion}$  are both used to gate the graphene, and the effective gate potential can be expressed as  $V_{gate} = V_{ion} - V_{lift}$ .

Finally, we note that the  $V_{com}$  readout can also be used to monitor any leakage of the transverse current channel to the liquid, which could occur through unintentional electrochemical processes at the electrodes or on the graphene surface. In the ideal case, the measured common mode potential of the graphene should equal the  $V_{ift}$  applied potential. An offset between the two indicates that there is a leakage. Using this approach, we showed that electrochemical leakage currents of tens of nanoamperes can arise if electrodes on the device are only partly coated, while an intact polyimide layer on the chip resulted in zero leakage currents (Fig.6.9).

### 6.2.3 PROOF-OF-PRINCIPLE EXPERIMENTS

We benchmarked our amplifier and graphene devices by first performing a series of control measurements. We simulated DNA translocations by voltage pulses  $\Delta V_{ion}$  (-20mV, 1ms) applied to the ionic voltage channel ( $V_{ion} = 300\text{mV}$ ), and detected the response in the graphene transverse current  $\Delta I_g$ . Furthermore, we probed the current signals in the graphene at three different values of  $V_{bias}$  (25, 50 and 100mV) and tuned the DC operating point to either side of the Dirac curve such that the conductance was dominated by either p- or n-type carriers ( $V_{ift} = 300\text{mV}$  (n-type) vs. +50mV (p-type) (indicated by the orange and blue line that cross the solid lines measured at  $V_{ion} = 300\text{mV}$  in Fig. 6.4a), leading to a  $g_m$  of different sign. As shown in Fig. 6.4a, we measured, as expected, a near-linear  $V_{bias}$  dependence of the graphene current signals (see Fig.6.10).

The most noteworthy result is presented in the top panels of Fig. 6.4b, where we measured a different-sign response of the graphene current to the gate voltage, depending on the choice of the operating point: downward spikes for  $V_{ift} = -300\text{mV}$  and upward spikes for  $V_{ift} = +50\text{mV}$  (Fig. 6.4c). The values of transconductance derived from the Dirac curves ( $g_m = -1.1 \text{ nA/mV}$  and  $0.7\text{nA/mV}$ , respectively) were in good agreement with ones obtained from graphene current responses to the  $V_{ion}$  pulses ( $g_m = -1.1\text{nA/mV}$  and  $1\text{nA/mV}$ , see Fig.6.10b). At the same time, the currents induced by capacitive couplings, are measured in the common-mode channel (bottom panels Fig. 6.4b). As expected, these signals (i) remain of the same sign at any  $V_{ift}$ , and (ii) do not increase in magnitude with increasing  $V_{bias}$ . This clearly asserts that our differential amplifier separates, as designed, the transverse current response due to gating of the graphene sensor, recorded in the differential channel, from signals caused by capacitive coupling which are picked up in the common mode channel of the amplifier.

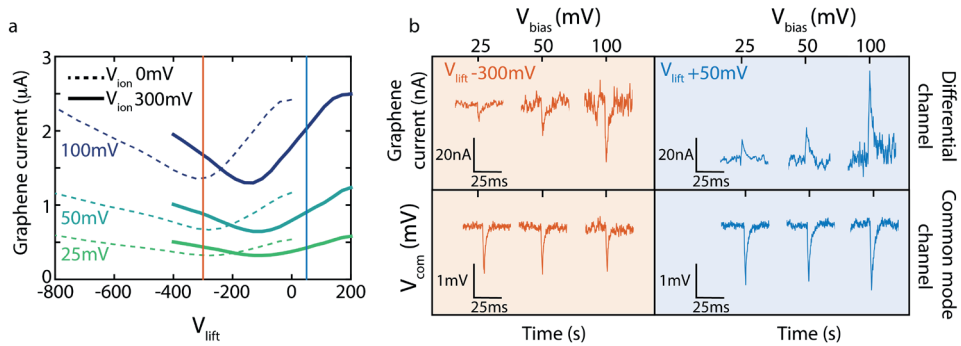


**Figure 6.4: Proof of principle.** (a) Mapping of the graphene current response to a sweep in  $V_{lift}$  gate potential, at different  $V_{bias}$  (25 mV, green, 50 mV, turquoise, and 100 mV, purple), and for two values of  $V_{ion}$  (0 mV, dotted line, and 300 mV, solid line). The orange and blue lines indicate the  $V_{lift}$  gate potentials at which we measure the pulses displayed in panel b (*i.e.*,  $V_{lift} = -300$  mV and  $+50$  mV, respectively). (b) Response from the differential current amplifier to  $-20$  mV pulses of 1 ms in  $V_{ion}$ . The positive probe ( $V_{ion} = 300$  mV) is located on the graphene side (*i.e.* trans side) of the membrane. The response in the graphene current is, as expected, different on both sides of the Dirac curve: We observe current dips (orange) for  $V_{lift} = -300$  mV, and current peaks (blue) for  $V_{lift} = +50$  mV. Measurements were done at three values for the bias voltage, 25, 50, and 100 mV. As expected, larger signals are measured in the graphene current for higher bias voltages. The common mode channel presents the capacitive signals, and as expected, these do not change sign or magnitude, as these do not depend on the gate voltage nor the bias voltage. A signal amplitude of 1 mV corresponds to a current of 200 pA.

6

#### 6.2.4 PROBING DNA TRANSLOCATIONS

Finally, we performed DNA translocation experiments with our graphene nanostructure devices, where we simultaneously recorded the time traces of the ionic nanopore current and the graphene transverse current, using the setup shown in Fig. 6.1a. It proved to be extremely challenging to perform such experiments successfully, because of constraints in the extensive fabrication protocol and additionally because it was very difficult to wet the nanopores. The latter is likely caused by the hydrophobic nature of the graphene. Note that the samples cannot be treated with oxygen plasma or piranha solution as this will remove the graphene. Attempts to wet the pores through ethanol flushing often resulted in breaking of the nanostructure. These effects rather unfortunately reduced our yield of successful experiments dramatically. However, we managed to obtain consistent data with one sample (out of 180 devices that we started fabricating) with a good enough signal-to-noise ratio to study the signals in detail.

After addition of 20 kb plasmid DNA, we detected current blockades in the current trace of the ion flow through the graphene nanopore as well as simultaneous current signals in the electronic current running through the graphene nanostructure. An example trace of such events is shown in Fig. 6.5a (and more example events are presented in Fig. 6.11). Clearly, the signals were fully synchronized in time as for 99.9% of the events in the ionic current

(N=1429) we also observed a very clear signature in the graphene current. Furthermore, an anti-correlation is observed in the sign of both signals: a decrease of the ion current, which unambiguously signals the translocation of DNA at these high-salt conditions, corresponds to an increase in the current measured through the graphene nanoribbon. In other words: the passage of the DNA leads to a temporarily lowered resistance of the graphene nanoribbon.

About 1400 of these events were measured, as presented in the scatterplots in Fig. 6.5bc. The data in Fig. 6.5b show that the correlation also holds for the magnitude of the current deviations in both channels, *viz.* a larger current dip in the ionic current corresponds to a larger current increase in the graphene current. The magnitude of the signal in graphene channel furthermore scaled with the bias voltage (inset Fig. 6.5b), while the ionic current signals remained unchanged (Fig.6.12b). The signal-to-noise ratio (SNR) in the graphene current is comparable to the SNR in the ionic current (see Fig. 6.12c) (SNR=4.2-4.5 for the graphene current *versus* 3.8-5.4 for the ionic current at 20-30mV bias voltage). Figure 6.5c displays the ionic conductance blockades ( $0.46 \pm 0.19$  nS (median  $\pm$  s.d.)) and the graphene conductance signals ( $0.16 \pm 0.08$   $\mu$ S (median  $\pm$  s.d.)) *versus* the observed translocation times. The distribution of the observed translocation time (top of Fig.6.5c) has a median of  $2.3 \pm 8.9$  ms ( $\pm$  s.d.). The wide spread of translocation times shows that a substantial amount of events is much longer, which may be due to interactions between the DNA molecule and the graphene. Interestingly, the subset of events with longer translocations times (all  $>2.5$ ms), showed a 16% larger graphene current signal. The transconductance recorded prior to the measurements was  $-0.25$ nA/mV (see Fig. 6.5d), at the potentials at which we performed the measurements. For the large majority of the events, no signal was detected in the common mode channel (see Fig.6.5a for a typical example). For a small minority of the events (3.5%), we measured a correlated signature in common mode channel of  $\sim 100$   $\mu$ V magnitude, corresponding to transient currents of approximately 10pA. Eventually, after about 30 minutes of measurement time, the nanostructure broke and the current was lost in the graphene nanostructure. Although the nanopore current had significantly increased to 16nA, indicating a much increased pore size, events could still be detected in the ionic current, but the signatures in the graphene current were lost.

### 6.2.5 DATA INTERPRETATION

To interpret these signals, we first consider that we measured on the left wing of the Dirac curve with  $V_{ift} = 0$ mV and  $V_{ion} = 300$ mV, *i.e.*, with p-type conduction in graphene. Electrostatic interactions in this case would yield, as observed, a current enhancement in the graphene when the DNA molecule translocates through the nanostructure. Electrostatic gating by the negative charge of the DNA backbone and gating due to a change in the local potential at the nanopore during DNA translocation, will both induce a current enhancement through  $I_g = g_m \Delta V$ . From the measured transconductance  $g_m = -0.25$

nA/mV (see Fig. 6.5d), and the median of the graphene current signals  $I_g = 3.8\text{nA}$  measured at  $20\text{mV } V_{bias}$  (see inset Fig. 6.5b), we deduce a  $\Delta V \cong -15\text{mV}$ .

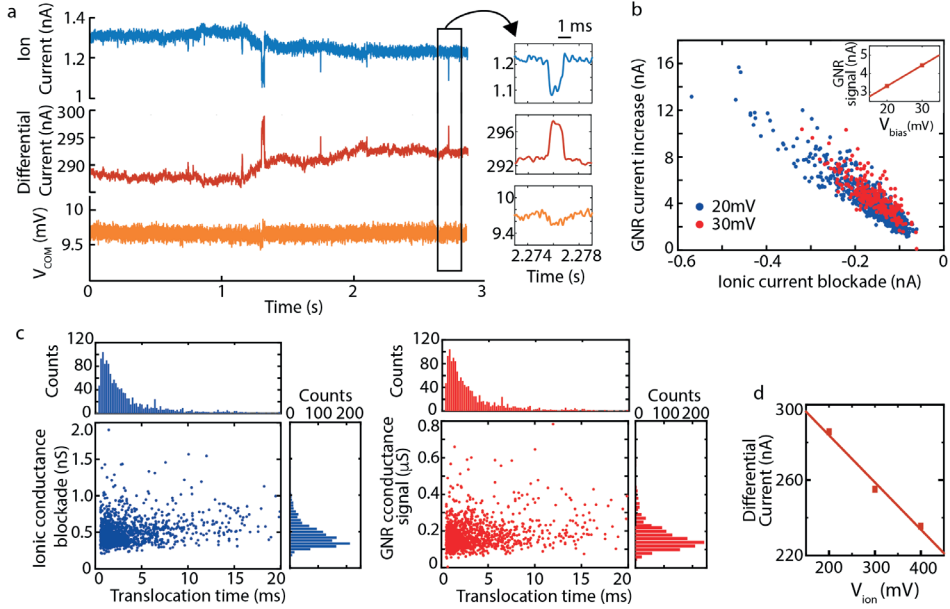


**Figure 6.5: DNA translocation through a nanopore in a graphene nanostructure.** (a) Example traces (filtered at 2kHz) that are simultaneously collected in three channels: the ionic current (blue), graphene current (red), and the common mode voltage channel (yellow). The right panel shows a zoom of one DNA event in the three different channels. (b) Scatterplot showing the ion current signals *versus* the graphene current, for 20mV (blue) and 30mV bias voltage (red). The ionic potential was held constant at 300mV. All events were detected at  $V_{lift} = 0\text{mV}$ . Larger current blockades in the ionic current (*i.e.*, more negative values) correspond to larger upward peaks in the graphene current (more positive). Inset: Medians of graphene current signals *versus* bias voltages. (c) Ionic conductance blockades (blue) and graphene conductance signals (red) *versus* DNA translocation time. The median of the translocation time distribution is  $2.3 \pm 8.9\text{ ms}$  ( $\pm$  s.d.). The ionic conductance blockade observed is  $0.46 \pm 0.2\text{ nS}$  (median  $\pm$  s.d.), the graphene conductance signal measured is  $0.16 \pm 0.08\text{ }\mu\text{S}$  (median  $\pm$  s.d.). (d) Graphene current measured *versus*  $V_{ion}$  (at  $V_{lift} 0\text{ mV}$ ), recorded prior to the DNA experiments. From the slope of the fit we deduce a transconductance of  $-0.25\text{ nA/mV}$ .

What underlies this induced voltage change? We first discuss the potential change that the charge of the DNA backbone can generate through  $\Delta V_Q = \frac{Q_{eff}}{C_g}$ . We consider that the Debye screening length at 1M KCl is approx. 0.3nm, and that at any distance further than that no charge is probed. The maximum charge of the DNA as seen from the nanopore rim in 1M KCl is approximated to be  $2e$  or a fraction of that (as the DNA basepairs each carry an effective charge of  $0.5e^{51}$  and as the effective graphene length is approx.  $0.6\text{nm}^{10}$ , see section 6.10.2 for details). To approximate a value for the relevant capacitance of the graphene, we consider a ring of 1nm extending from the nanopore rim,

to find  $C_g \cong 5 \times 10^{-19}$  F (see section 6.10.1), yielding an estimate of  $\Delta V_Q$  ranging between -30mV and -600mV. It must be noted, however, that the capacitance value extracted from the measured transconductance is substantially smaller, which would correspond to much higher  $\Delta V_Q$  values. Secondly, we examine the potential change at the nanopore that occurs due to the insertion of DNA in the nanopore. With the use of an analytical relation,<sup>38,40,42</sup> we approximate the potential change at the nanopore to be about -50mV, based on our nanopore geometry and DNA plasmid analyte (see section 6.10.2 and Fig.6.14), which can be an overestimation because surface charges are not accounted for in this relation<sup>38</sup>.

6 | From these estimates, we conclude that the measured response signals in the graphene current can be explained as due to the local potential change and DNA charge. The approximations discussed above, show that both effects can induce a  $\Delta V$  in the order of tens of mV, which is close to what we measure here (-15mV). Furthermore, it is possible that the graphene current signals are partly due to a non-electrostatic coupling between the nanopore and the DNA bases<sup>23-34</sup>, leading to a modulation in the density of states which causes a change in the graphene nanoribbon conductance. Unfortunately, different theories provide rather conflicting predictions regarding the signal sign and magnitude, which hinders comparison to our data.

Finally, we comment on those rare (3.5%) events where we measured  $\sim 100 \mu\text{V}$  signals in the common mode channel, which correspond to  $\sim 20\text{pA}$  transient capacitive currents. The local capacitance between the electrolyte and the graphene at the nanopore is simply too small to induce such currents through  $\frac{\Delta V}{\Delta t} \approx \frac{I_c}{C_g}$  (see section 6.10.3). From this relation, it can be conceived that pA currents rather correspond to capacitances in the order of pF. The capacitance of the area exposed to liquid was measured to be  $\sim 20\text{pF}$  (see section 6.10.3). Therefore, we attribute these events to non-local interactions  $\Delta V_{nl}$  to the capacitances of the leads  $C_{lead}$  (i.e. to the graphene capacitance at a distance from the nanopore). This is supported by Spice simulations that show a  $100 \mu\text{V}$  response in the common mode channel to 10mV voltage steps when the capacitance at the nanopore is increased to 20pF, see section 6.10.3 for details.

### 6.3 CONCLUSIONS

In this paper, we have shown that it is possible to fabricate freestanding 30x30nm graphene nanoribbons with a 5 nm nanopore in its center, that allow to measure resistive modulations in the inplane graphene current due to DNA translocation through the nanopore. Due to our high-temperature STEM sculpting approach, in combination with transfer techniques to assembled stacked structures of 2D materials, we were able to make graphene nanostructures that are significantly smaller than what was studied before. With our custom-made differential current amplifier, we presented a new method that enables

to discriminate between resistive modulations in the graphene current and signals due to capacitive coupling. Despite this success, we also have to note that, unfortunately, the fabrication procedure and protocol for DNA measurements were overly challenging, yielding an unacceptably low yield (as we successfully obtained dual signals in only 1 out of 180 devices – see Materials and Methods for details). In future studies, a more scalable approach could be explored, such as e-beam lithography with ion beam milling<sup>52</sup> instead of TEM sculpting, leading to a higher device yield. Furthermore, other 2D materials such as MoS<sub>2</sub> and WS<sub>2</sub><sup>18,19</sup>, that can be oxygen-plasma treated to render the pore hydrophilic, could provide interesting alternatives to graphene, using the same approach of inplane current detection towards high-bandwidth DNA sequencing.

## 6.4 METHODS

### 6.4.1 FABRICATION PROCEDURE

Devices were built on top of a silicon wafer, diced into silicon chips with 500nm thick silicon nitride membranes with embedded platinum heater coils, which were used to locally heat the graphene during STEM sculpting. Windows were etched in the backside of the ‘heaterchips’ using backside spraycoating of e-beam resist, through-membrane e-beam lithography followed by RIE etching to obtain windows to 100nm thickness<sup>45</sup>. Platinum electrodes were deposited on the topside of the chips using e-beam lithography (200nm CSAR 6200.09 resist) and metal evaporation (10nm Ti, 60nm Pt). Next, 400nm holes were patterned using e-beam lithography (800nm resist layer CSAR 6200.18) and RIE etching (50W, 25:25 sccm Ar:CHF<sub>3</sub>, 80μbar). Monolayer graphene flakes were exfoliated onto silicon wafers with 90nm SiO<sub>2</sub> and transferred onto the chips with platinum electrodes and holes in the membranes using the wedging transfer<sup>53</sup>. To prevent leakage currents on the membrane, and because sculpting with a transmission electron microscope (TEM) is difficult and time-consuming on supported graphene, graphene structures consisting of a 200x200nm square with leads were pre-patterned using e-beam lithography (200nm PMMA A4) and oxygen plasma etching (40s, 20W, 20sccm, 800μbar), and the PMMA was removed through soaking in room-temperature acetone overnight. To prevent polymer residues after lithography, fresh stocks of PMMA were used. Subsequently, a 30x30nm graphene nanostructure was sculpted using high-temperature STEM, as detailed below. After this high-temperature patterning in the TEM, the contact resistances were low (~1kΩ). To support the freestanding sculpted nanoribbon and to cover the cavities next to the ribbon (in order to make the nanopore the only possible way for the DNA to pass), we transferred thin (3-7 layer) flakes of h-BN on top of the nanoribbon using wedging transfer. h-BN is a good insulator, relatively free of dangling bonds, it has an atomically smooth surface, and it has a lattice that is very similar to that of graphene, which makes it a good material to make stacked structures with graphene<sup>54</sup>. h-BN flakes were exfoliated onto silicon wafers



6 | with 90nm SiO<sub>2</sub> and the flake thickness was determined using optical microscopy. In order to do this transfer, a glass mask was placed on top of the target device with the graphene nanostructure during the oxygen plasma cleaning step. The deposition of a very thick polyimide layer (1.5μm) on top of the electrodes proved to be the only strategy to overcome electrochemical leakage during our nanopore measurements. Before patterning, samples were pre-baked at 100°C, an adhesion layer vm651/vm652 0.1% in H<sub>2</sub>O was spincoated (3000rpm) on top and baked for 2 minutes at 120°C. Next, the layer of polyimide was spun on top (PI-2545) at 5000rpm to obtain a thickness of 1.5μm. The polymer was soft baked at 90°C on a hotplate for 10 minutes. Finally, a 200nm layer of PMMA (A4 4000rpm) was spincoated on top and baked at 90°C on the hotplate for 5 minutes. A small area of 5x5 μm<sup>2</sup> at the nanostructure was exposed to the e-beam. After the development of the PMMA toplayer in MIBK (25% in IPA), and solvation of the exposed PI in diluted tetramethylammonium hydroxide (Mf321, 25% and 10%), a circular area with diameter ~10μm was cleared, and the PMMA was subsequently removed in room temperature acetone overnight. Finally, the nanopore was drilled in STEM mode, while using Joule heating to overcome carbon contamination. Before nanopore measurements were performed, the samples were baked at 180°C for 5 minutes on a hotplate, to cure the polyimide.

#### 6.4.2 STEM SCULPTING OF NANORIBBONS AND NANOPORES

Sculpting of graphene nanoribbons and nanopores was performed using the focused electron beam of a Transmission Electron Microscope (TEM), model FEI Titan 80-300, operated in Scanning mode (STEM). The fine probe of the electron beam (0.1 nm spot size, 0.15 nA beam current, 5ms dwell time, doses ranging between 10<sup>7</sup>-10<sup>8</sup> e/atom), combined with the 300 keV electron energy, allowed us to knock off single carbon atoms from the graphene lattice, so that we could “sculpt” graphene according to our needs<sup>46</sup>. Immediate feedback on the sculpting process was easily obtained by switching the microscope to imaging mode (5s dwell time and doses ranging between 10<sup>4</sup>-10<sup>5</sup> e/atom). During sculpting, the electron beam decomposed the hydrocarbons which were adsorbed on graphene surface (originating from the TEM vacuum chamber and organic residues from solvents used during sample preparation), causing carbon atoms to “stick” near the illuminated area and grow into a thin amorphous carbon layer. Such carbon deposition was minimized by (1) the high temperatures (>300°C), at which the surface diffusion of carbon ad-atoms is enhanced preventing ad-atom accumulation in the spot where the e-beam illuminates the sample, while graphene lattice recrystallization or “self-repair” is induced at high temperatures (~500°C)<sup>46,47,55</sup>, and (2) the high vacuum (~10<sup>-8</sup> mbar), as a lower total pressure implies a lower rate of impinging carbon atoms on the surface. For Joule heating, the Pt electrodes on the membrane were used to pass a high current densities (~10<sup>8</sup> A/cm<sup>2</sup>) through the graphene ribbon, to locally reach a very high temperature<sup>55</sup>. After polyimide deposition, the devices could not be heated above 300 °C, as the polymer would turn conductive at such

temperatures. We therefore aimed for high vacuum to prevent carbon contamination, and kept the samples in the TEM vacuum chamber for 12-24 hours, until the vacuum reached  $\sim 5 \times 10^{-8}$  mbar.

#### 6.4.3 DEVICE YIELD

The elegance of our approach is that it allows exquisite control of the graphene nanostructure properties, but its downside is that the device fabrication is extremely challenging, leading to a low device yield. In total, we started the fabrication procedure on about 180 devices, of which 51 graphene nanostructures were sculpted with STEM, 15 of which survived the h-BN transfer, polyimide passivation and nanopore drilling. It showed to be very difficult to establish a decent nanopore current, likely due to the hydrophobic nature of the graphene. Attempts to wet the nanopores by ethanol flushing frequently resulted in breaking of the nanostructures. We managed to perform DNA translocation measurements on a few devices, but with only two devices we measured clear DNA signals in the ionic current channel, of which in one device, we managed to measure clear resistive modulations in the graphene current due to DNA, occurring simultaneously with the ionic current events. Comparison of the transconductances, noise levels, and ionic signals of the two samples are given in Table S1 (SI). In the sample where we did not resolve graphene signals, the sensitivity was lower and the noise levels were higher.

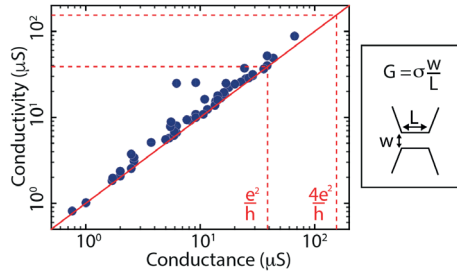
#### 6.4.4 NANOPORE EXPERIMENTS

The samples were mounted in a PEEK flowcell that fits a dedicated holder to insert Ag/AgCl probes in the flow chambers and to be able to connect the electrodes to the electrode pads. The  $V_{ion}$  gate potential is set with the use of an Axopatch 200B patchclamp amplifier, connected to two Ag/AgCl electrodes on each side of the membrane. The positive electrode was located on the graphene side (trans) of the membrane. The platinum electrode pads on the chip were contacted by PoGo pins connected to the differential pre-amplifier, such that the amplifier is in close proximity to the graphene nanostructure (minimizing input capacitances). Nanopore measurements were performed with 1M KCl, 10mM Tris-HCl buffer solution (pH 8.1), and 3 ng/ $\mu$ l 20kb DNA plasmids dissolved in the same buffer. We measured the transconductance by sweeping  $V_{ion}$  in the range of the voltages that were used during the DNA measurements (in our case 200-400mV) at selected  $V_{lift}$  gate potentials. Typically, the measured sensitivities ranged between 0.1-2nA/mV (varying per device). Due to the presence of the graphene nanostructure, we were not able to oxygen plasma or piranha clean the samples, making it difficult to wet the nanopore during DNA measurements. Attempts to wet the nanopores by flushing ethanol and buffer often resulted in breaking of the nanoribbons. The events were extracted from the ionic current traces using Tranzalyser<sup>56</sup> and the corresponding time traces in the differential and common mode channels were analyzed with Matlab.

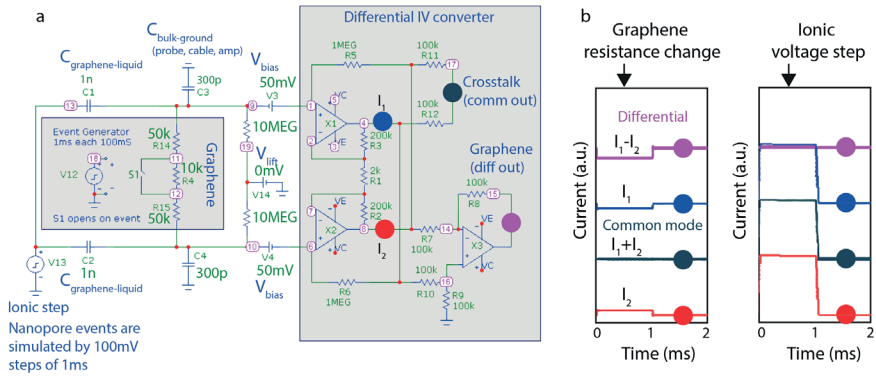
## 6.5 SUPPLEMENTARY INFORMATION

Experimental data, simulations and calculations, including SPICE simulations, prevention of electrochemical leakage, transconductance and sensitivity of proof-of-principle measurement, examples DNA translocation events, sensitivity of the graphene nanoribbon, graphene capacitance determination, data interpretation, and transconductance, signal and noise details of samples.

6

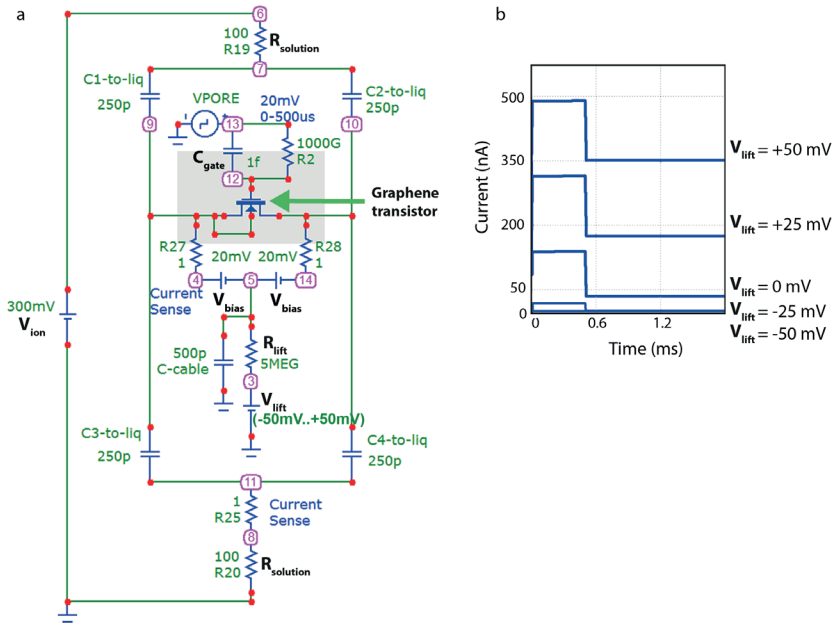


**Figure 6.6: Conductivity versus conductance plotted on logarithmic axes.** The graphene conductivity can be calculated from the measured conductance, using the relation  $G = \frac{1}{R} = \sigma \frac{W}{L}$ . The results follow the line  $G = \sigma$  (red diagonal) showing that the geometry of our graphene nanostructures indeed represents the intended  $L \approx w$ . The two dotted lines indicate the typical conductivity experimentally observed for nanoribbons  $\frac{e^2}{h}$  and the maximum 'bulk' conductivity of graphene  $\frac{4e^2}{h}$  at room temperature.

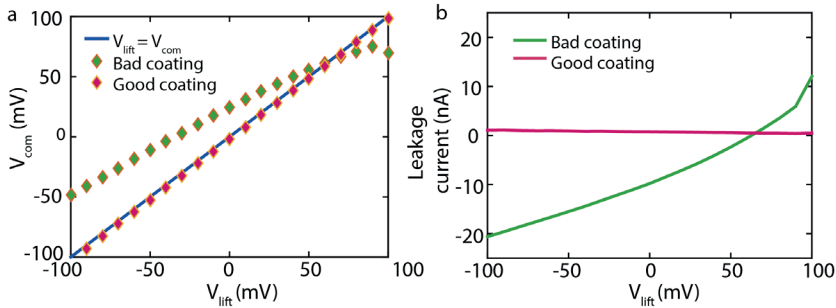


**Figure 6.7: Spice simulations to show the principle of the differential amplifier.** (a) Nanopore events are simulated by 100 mV voltage steps of 1ms. A graphene resistance change is simulated by changing the graphene resistance from 100kOhm to 110kOhm for 1ms. The response is probed at 4 different nodes: blue dot: after first op-amp, red dot: after second op-amp, grey dot: common mode output, pink dot: differential output. (b) Current response *versus* time on the graphene resistance increase (left) and the 100mV ionic step (right) as probed in the 4 points (red, blue, grey, pink) indicated in panel a. Both the graphene and the ionic ‘event’ occur between 0 and 1ms. The two op-amps (red and blue) measure both signals, and the graphene signal has opposite polarity in the two measurements (see main text Fig.6.3a-c). The capacitive signal, however, is equal in sign. At the common mode probe (grey) we observe an addition of the red and blue, divided by two, yielding only the capacitive response. In the differential readout (pink), we observe the difference between the two signals as measured in the red and blue probes, thus yielding solely the graphene response.

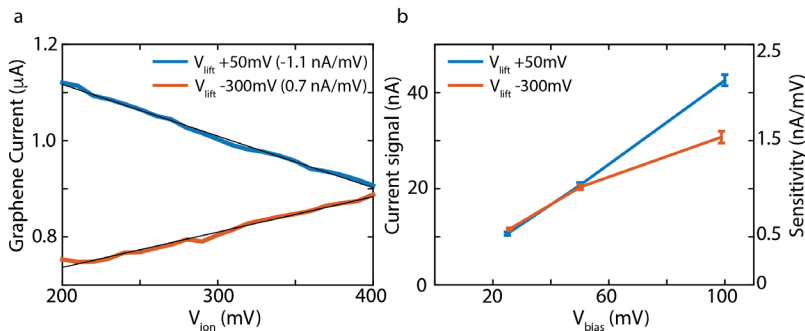
6



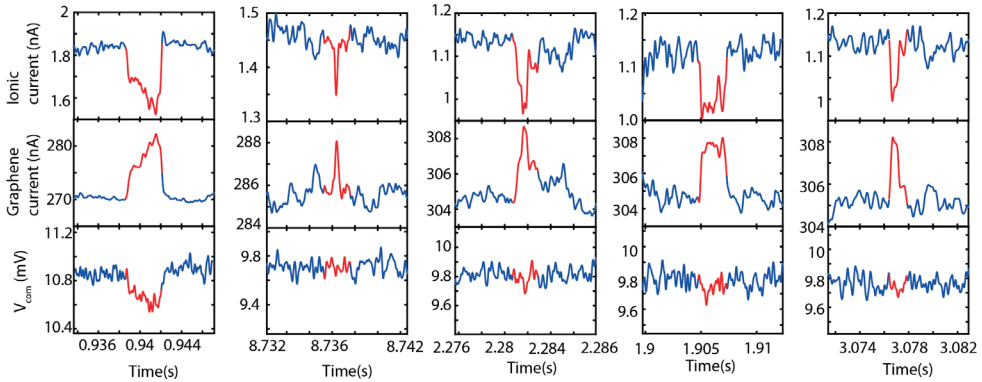
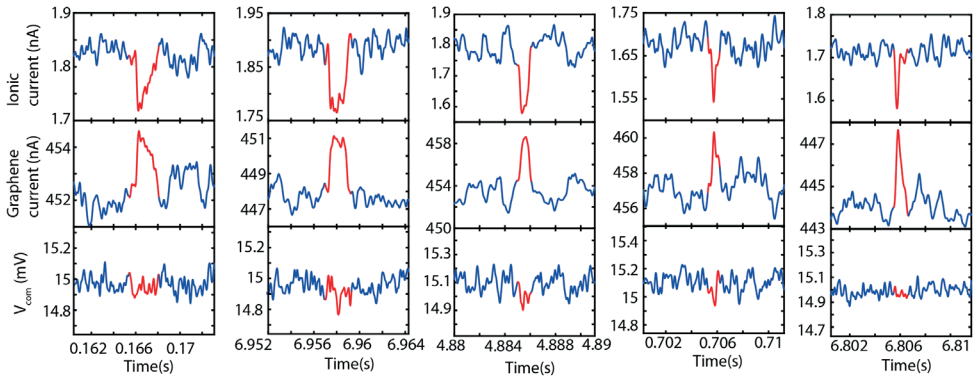
**Figure 6.8: SPICE simulation of the equivalent circuit diagram of the electronic circuit in Fig. 3b.** (a) Potential modulations at the nanopore are simulated by a 500  $\mu$ s pulse of 20mV. The graphene nanostructure functionality is simulated by a transistor. The current in the graphene as a result of the voltage pulse is measured in resistor R27, which has a value of 1  $\Omega$ , which solely functions to probe the current. (b) Response in the graphene probed in R27 to the 500  $\mu$ s voltage step of 20mV, while the  $V_{lift}$  potential is swept from -50mV to +50mV, showing that the sensitivity in the graphene increases with  $V_{lift}$ .



**Figure 6.9: Polyimide coating of the electrodes prevent leakage currents** (a) Measured voltage  $V_{com}$  versus applied voltage  $V_{lift}$ . An offset between the applied voltage and measured voltage indicates a leaking into the liquid. When this measurement is done on a device on which the coating is partly peeled ('bad coating'), a clear offset results, while an intact polyimide coating (green) leads to a zero offset. With this approach, one can measure electrochemical leakage during the nanopore measurement. (b) The calculated leakage current versus  $V_{lift}$ . Currents are calculated through:  $I_{leakage} = 2 \times \left( \frac{V_{lift} - V_{com}}{R_{lift}} \right)$  with  $R_{lift} = 5M\Omega$ . A bad coating can lead to leakage currents of tens of nanoamperes at  $V_{lift} = \pm 100mV$ .



**Figure 6.10: Results of pulse experiments on a graphene ribbon device as delineated in Fig.6.4b** (a) Graphene current versus the ionic gate voltage, representing the transconductances at the two  $V_{lift}$  voltages measured, for  $V_{bias} = 50mV$ . The fits yield a transconductance of -1.1 nA/mV at  $V_{lift} = +50mV$  and 0.7 nA/mV for  $V_{lift} = -300mV$ . (b) Average current signals (left axis) and sensitivities (right axis) in the graphene as a function of  $V_{bias}$ . The graphene signal increases strongly with increasing bias voltage. The sensitivities are calculated by dividing the graphene current signal by the  $V_{ion}$  potential pulse of 20mV, which are in good agreement with the transconductances measured before the experiment, as presented in the graph in (a).

Example events  $V_{bias} = 20\text{mV}$ Example events  $V_{bias} = 30\text{mV}$ 

**Figure 6.11: Example events as monitored in three channels (ionic current, differential graphene current, common mode voltage).** Five example events are shown as measured at  $20\text{mV}$   $V_{bias}$  (top) or  $30\text{mV}$   $V_{bias}$  (below). The red part in the time trace is detected as ‘event’ in the ionic current trace by the event detection software. The corresponding time traces in the differential GNR current channel and common mode channel are presented accordingly. The graphene events in the graphene current correlate closely with the events in the ionic current channel. In the common mode channel, however, only 1.5% of the events shows a clear signal that corresponds in time with the ionic current channel event.

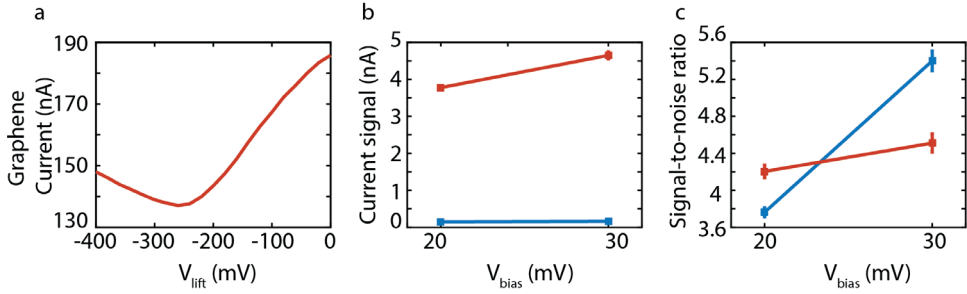


**Figure 6.12: Sensitivity of the graphene nanostructure.** (a)  $V_{lift}$  dependence of the graphene current measured at 15mV bias voltage and  $V_{ion}$  gate potential of +200mV. (b) Mean graphene current increase (red) and ionic current blockades (blue) due to DNA translocations in nanoamperes at two bias voltages ( $3.78 \pm 0.05$  nA (mean +- s.e.m.) at  $V_{bias} = 20$ mV and  $4.65 \pm 0.09$  nA (mean  $\pm$  s.e.m.) at  $V_{bias} = 30$ mV). The ionic current dips remain unchanged for the two different bias voltages. (c) Signal-to-noise ratio *versus* bias voltage.

### 6.5.1 CALCULATION OF THE GRAPHENE CAPACITANCE

When an electrolyte gate is used, two components of the capacitance have to be taken into account: the double layer capacitance, and the quantum capacitance<sup>57</sup>. Interestingly, the quantum capacitance of the graphene is the dominant component of the capacitance measured. The capacitance  $C_g$  can be modelled as two capacitances in series:  $\frac{1}{C_g} = \frac{1}{C_{dl}} + \frac{1}{C_q}$  with  $C_{dl}$  the double layer capacitance and  $C_q$  the quantum capacitance. The double layer capacitance is approximated by  $\epsilon_0 \epsilon / t$ , where  $\epsilon_0 = 8.85 \times 10^{-12}$  Fm<sup>-2</sup>,  $\epsilon = 78.4$  the dielectric constant of 1M KCl, and  $t \approx 0.3$ nm the thickness of the Debye screening length at 1M KCl, leading to  $C_{dl} \approx 2.3$  Fm<sup>-2</sup>. The quantum capacitance can be approximated by the simplified equation<sup>57</sup>:  $C_q \approx \frac{2e^2}{\hbar v_F \sqrt{\pi}} \sqrt{n}$ , with  $e$  the electron charge,  $v_F \approx c/300$  the Fermi velocity of the Dirac charge carriers, and  $n$  the carrier density, which we estimate to be  $n = 10^{12}$  cm<sup>-2</sup>. Filling in these numbers leads to  $C_q \approx 0.0275$  Fm<sup>-2</sup> and a total capacitance of  $C_g \approx 0.0272$  Fm<sup>-2</sup>. Figure 6.13a displays the capacitance *versus* radial surface area, presented in radial distance from the nanopore center.

Secondly, we can estimate the capacitance from the transconductance measurement<sup>58,59</sup>, using the relation:  $g_m = \frac{w}{L} \cdot C \cdot \mu \cdot V_{bias}$ , with  $g_m$  the measured transconductance,  $w$  the width of the nanostructure,  $L$  the length of the nanostructure,  $\mu$  the mobility, and  $V_{bias}$  the drain-source voltage. The mobility of the charge carriers is estimated to be<sup>60</sup>  $\mu \sim 100$  cm<sup>2</sup>V<sup>-1</sup>s<sup>-1</sup>. Filling in the numbers of the experiment:  $\frac{w}{L} \sim 1$ ,  $g_m = -0.25$ nA/mV,  $V_{ds} = 0.02$ V, leads to 1.25 mFm<sup>-2</sup>. The measured capacitances as a function of radial surface area, as extending from the nanopore center are presented in Fig. 6.14b.



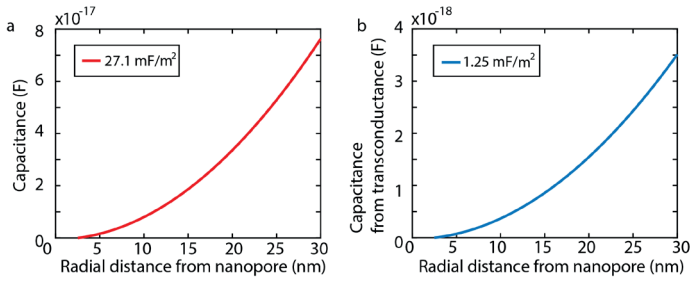


**Figure 6.13: Graphene capacitance as a function of radial distance from the nanopore.** (a) The graphene capacitance as theoretically approximated as function of the radial distance from the center of the nanopore. The surface area is modelled as a circular disk that extends from the center of the nanopore. (b) Capacitance as derived from the transconductance *versus* the same radial distance as in (a).

6

### 6.5.2 INTERPRETATION OF THE DIFFERENTIAL CURRENT SIGNALS

Both the electrostatic gating due to the negative charge of the DNA backbone and due to the potential change at the nanopore caused by the DNA translocation can induce an increase in current through  $I_g = g_m \Delta V$ . With the measured transconductance  $g_m = -0.25 \text{ nA/nV}$  at  $V_{bias} = 20 \text{ mV}$  (see fig. 6.5d main text) and the median of the graphene current signals of  $I_g = 3.8 \text{ nA}$  measured at  $V_{bias} = 20 \text{ mV}$ , we extract  $\Delta V \cong -15 \text{ mV}$ .

To examine whether this is a reasonable value for a direct charge measurement of the graphene, we consider the relation:  $\Delta V_Q = \frac{Q_{eff}}{C_g}$ . Where  $Q_{eff}$  is the effective charge of the DNA as probed by the graphene, and  $C_g$  the local capacitance between the graphene and the electrolyte. The effective charge of dsDNA was experimentally determined to be  $0.5 \pm 0.05 \text{ e/bp}$  in  $1 \text{ M KCl}$ <sup>51</sup>. Given that we measure on DNA plasmids (which will insert two double-stranded DNA molecules in parallel into the nanopore) and that the distance between two consecutive basepairs is approximately  $0.34 \text{ nm}$ , each vertical ‘slice’ of DNA contains an effective charge of approximately  $1e$ . The effective thickness of graphene nanopores was shown to be  $\sim 0.6 \text{ nm}$ <sup>10</sup>, which would host approximately two such DNA slices. We therefore estimate that the charge that is probed by the graphene is at maximum of order  $2e$ , or a fraction of that, as the DNA needs to be in close proximity to the graphene edge to be sensed within the very small Debye screening length of  $0.3 \text{ nm}$  at  $1 \text{ M KCl}$ . For a rough estimate for the graphene capacitance, we consider a ring with a width of  $1 \text{ nm}$  around the nanopore, which yields a capacitance of  $C_g \cong 5 \times 10^{-19} \text{ F}$  (section 6.10.1). Adopting this value for the capacitance and values for  $Q_{eff}$  ranging between  $0.1-2e$ , we obtain  $\Delta V_Q$  ranging between  $-30 \text{ mV}$  and  $-600 \text{ mV}$ . However, it must be noted that the capacitance derived from the transconductance measurement is one order of magnitude smaller than the above theoretical estimate, which would yield substantially larger  $\Delta V_Q$  values of  $-0.7 \text{ V}$  to  $-13.5 \text{ V}$ .

Furthermore, as reported before<sup>38,39</sup>, DNA translocation itself evokes a change in the potential at the nanopore. We used the analytical approximation<sup>38,40,42</sup>  $V(r) = \frac{d^2}{8lr} V_{ion}$ , with  $d$  the nanopore diameter,  $l$  the nanopore length, and  $r$  the distance from the center of the nanopore, to calculate the potentials at the nanopore with and without DNA, through  $\Delta V = V_{DNA}(r) - V_{no\ DNA}(r)$  (see Fig. 6.14). We find that the potential change at the nanopore edge is in the order of -50mV (see Fig. 6.14) for our experimental conditions ( $d \sim 5\text{nm}$ ,  $l \sim 5\text{nm}$  (i.e. the approximated thickness of the h-BN flake),  $V_{ion} = 300\text{mV}$ , and a DNA plasmid as analyte). This approximation, however, does not take surface charges into account and should therefore be considered as an upper limit<sup>38</sup>. We conclude that the measured  $\Delta V$  is consistent with contributions of both the direct charge coupling of the DNA and in a local potential change at the nanopore.

6

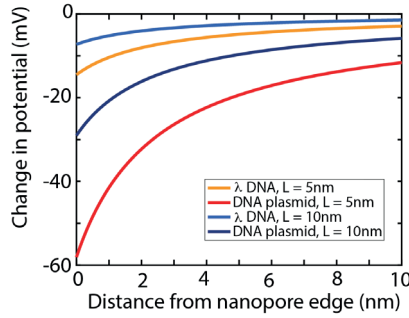


**Figure 6.14: Estimation of the potential change as a function of distance from the nanopore edge during DNA translocation.** An analytical expression (derived in Ref. <sup>38,40,42</sup>) was used to estimate the potential change due to DNA translocation. A transmembrane potential of 300mV was used. It is clear from the graph that a larger potential change emerges for thinner pores and for DNA plasmids (where the amount of DNA that resides in the pore is doubled). It must be noted that this expression does not take surface charges into account, which was shown to lead to a higher estimation of the potential changes<sup>38</sup>. In the DNA measurements, we used homogeneous buffer salt conditions (1M KCl), a nanopore diameter of 5nm, a pore length of 5nm, and we translocated DNA plasmids. The red curve in the graph corresponds best to our conditions.

### 6.5.3 INTERPRETATION OF THE COMMON MODE SIGNALS

In a small subset of the events (3.5%) we measured  $\sim 100 \mu V$  signals in the common mode channel, which correspond to  $\sim 20\text{pA}$  transient capacitive currents. This subset of events shows a larger mean current signal in the differential graphene channel and a larger mean translocation time. If these responses were to solely induced through the tiny graphene nanoribbon capacitance, it would indicate extremely large voltage fluctuations at the pore ( $\frac{\Delta V}{\Delta t} \approx \frac{I_c}{C_g} \approx \frac{10 \times 10^{-12}}{8 \times 10^{-18}} \approx 1.25 \times 10^6 \text{ V/s}$ ), which is an unreasonable value. Here we assumed a circular area with radius of 10nm extending from the pore center to calculate a capacitance of:  $C_g \approx 8 \times 10^{-18} \text{ F}$  (see Fig. 6.13a), as this is the radial distance at which most of the potential change is probed (see Fig. 6.14). This indicates that these common mode signals rather relate to non-local interactions during the DNA translocations.

The capacitance of the active area exposed to liquid was measured to be in the order of 20pF, which would relate to  $\frac{\Delta V}{\Delta t} \approx \frac{I_c}{C_g} \approx \frac{10 \times 10^{-12}}{20 \times 10^{-12}} \approx 0.5 \text{V/s} \approx 500 \mu\text{V/ms}$  which appears more reasonable.

In Figure 6.15, we simulate the graphene nanoribbon as a transistor and measure its response to a 10mV voltage step in the differential channel. In the simulation, the common mode channel does not pick up any signal, unless two 10pF capacitances are added next to the graphene nanoribbon (see C1 and C2 in scheme), to lead to a response of  $\sim 100 \mu\text{V}$ . Thus, the 1.5% events that are visible in the common mode channel likely relate to non-local  $\Delta V_{nl}$  interactions to the capacitances of the leads ( $C_{lead}$ ).

6

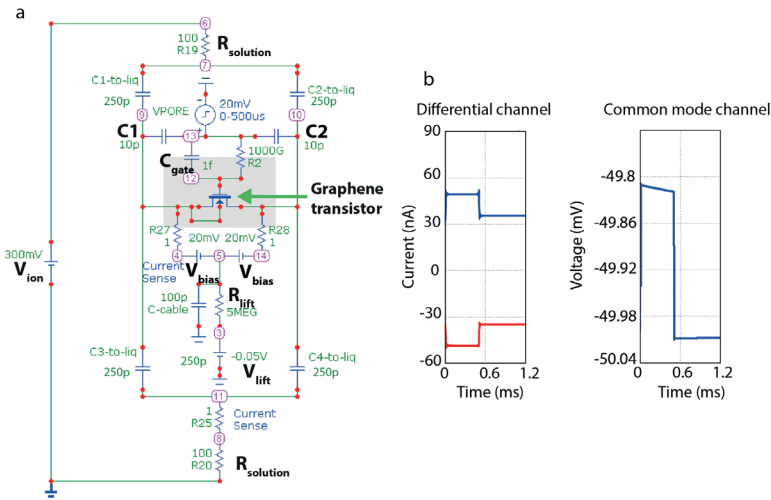


**Figure 6.15: SPICE simulation after addition of extra capacitance at the nanopore.** (a) Same circuit as in figure 6.7, but now with the addition of two 10pF capacitances at the nanopore (C1 and C2). A potential modulation is simulated by a 500  $\mu\text{s}$  pulse of 20mV. The graphene nanostructure functionality is simulated by a transistor. The  $V_{lift}$  potential is set at -50mV. (b) The current in the graphene as a result of the voltage pulse is measured in R27 (blue) and in R28 (red). The common mode readout is probed in node 5, between the  $V_{bias}$  batteries in the circuit in (a). A response of 200 $\mu\text{V}$  is measured. Without presence of the C1 and C2, such as in the circuit in figure 6.7, there would be no signature in the common mode measurement, due to the tiny capacitance at the nanopore.

PROBING DNA TRANSLOCATIONS WITH INPLANE CURRENT SIGNALS IN A GRAPHENE NANORIBBON WITH A NANOPORE

---

	$g_m$ (nA/mV)	$V_{ift}$		<b>G</b>	<b><math>\Delta G</math></b>	$I_{rms}$ (nA)	$V_{bias}$ (mV)	<b>SNR</b>	$V_{bias}$ (mV)
Sample A (Fig. 6.5)	-0.25  $V_{bias} = 20mV$	0 mV	Ionic	4 nS	$0.46 \pm 0.2nS$	0.04 0.03	20 30	3.8 5.4	20 30
			Graphene	15 $\mu S$	$0.16 \pm 0.08\mu S$	1.0 1.0	20 30	4.2 4.5	20 30
Sample B	-0.20 +0.13  $V_{bias} = 30mV$	0 mV  -350mV	Ionic	10 nS	$1.8 \pm 0.5nS$	0.05 0.06 0.09 0.10 0.12	10 25 30 50 75	10.5 5.1 4.9 4.3 5.4	10 25 30 50 75
			Graphene	10 $\mu S$	N/A	0.8 2.8 2.3 3.7 5.7	10 25 30 50 75	N/A	

**Table 6.1:** Comparison of transconductances, noise levels, and signals in two samples that yielded ionic signals.

6

## REFERENCES

1. Kasianowicz, J. J., Brandin, E., Branton, D. & Deamer, D. W. Characterization of individual polynucleotide molecules using a membrane channel. *Proc. Natl. Acad. Sci.* **93**, 13770–13773 (1996).
2. Bayley, H. Nanopore Sequencing: From Imagination to Reality. *Clin. Chem.* **61**, 25–31 (2015).
3. Jain, M., Olsen, H. E., Paten, B. & Akeson, M. The Oxford Nanopore MinION: delivery of nanopore sequencing to the genomics community. *Genome Biol.* **17**, 239 (2016).
4. Jain, M. *et al.* Nanopore sequencing and assembly of a human genome with ultra-long reads. *bioRxiv* 128835 (2017).
5. Li, J. *et al.* Ion-beam sculpting at nanometre length scales. *Nature* **412**, 166–169 (2001).
6. Dekker, C. Solid-state nanopores. *Nat. Nanotechnol.* **2**, 209–15 (2007).
7. Miles, B. N. *et al.* Single molecule sensing with solid-state nanopores: novel materials, methods, and applications. *Chem. Soc. Rev. Chem. Soc. Rev* **42**, 306–12 (2013).
8. Squires, A. H., Gilboa, T., Torfstein, C., Varongchayakul, N. & Meller, A. Single-Molecule Characterization of DNA–Protein Interactions Using Nanopore Biosensors. *Methods Enzymol.* **582**, 353–385 (2017).
9. Schneider, G. F. *et al.* DNA translocation through graphene nanopores. *Nano Lett.* **10**, 3163–7 (2010).
10. Garaj, S. *et al.* Graphene as a subnanometre trans-electrode membrane. *Nature* **467**, 190–3 (2010).
11. Merchant, C. A. *et al.* DNA translocation through graphene nanopores. *Nano Lett.* **10**, 2915–21 (2010).
12. Venkatesan, B. M. *et al.* Stacked graphene-Al<sub>2</sub>O<sub>3</sub> nanopore sensors for sensitive detection of DNA and DNA-protein complexes. *ACS Nano* **6**, 441–50 (2012).
13. Banerjee, S. *et al.* Electrochemistry at the edge of a single graphene layer in a nanopore. *ACS Nano* **7**, 834–43 (2013).
14. Schneider, G. F. *et al.* Tailoring the hydrophobicity of graphene for its use as nanopores for DNA translocation. *Nat. Commun.* **4**, 2619 (2013).
15. Garaj, S., Liu, S., Golovchenko, J. A. & Branton, D. Molecule-hugging graphene nanopores. *Proc. Natl. Acad. Sci. U. S. A.* **110**, 12192–6 (2013).
16. Banerjee, S. *et al.* Slowing DNA Transport Using Graphene-DNA Interactions. *Adv. Funct. Mater.* **25**, 936–946 (2014).
17. Liu, S. *et al.* Boron Nitride Nanopores: Highly Sensitive DNA Single-Molecule Detectors. *Adv. Mater.* **25**, 4549–4554 (2013).

18. Feng, J. *et al.* Identification of single nucleotides in MoS<sub>2</sub> nanopores. *Nat. Nanotechnol.* **10**, 1070–1076 (2015).
19. Danda, G. *et al.* Monolayer WS<sub>2</sub> Nanopores for DNA Translocation with Light-Adjustable Sizes. *ACS Nano* **11**, 1937–1945 (2017).
20. Liu, K. *et al.* Geometrical Effect in 2D Nanopores. *Nano Lett.* **17**, 4223–4230 (2017).
21. Heerema, S. J. *et al.* 1/f noise in graphene nanopores. *Nanotechnology* **26**, (2015).
22. Wallace, P. The Band Theory of Graphite. *Phys. Rev.* **71**, 622–634 (1947).
23. Nelson, T., Zhang, B. & Prezhdoo, O. V. Detection of nucleic acids with graphene nanopores: ab initio characterization of a novel sequencing device. *Nano Lett.* **10**, 3237–42 (2010).
24. Ouyang, F.-P., Peng, S.-L., Zhang, H., Weng, L.-B. & Xu, H. A biosensor based on graphene nanoribbon with nanopores: a first-principles devices-design. *Chinese Phys. B* **20**, 58504 (2011).
25. Saha, K. K., Drndić, M. & Nikolić, B. K. DNA base-specific modulation of microampere transverse edge currents through a metallic graphene nanoribbon with a nanopore. *Nano Lett.* **12**, 50–5 (2012).
26. Avdoshenko, S. M. *et al.* Dynamic and electronic transport properties of DNA translocation through graphene nanopores. *Nano Lett.* **13**, 1969–76 (2013).
27. Girdhar, A., Sathe, C., Schulten, K. & Leburton, J.-P. Graphene quantum point contact transistor for DNA sensing. *Proc. Natl. Acad. Sci. U. S. A.* **110**, 16748–53 (2013).
28. Ahmed, T., Haraldsen, J. T., Zhu, J.-X. & Balatsky, A. V. Next-Generation Epigenetic Detection Technique: Identifying Methylated Cytosine Using Graphene Nanopore. *J. Phys. Chem. Lett.* **5**, 2601–2607 (2014).
29. Sadeghi, H. *et al.* Graphene sculpture nanopores for DNA nucleobase sensing. *J. Phys. Chem. B* **118**, 6908–14 (2014).
30. Ahmed, T. *et al.* Correlation dynamics and enhanced signals for the identification of serial biomolecules and DNA bases. *Nanotechnology* **25**, 125705 (2014).
31. Paulechka, E., Wassenaar, T. A., Kroenlein, K., Kazakov, A. & Smolyanitsky, A. Nucleobase-functionalized graphene nanoribbons for accurate high-speed DNA sequencing. *Nanoscale* **8**, 1861–1867 (2016).
32. Pedersen, J. N., Boynton, P., Ventra, M. Di, Jauho, A.-P. & Flyvbjerg, H. Classification of DNA nucleotides with transverse tunneling currents. *Nanotechnology* **28**, 15502 (2017).
33. Sarathy, A., Qiu, H. & Leburton, J.-P. Graphene Nanopores for Electronic Recognition of DNA Methylation. *J. Phys. Chem. B* **121**, 3757–3763 (2017).
34. De Souza, F. A. L., Amorim, R. G., Scopel, W. L. & Scheicher, R. H. Electrical detection of nucleotides via nanopores in a hybrid graphene/h-BN sheet. *Nanoscale*

**9**, (2017).

35. Han, S.-J. *et al.* High-Frequency Graphene Voltage Amplifier. (2011).
36. Petrone, N., Meric, I., Hone, J. & Shepard, K. L. Graphene Field-Effect Transistors with Gigahertz-Frequency Power Gain on Flexible Substrates. (2012).
37. Traversi, F. *et al.* Detecting the translocation of DNA through a nanopore using graphene nanoribbons. *Nat. Nanotechnol.* **8**, 939–45 (2013).
38. Puster, M. *et al.* Cross-Talk Between Ionic and Nanoribbon Current Signals in Graphene Nanoribbon-Nanopore Sensors for Single-Molecule Detection. *Small* **11**, 6309–6316 (2015).
39. Xie, P., Xiong, Q., Fang, Y., Qing, Q. & Lieber, C. M. Local electrical potential detection of DNA by nanowire-nanopore sensors. *Nat. Nanotechnol.* **7**, 119–25 (2012).
40. Wanunu, M., Morrison, W., Rabin, Y., Grosberg, A. Y. & Meller, A. Electrostatic focusing of unlabelled DNA into nanoscale pores using a salt gradient. *Nat. Nanotechnol.* **5**, 160–165 (2010).
41. Parkin, W. M. & Drndic, M. Signal and noise in FET-nanopore devices. *ACS Sensors* (2018). doi:10.1021/acssensors.7b00708
42. Grosberg, A. Y. & Rabin, Y. DNA capture into a nanopore: Interplay of diffusion and electrohydrodynamics. *J. Chem. Phys.* **133**, (2010).
43. Stampfer, C. *et al.* Energy Gaps in Etched Graphene Nanoribbons. *Phys. Rev. Lett.* **102**, 56403 (2009).
44. Todd, K., Chou, H.-T., Amasha, S. & Goldhaber-Gordon, D. Quantum Dot Behavior in Graphene Nanoconstrictions. *Nano Lett.* **9**, 416–421 (2009).
45. Neklyudova, M. *et al.* Through-membrane electron-beam lithography for ultrathin membrane applications. *Appl. Phys. Lett.* **111**, (2017).
46. Xu, Q. *et al.* Controllable atomic scale patterning of freestanding monolayer graphene at elevated temperature. *ACS Nano* **7**, 1566–72 (2013).
47. Song, B. *et al.* Atomic-scale electron-beam sculpting of near-defect-free graphene nanostructures. *Nano Lett.* **11**, 2247–50 (2011).
48. Novoselov, K. S. *et al.* Two-dimensional gas of massless Dirac fermions in graphene. *Nature* **438**, 197–200 (2005).
49. Han, M., Özyilmaz, B., Zhang, Y. & Kim, P. Energy Band-Gap Engineering of Graphene Nanoribbons. *Phys. Rev. Lett.* **98**, 206805 (2007).
50. Rodríguez-Manzo, J. A. *et al.* *In Situ* Transmission Electron Microscopy Modulation of Transport in Graphene Nanoribbons. *ACS Nano* **10**, 4004–4010 (2016).
51. Keyser, U. F. *et al.* Direct force measurements on DNA in a solid-state nanopore. *Nat. Phys.* **2**, 473–477 (2006).
52. Nanda, G. *et al.* Electronic transport in helium-ion-beam etched encapsulated graphene nanoribbons. *Carbon N. Y.* **119**, 419–425 (2017).

53. Schneider, G. F., Calado, V. E., Zandbergen, H., Vandersypen, L. M. K. & Dekker, C. Wedging transfer of nanostructures. *Nano Lett.* **10**, 1912–6 (2010).
54. Dean, C. R. *et al.* Boron nitride substrates for high-quality graphene electronics. *Nat. Nanotechnol.* **5**, 722–726 (2010).
55. Qi, Z. J. *et al.* Electronic transport of recrystallized freestanding graphene nanoribbons. *ACS Nano* **9**, 3510–20 (2015).
56. Plesa, C. & Dekker, C. Data analysis methods for solid-state nanopores. *Nanotechnology* **26**, 84003 (2015).
57. Xia, J., Chen, F., Li, J. & Tao, N. Measurement of the quantum capacitance of graphene. *Nat Nanotechnol* **4**, 505–509 (2009).
58. Schwierz, F. Graphene transistors. *Nat. Nanotechnol.* **5**, 487 (2010).
59. Kireev, D. *et al.* Graphene transistors for interfacing with cells: towards a deeper understanding of liquid gating and sensitivity. *Sci. Rep.* **7**, 6658 (2017).
60. Schwierz, F. Graphene Transistors: Status, Prospects, and Problems. *Proc. IEEE* **101**, 1567–1584 (2013).





# 7

## CONCLUSIONS AND RECOMMENDATIONS

This thesis describes the work that is done to probe the potential of using nanopores in graphene membranes and nanoribbons for a future DNA sequencing technology. The theoretical studies performed in the field, as described in chapter 2, are generally very optimistic and hence promising. Experimentally, however, we are still far away from this goal. It showed to be extremely difficult to obtain DNA signals in the inplane current of a graphene nanoribbon, mainly due to the involved material science, the many lithography steps, and nanopore wetting issues. Although we were the first to explicitly show DNA-induced gating of a graphene nanoribbon with a nanopore, we have not been able to characterize the signals and signal-to-noise ratios in detail. The recommendations listed in this chapter may help to guide future scientists to further identify and improve signals in the inplane currents of graphene or other 2D material nanostructures.

## 7.1 GENERAL CHALLENGES FOR NANOPORE MEASUREMENTS BASED ON ELECTROPHORETIC FORCE

7 | One of the powerful aspects of the nanopore approach is the fact that the DNA is pulled towards and along the sensor like a string through the eye of a needle. Even though the principle is elegant, it does come with certain issues. The combination of forces causes the DNA to move stochastically and, in case of solid-state nanopores, extremely fast. The stochasticity in the translocation velocity is represented by the typically wide distributions of translocation times. These velocity fluctuations hamper the measurements, as it complicates the correlation between temporal signals and spatial information encoded in the DNA molecule. Secondly, spatial fluctuations caused by DNA motions with respect to the nanopore plane, can lead to overlapping signal distributions rather than distinct signal levels for each base. To limit these fluctuations, the size of the nanopores should ideally correspond to the width of the DNA. Thirdly, the fast translocation speed is often seen as a virtue, as it enables fast sequencing. However, it sets the demand for sampling frequencies above 5MHz. At such high frequencies, noise originating from the coupling between the feedback resistance in the amplifier and the capacitances from the nanopore membrane and instrumentation dominates, and makes it very challenging to resolve the tiny current changes in the ionic current<sup>1,2</sup>. Longer translocation times would therefore greatly ease the development of solid-state nanopore sequencing based on the ionic current readout. To summarize, a major challenge in the development of solid-state nanopore sequencer is to control the movement of the DNA molecules through the nanopore. It remains to be seen whether this can be done through the docking of a polymerase<sup>3-5</sup>, as is done with biological nanopores, by attaching functional groups at the nanopore that slow down and guide the DNA through the nanopore<sup>6,7</sup>, or by using plasmonic nanopores<sup>8</sup> and double pores<sup>9</sup>.

Other experimental challenges that are generally underestimated, involve the lack of wetting due to graphene's hydrophobicity and clogging of the nanopore by DNA due to hydrophobic interactions. Not seldomly, it appeared to be impossible to obtain clear DNA signals during graphene nanopore experiments, even after linear current-voltage behavior was observed for the ionic currents, which is possibly related to graphene's hydrophobicity. The use of hydrophilic coatings can improve wetting and prevent clogging of graphene nanopores, for instance by a coating of amino-pyrene-PEG<sup>10</sup>. During the work performed in this project, it appeared difficult to get this working reproducibly, however. Although solid-state pores are claimed to be robust, the nanopores often grow in size over time during measurements, and pores can typically be used for only 1-2 hours. These experimental difficulties certainly need to be studied, in order to realize DNA sequencing based on solid-state nanopores.

## 7.2 CONSIDERATIONS FOR GRAPHENE NANORIBBON INPLANE CURRENT MEASUREMENTS

In chapter 6 of this thesis, we made a distinction between the different signals that can be measured in the inplane current of a nanoribbon when a DNA molecule translocates through a nanopore in that ribbon. This section makes a few additional comments on the expected signal-to-noise ratios in the graphene current, discusses a few considerations for the device layout, and presents an overview of the different fabrication strategies used in this project.

### 7.2.1 SIGNAL-TO-NOISE IN THE TRANSVERSE CURRENT – WHERE IT ALL STARTED

A major putative advantage of the inplane current readout, as frequently stated, is the benefit of larger current magnitudes that enable high bandwidth measurements. Indeed, a lower resistance corresponds to shorter relaxation times in the circuit. However, it is relevant to assess the signal-to-noise ratio at the high bandwidths needed to resolve base information at the translocation speeds measured in graphene nanopores.

The intrinsic noise in the inplane graphene current<sup>11</sup> is manifested by a frequency-independent thermal noise and shot noise, both arising from the random motions of charge carriers. Furthermore, frequency-dependent  $1/f$  noise and noise due to the generation and recombination of charge carriers ('generation-recombination noise') are present, which are both low-frequency noise phenomena.  $1/f$  noise is generally caused by charge carrier number fluctuations, mobility fluctuations or a combination of the two. Due to its  $1/f$  dependency, these noise contributions are not expected to be limiting at high frequencies.

In the high-frequency regime, other noise sources come into play. The vast majority of amplifiers used to measure small currents use negative voltage feedback op-amp circuits, due to their low noise. At high frequencies, noise is induced by the capacitances in the circuit, which are predominantly represented by the nanopore membrane capacitance, electronic wiring in the experimental setup, and amplifier input capacitances. Typically, in nanopore measurement setups, this capacitive noise becomes dominant at  $\sim 100$  kHz and higher frequencies, where it surpasses the thermal noise level, and scales with the square of the frequency<sup>12</sup> ( $f^2$ ). The capacitance of the graphene sensor is dominated by the capacitance between the gate and source/drain electrodes, due to their large surface area ( $C \propto \frac{A}{t}$ , with  $A$  is the area and  $t$  the thickness). Therefore, a thick insulating passivation layer on top of the leads is crucial to obtain low capacitance levels, down to  $\sim 0.01$ - $0.1$  pF, while the best nanopore membranes exhibit a capacitance of several pF<sup>2</sup>. Considering all other settings equal, i.e. the capacitances associated with the wiring and the amplifier input, for both the nanopore ionic current and the graphene inplane current, this 'capacitive noise' is expected to become dominant at higher frequencies than in the nanopore read-out. The

high-frequency response of the amplifier is also related to the capacitance between the gate and the source/drain electrodes, via<sup>13</sup>:  $\tau \approx \frac{C_{gd}}{g_m}$ , where  $g_m$  is the graphene transconductance. Response times of  $\sim 10$ - $100$ ns can be achieved, for a transconductance of  $1\mu\text{S}$  ( $1\text{nA/mV}$ ) and a total gate capacitance of  $0.01$ - $0.1\text{pF}$ .

What about the signals in the graphene current? As discussed in chapter 6, an electrostatic signal can be induced by a local potential modulation, either due to the volume constriction of the nanopore by DNA ( $\Delta V_I$ ), or due to the presence of the charged backbone of the DNA ( $\Delta V_Q$ ). This potential change is converted into a current change via the graphene's transconductance, which is a great asset in itself. For example, let's assume that the transconductance of the graphene nanostructure is  $1\mu\text{S}$  ( $1\text{nA/mV}$ ). The passage of a DNA molecule through the nanopore results in a typical ionic current blockade of  $1\text{nA}$ , an event that corresponds to a potential change of  $10\text{mV}$  at the nanopore, leading to a signal of  $10\text{nA}$  in the graphene current, i.e. a  $\sim 10$  times larger signal.

The circuit used in for the nanopore measurements described in chapter 6, contained a hardware low-pass RC filter to overcome crosstalk amongst the different channels in the DAQ, resulting in a maximum bandwidth of only  $10\text{kHz}$ . The power spectral density curves of recorded traces showed a  $1/f$  dependence up to this filter frequency. Within this bandwidth, the signal-to-noise ratios of the DNA events did not vary. Therefore, we do not have direct experimental evidence of how the  $S/N$  in the ionic and graphene channel compare at high frequencies.

To summarize, the signal-to-noise ratio in the inplane graphene nanoribbon current will likely be better than in the ionic current, particularly in the high frequency regime. 'Capacitive' noise is expected to become dominant at higher frequencies than in the ionic current measurement, due a lower overall input capacitance. Furthermore, electrostatic signals, based on a potential modulation  $\Delta V_I$  or exposed charge  $\Delta V_Q$ , are amplified due to the FET nature of the graphene, effectively yielding larger signals. However, based on our experiments, we cannot make any quantitative statements about high-frequency signal-to-noise levels and future studies are needed to explore this experimentally.

### 7.2.2 SOME CONSIDERATIONS FOR THE DEVICE LAYOUT

Due to the low density of states in graphene, the liquid acts as a highly effective gate that easily changes the Fermi level<sup>14</sup>. This also results in a fast response of the graphene to local and small potential changes, which is beneficial for fast DNA detection. If the graphene is not covered by an oxide layer or any other top-layer, the carbon atoms are in direct contact with the environment, allowing optimal interaction with local changes at the nanopore. Intuitively, it makes sense that for a direct charge measurement, or for a non-electrostatic

measurement where the presence of the DNA modifies the local density of states around the nanopores (as calculated in many of the theoretical studies, as described in chapter 2), it is best to expose the graphene directly to the liquid, at least locally near the nanopore.

What about the geometry of the nanopore? For the optimization of any type of signal one aims to measure, the diameter needs to approach the size of the DNA, as any modulation due to DNA will be extremely local, and will reduce strongly with distance. In addition, spatial fluctuations of the DNA inside the nanopore will be limited. In case of the local potential measurement and for capacitive coupling, the signals depend on the thickness of the nanopore membrane  $\Delta V_l \propto \frac{V_{ion}}{l \cdot d}$ , i.e. the thinner the membrane the larger the signal (see chapter 6). For the charge measurement, or non-electrostatic pore-DNA interactions, the membrane thickness is not relevant, implying that the graphene can rest on a thicker SiN or BN membrane.

Another point of attention, which is crucial for device performance, are the contact resistances of the graphene nanoribbon. Low contact resistances are not trivial. In this project they were obtained through current annealing. Due to the larger surface areas, CVD graphene generally provides better contacts. Secondly, as described above, the passivation of electrodes is important to suppress noise and to shorten the relaxation time of the graphene sensor. The passivation through polyimide, as described in chapter 6 has been useful, as it creates an insulating layer of 1.5  $\mu\text{m}$ .

### 7.2.3 NANOSCALE SIZE, DAMAGE, AND YIELD – A TRADE-OFF

To maximize the sensitivity of the graphene nanoribbon, the ribbon dimensions should be as small as possible, while aiming for high mobilities of the charge carriers. Graphene is well-known for the exceptionally high room-temperature carrier mobilities that are measured in large area graphene samples<sup>15</sup> (>100.000  $\text{cm}^2/\text{Vs}$ ). However, once patterned into a nanostructure, the mobilities are much lower, and range between<sup>16</sup> 100-1000  $\text{cm}^2/\text{Vs}$ . Defects induced during the patterning processes lead to these reduced mobilities<sup>17-19</sup>. In this section, the advantages and disadvantages of e-beam lithography, helium ion milling, TEM, and bottom-up ribbons are discussed, and summarized in Table 7.1.

As discussed in great detail in this thesis, the STEM approach yielded small well-defined nanostructures with nanopores, with relatively high conductivities. In principle, one could go down in size to 1-2nm, and sculpt along a certain crystal orientation, yielding purely zig-zag or armchair edges<sup>20</sup>, which determine the nanoribbon transport characteristics<sup>21,22</sup>. However, due to the complex multistep approach, the device yields were unacceptably low. Moreover, the STEM sculpting is done chip-by-chip, leading to hardly scalable protocols.

7 | A common approach to pattern graphene nanoribbons is through the combination of e-beam lithography and oxygen plasma etching. This method is highly scalable as patterning can be done on wafer-scale. However, the oxygen-plasma etching step induces damage that extends over tens of nanometers, which sets a limit to the minimum constriction width. Secondly, irregularities along the edges can result in a concatenation of quantum dots rather than a single nanoribbon<sup>17</sup>. Although smaller graphene structures can be obtained using e-beam, for nanoribbons with nanopores, ribbon widths of 50-100nm were reported<sup>23,24</sup>. The conductivities in graphene nanoribbons can be highly improved through graphene 'healing' by Joule heating<sup>25</sup>, as described in chapter 3 of this thesis. The combination of e-beam patterning and Joule heating can perhaps yield smaller nanoribbons with nanopores. The e-beam devices made during this project often yielded irregular or over-etched nanostructures. This was generally caused by polymer residues at the graphene constriction after e-beam exposure and resist development, covering areas that should be etched during the oxygen plasma etchings step. Secondly, the PMMA removal step in acetone, often resulted in the lift-off of the graphene nanostructures, which was solved by a top-layer of h-BN or through the use of negative resists such as HSQ.

Bottom-up ribbons synthesized by a chemical synthesis route are near-perfect ribbons<sup>26</sup>, with tiny widths of 1-2 nm, and generally much longer lengths (100's of nm). As the name suggest, these structures are chemically synthesized on substrates<sup>26</sup> (typically gold) or in solution<sup>27</sup>. We explored the possibility to use a nanopore next to a ~1nm wide ribbon, for the inplane current detection of DNA. The involved difficulty is to extract a single nanoribbon from a high density of ribbons in suspension, or from a gold surface, and to position it between two contacts. In order to do this, we tried electrostatic trapping<sup>28</sup> of nanoribbons suspended in tetrahydrofuran (THF), between two platinum electrodes at 50nm distance. In that trapping experiment, the graphene ribbons are polarized by an applied electric field and attracted to the position where the field is largest, i.e. in between the electrodes. We did not manage to get this protocol working, mainly due to nanoribbon aggregates in the suspensions. High-performance field effect transistors based on sub-nm bottom-up ribbons have been reported, showing high on-currents at room temperature<sup>29</sup> (1 $\mu$ A at 1V bias voltage). A protocol for bottom-up ribbons can, in principle, be scalable as they are synthesized in great numbers. However, the need to reproducibly obtain good contacts to single nanoribbons remains.

Last, an effort was made to fabricate nanostructures within stacked h-BN-graphene-h-BN nanoribbons using helium ion milling. Defect formation in the nanostructure can be limited due to the h-BN encapsulation<sup>30</sup>. The He-FIB has a small spot size and a relatively small scattering length<sup>31</sup>, and can be used for both imaging and patterning. To cut nanostructures in these graphene-BN stacks, a 10nm wide insulating barrier between the nanostructure and

the rest of the encapsulated graphene was made, yielding ribbon widths down to 25nm<sup>32</sup>. However, similar to what is found for e-beam ribbons, the beam induced damage in the ribbon edges results in transport that is governed by a series of quantum dots. Nanopores could be made in the same step as the nanostructure milling, which is a nice advantage, although the minimum pore size would be limited to 5nm. This method is scalable, because one is not limited to patterning one sample at the time.

	scalability	defect density	minimum size (nm)	handling difficulty
E-beam lithography	high	high	50	*
HIM	medium	high	25	*
STEM	low	low	1	***
Bottom-up	high	low	1	****

**Table 7.1:** Characteristics of the different graphene nanoribbon fabrication strategies employed in this research. The values are estimations, which are based on experiments and publised experimental results.

7

Fabrication of nanopores can be done in multiple ways. Scalable approaches to make nanopores in graphene are e-beam lithography followed by oxygen plasma etching (down to 16nm in diameter)<sup>33</sup>, or through the application of short high voltage pulses over a graphene membrane enclosed by reservoirs with ionic solutions (nanopores down to 1nm)<sup>34</sup>. The latter technique, however, does not provide means to predetermine the location of the nanopore. Until now, (S)TEM appears to remain the only way to controllably drill small nanopores in or at the edge of the graphene nanostructure, with low defect formation while retaining high conductivities<sup>35</sup>.

#### 7.2.4 WHAT ABOUT OTHER 2D MATERIALS?

In the past years, nanopores have been explored in other 2D materials, like h-BN<sup>36,37</sup>, MoS<sub>2</sub><sup>38-40</sup> and WS<sub>2</sub><sup>41</sup>. Single layers of these materials are just slightly thicker than graphene (e.g. ~0.65nm for MoS<sub>2</sub><sup>38</sup>) and high signal-to-noise ratios of the DNA translocation events through these membranes have been observed (>10). These materials are supposedly easier to wet<sup>36,38,39</sup>, and do not suffer from  $\pi$ -stacking interactions, which for graphene lead to nanopore clogging. Particularly for MoS<sub>2</sub>, a better wettability has been reported, which can be ascribed to the hydrophilic nature of the Mo atoms<sup>42</sup>.

The group of 2D transition metal dichalcogenides (TMDCs) (e.g. MoS<sub>2</sub>, WS<sub>2</sub>, and WSe<sub>2</sub>), are semiconducting materials, and could therefore be interesting for the inplane current detection of DNA when combined with a nanopore. Theoretical studies have presented calculations on the transmission response in a MoS<sub>2</sub> nanostructure due to DNA translocation or to DNA adsorption<sup>42,43</sup>, or to the passage of methylated DNA<sup>44</sup>. Measurable base-dependent bandgap changes in MoS<sub>2</sub> due to DNA adsorption have been predicted<sup>42</sup>.



Experimental work has mostly focused on a nanopore-integrated FET layout. Single-layer MoS<sub>2</sub> has a bandgap of 1.8eV<sup>45</sup>, with reported mobilities in the order of ~1 cm<sup>2</sup>/Vs, which can be increased to ~200 cm<sup>2</sup>/Vs through the use of a hafnium oxide topgate<sup>46</sup>. A general problem with 2D TMDCs, is the difficulty to obtain low contact resistances owing to their semiconducting nature, while this is vital for device performance. A common strategy to decrease the contact resistance in bulk semiconductors is to induce doping to the contact areas. In 2D materials, however, this would modify the material properties and is therefore not possible<sup>47</sup>. Secondly, the lack of dangling bonds on the surface makes it difficult to form bonds with the metal<sup>47</sup>. Recently, it was shown that metallic TMDCs can be used to contact semiconducting TMDCs, where the native chemical bonds allow easier charge transport leading to lower contact resistances<sup>48</sup>.

7 | Summing up, monolayer TMDCs are semiconducting 2D materials that can potentially be useful for a nanopore-integrated FET readout, where the main advantage will be the wettability of the nanopore. It can be challenging to achieve high carrier mobilities in the nanostructures needed to sense DNA, and to obtain low contact resistances. The nanopore experiment is expected to be much easier, which can enable DNA signal characterization in these FET systems.

### 7.3 OUTLOOK

In this thesis, we have shown that a graphene nanoribbon with a nanopore can be sensitive to translocating DNA molecules. Future studies will likely focus on nanopore-integrated graphene or TMDC-based FETs, and should show whether signal-to-noise ratios in these FET currents are higher, particularly in the high-frequency range. In pursuit of such devices, scalability should be addressed, in order to obtain reasonable device yields.

The recent successes with biological nanopores have somewhat tempered the optimism about the potential of solid-state nanopores. However, considering the developments on low-noise nanopore membranes<sup>1,49</sup>, low-noise amplifiers<sup>2</sup>, and the control of nanopore drilling in 2D membranes<sup>37</sup>, I believe that we have reasons to be optimistic, and that sequencing based on solid-state nanopores will come into being.

## REFERENCES

1. Balan, A. *et al.* Improving Signal-to-Noise Performance for DNA Translocation in Solid-State Nanopores at MHz Bandwidths. *Nano Lett.* **14**, 7215–7220 (2014).
2. Shekar, S. *et al.* Measurement of DNA translocation dynamics in a solid-state nanopore at 100 ns temporal resolution. *Nano Lett.* **16**, 4483–4489 (2016).
3. Hornblower, B. *et al.* Single-molecule analysis of DNA-protein complexes using nanopores. *Nat. Methods* **4**, 315–317 (2007).
4. Benner, S. *et al.* Sequence-specific detection of individual DNA polymerase complexes in real time using a nanopore. *Nat. Nanotechnol.* **2**, 718–724 (2007).
5. Cockroft, S. L., Chu, J., Amarin, M. & Ghadiri, M. R. A single-molecule nanopore device detects DNA polymerase activity with single-nucleotide resolution. *J. Am. Chem. Soc.* **130**, 818–820 (2008).
6. Ohshiro, T. & Umezawa, Y. Complementary base-pair-facilitated electron tunneling for electrically pinpointing complementary nucleobases. *Proc. Natl. Acad. Sci.* **103**, 10–14 (2006).
7. He, J., Lin, L., Zhang, P. & Lindsay, S. Identification of DNA basepairing via tunnel-current decay. *Nano Lett.* **7**, 3854–3858 (2007).
8. Belkin, M., Chao, S.-H., Jonsson, M. P., Dekker, C. & Aksimentiev, A. Plasmonic Nanopores for Trapping, Controlling Displacement, and Sequencing of DNA. *ACS Nano* **9**, 10598–10611 (2015).
9. Pud, S. *et al.* Mechanical Trapping of DNA in a Double-Nanopore System. *Nano Lett.* **16**, 8021–8028 (2016).
10. Schneider, G. F. *et al.* Tailoring the hydrophobicity of graphene for its use as nanopores for DNA translocation. *Nat. Commun.* **4**, 2619 (2013).
11. Balandin, A. A. Low-frequency  $1/f$  noise in graphene devices. *Nat. Nanotechnol.* **8**, 549–55 (2013).
12. Rosenstein, J. K. & Shepard, K. L. Temporal resolution of nanopore sensor recordings. *Conf. proceedings Annual Int. Conf. IEEE Eng. Med. Biol. Soc.* 4110–4113 (2013).
13. Parkin, W. M. & Drndic, M. Signal and noise in FET-nanopore devices. *ACS Sensors* (2018). doi:10.1021/acssensors.7b00708
14. Heller, I. *et al.* Individual single-walled carbon nanotubes as nanoelectrodes for electrochemistry. *Nano Lett.* **5**, 137–142 (2005).
15. Wang, L. *et al.* One-dimensional electrical contact to a two-dimensional material. *Science (80-. )*. **342**, 614–617 (2013).
16. Schwierz, F. Graphene Transistors: Status, Prospects, and Problems. *Proc. IEEE* **101**, 1567–1584 (2013).
17. Stampfer, C. *et al.* Energy Gaps in Etched Graphene Nanoribbons. *Phys. Rev. Lett.* **102**, 56403 (2009).

18. Haskins, J. *et al.* Control of thermal and electronic transport in defect-engineered graphene nanoribbons. *ACS Nano* **5**, 3779–3787 (2011).
19. Lherbier, A. *et al.* Transport properties of graphene containing structural defects. *Phys. Rev. B* **86**, 75402 (2012).
20. Xu, Q. *et al.* Controllable atomic scale patterning of freestanding monolayer graphene at elevated temperature. *ACS Nano* **7**, 1566–72 (2013).
21. Fujita, M., Wakabayashi, K., Nakada, K. & Kusakabe, K. Peculiar Localized State at Zigzag Graphite Edge. *J. Phys. Soc. Japan* **65**, 1920–1923 (1996).
22. Nakada, K., Fujita, M., Dresselhaus, G. & Dresselhaus, M. Edge state in graphene ribbons: Nanometer size effect and edge shape dependence. *Phys. Rev. B* **54**, 17954–17961 (1996).
23. Traversi, F. *et al.* Detecting the translocation of DNA through a nanopore using graphene nanoribbons. *Nat. Nanotechnol.* **8**, 939–45 (2013).
24. Puster, M. *et al.* Cross-Talk Between Ionic and Nanoribbon Current Signals in Graphene Nanoribbon-Nanopore Sensors for Single-Molecule Detection. *Small* **11**, 6309–6316 (2015).
25. Qi, Z. J. *et al.* Electronic transport of recrystallized freestanding graphene nanoribbons. *ACS Nano* **9**, 3510–20 (2015).
26. Cai, J. *et al.* Atomically precise bottom-up fabrication of graphene nanoribbons. *Nature* **466**, 470–3 (2010).
27. Narita, A. *et al.* Synthesis of structurally well-defined and liquid-phase-processable graphene nanoribbons. *Nat. Chem.* **6**, 126–132 (2014).
28. Bezryadin, A., Dekker, C. & Schmid, G. Electrostatic trapping of single conducting nanoparticles between nanoelectrodes. *Appl. Phys. Lett.* **71**, 1273–1275 (1997).
29. Llinas, J. P. *et al.* Short-channel field-effect transistors with 9-atom and 13-atom wide graphene nanoribbons. *Nat. Commun.* **8**, (2017).
30. Nanda, G., Goswami, S., Watanabe, K., Taniguchi, T. & Alkemade, P. F. A. Defect Control and n-Doping of Encapsulated Graphene by Helium-Ion-Beam Irradiation. *Nano Lett.* **15**, 4006–4012 (2015).
31. Li, W.-D., Wu, W. & Stanley Williams, R. Combined helium ion beam and nanoimprint lithography attains 4 nm half-pitch dense patterns. *J. Vac. Sci. Technol. B, Nanotechnol. Microelectron. Mater. Process. Meas. Phenom.* **30**, 06F304 (2012).
32. Nanda, G. *et al.* Electronic transport in helium-ion-beam etched encapsulated graphene nanoribbons. *Carbon N. Y.* **119**, 419–425 (2017).
33. Verschueren, D. V, Yang, W. & Dekker, C. Lithography-based fabrication of nanopore arrays in freestanding SiN and graphene membranes. *Nanotechnology* **29**, 145302 (2018).
34. Kuan, A. T., Lu, B., Xie, P., Szalay, T. & Golovchenko, J. A. Electrical pulse fabrication of graphene nanopores in electrolyte solution. *Appl. Phys. Lett.* **106**, (2015).

35. Puster, M., Rodríguez-Manzo, J. A., Balan, A. & Drndić, M. Toward sensitive graphene nanoribbon-nanopore devices by preventing electron beam-induced damage. *ACS Nano* **7**, 11283–9 (2013).
36. Zhou, Z. *et al.* DNA translocation through hydrophilic nanopore in hexagonal boron nitride. *Sci. Rep.* **3**, 3287 (2013).
37. Liu, K. *et al.* Geometrical Effect in 2D Nanopores. *Nano Lett.* **17**, 4223–4230 (2017).
38. Liu, K., Feng, J., Kis, A. & Radenovic, A. Atomically Thin Molybdenum Disulfide Nanopores with High Sensitivity for DNA Translocation. *ACS Nano* **8**, 2504–2511 (2014).
39. Feng, J. *et al.* Identification of single nucleotides in MoS<sub>2</sub> nanopores. *Nat. Nanotechnol.* **10**, 1070–1076 (2015).
40. Shim, J. *et al.* Detection of methylation on dsDNA using nanopores in a MoS<sub>2</sub> membrane. *Nanoscale* **9**, 14743–15162 (2017).
41. Danda, G. *et al.* Monolayer WS<sub>2</sub> Nanopores for DNA Translocation with Light-Adjustable Sizes. *ACS Nano* **11**, 1937–1945 (2017).
42. Farimani, A. B., Min, K. & Aluru, N. R. DNA Base Detection Using a Single-Layer MoS<sub>2</sub>. *ACS Nano* **8**, 7914–22 (2014).
43. Thomas, S., Rajan, A. C., Rezapour, M. R. & Kim, K. S. In search of a two-dimensional material for DNA sequencing. *J. Phys. Chem. C* **118**, 10855–10858 (2014).
44. Qiu, H., Sarathy, A., Schulten, K. & Leburton, J.-P. Detection and mapping of DNA methylation with 2D material nanopores. *npj 2D Mater. Appl.* **1**, 3 (2017).
45. Mak, K. F., Lee, C., Hone, J., Shan, J. & Heinz, T. F. Atomically thin MoS<sub>2</sub>: A new direct-gap semiconductor. *Phys. Rev. Lett.* **105**, (2010).
46. Radisavljevic, B., Radenovic, A., Brivio, J., Giacometti, V. & Kis, A. Single-layer MoS<sub>2</sub> transistors. *Nat. Nanotechnol.* **6**, 147–150 (2011).
47. Allain, A., Kang, J., Banerjee, K. & Kis, A. Electrical contacts to two-dimensional semiconductors. *Nature Materials* **14**, 1195–1205 (2015).
48. Nourbakhsh, A. *et al.* MoS<sub>2</sub> Field-Effect Transistor with Sub-10 nm Channel Length. *Nano Lett.* **16**, 7798–7806 (2016).
49. Lee, M.-H. *et al.* A Low-Noise Solid-State Nanopore Platform Based on a Highly Insulating Substrate. *Sci. Rep.* **4**, 7448 (2014).



# Summary

The information that can be extracted from DNA base sequences, is important for our understanding of biology, for insights in disease, and the way we practice medicine. The technology that one uses to determine DNA-base sequences is called 'DNA sequencing'. A portable device that enables fast and accurate sequencing, can potentially greatly improve the quality of healthcare. Nanopores in graphene have potential for a new DNA sequencing technology that is superior to the current solutions.

A nanopore is a nanometer-sized hole in a thin membrane. In nanopore experiments, a nanopore in a membrane, which is enclosed by two liquid chambers, forms the only passage for ions and molecules. When a potential is applied over the membrane, an ionic current emerges and molecules, like DNA, can translocate through the nanopore from one side to the other. The small current changes, caused by the blocking of the nanopore by the DNA molecule during translocation, can theoretically provide information about the different DNA bases due to their tiny volume differences. The membranes used for these experiments, are typically tens of nanometers thick, and therefore embrace many tens of DNA bases simultaneously (the distance between two consecutive bases along a ssDNA molecule is  $\sim 0.6\text{nm}$ ). Graphene is composed of a single layer of carbon atoms arranged in a two-dimensional hexagonal lattice. Due to its two-dimensional nature, graphene is ultimately thin, about  $\sim 0.34\text{nm}$ , and can therefore maximize the spatial resolution during nanopore experiments. The noise through graphene nanopores is, however, relatively high, which has made it impossible to resolve any base information, so far.

Theoretically, it was shown to be possible to sequence DNA by measuring the inplane current through a nanoribbon with a nanopore, while a DNA molecule traverses the nanopore through that nanoribbon. An important advantage of the approach, are the relatively large current magnitudes through these nanoribbons, which enables high bandwidth measurements. This thesis reports on the work that is done to experimentally explore whether DNA can be detected in the current through a graphene nanoribbon with a nanopore.

Graphene has many special properties, next to its single atom thickness, it is a very strong material, a good thermal conductor and a very good electrical conductor. After its characterization in 2004, many creative ideas were proposed to exploit the special characteristics of graphene to sequence DNA. In **chapter 2**, we review these concepts and discuss the

---

corresponding experimental efforts in the field. The efforts can be categorized in four different methods: DNA detection by ionic current measurements through graphene nanopores, tunnelling currents across graphene nanogaps, inplane currents through graphene nanoribbons, and the physisorption of DNA on graphene nanostructures. We discuss the challenges of the different approaches and present a perspective on the future of DNA sequencing using graphene.

Graphene nanostructures can be sensitive to environmental fluctuations, such as variations in gas molecules or biomolecules, a characteristic that is used in various graphene sensors. A general challenge in the fabrication of graphene nanostructures is to control the generation of damage in the graphene lattice, as structural defects can affect mechanical, chemical, electrical and optical properties. In **chapter 3**, we discuss what types of defects exist in graphene as well as their effect on the electronic transport in graphene. A number of experimental studies that are performed to study graphene damage and to recover the lattice through recrystallization are evaluated. Scanning transmission electron microscopy (STEM) provides a useful method to study lattice defects, as it enables to image the material's response to environmental changes, such as e-beam irradiation and local heating.

The sensitivity of DNA translocation measurements is determined by the signal-to-noise ratio. Ideally, the signal is maximized and the noise levels are minimized. However, the current through graphene nanopore currents expose relatively high noise levels, which is apparent particularly in the low-frequency regime, characterized by a  $1/f$  dependency. In **chapter 4** of this thesis, an in-depth study into the origin of this noise is presented. The  $1/f$  noise in the ionic currents through graphene nanopores is shown to be two orders of magnitude larger than the noise levels measured in SiN nanopores. The  $1/f$  noise dependence to various parameters, such as the nanopore size, the buffer salt concentration and pH level of the solution is examined. Surprisingly, the noise does not scale with the inverse of the number of charge carriers, a relation which was found to hold for the noise in SiN nanopores. The noise comparison between mono- and bilayer graphene samples and multilayer graphene and boron nitride samples shows that the  $1/f$  noise can be lowered by increasing the flake thickness of graphene or boron nitride. We propose that the increased noise levels are induced by mechanical fluctuations of the thin elastic 2-dimensional membranes.

The results from the noise study, as presented in chapter 4, yielded ways to reduce the noise in the graphene nanopore devices. The effect of membrane fluctuations on the noise, is expected to lower when the area of freestanding graphene is smaller. In the original devices, a micrometer sized hole was made in the silicon nitride membrane, over which graphene flakes were suspended. The chips contained relatively thick SiN membranes ( $\sim 600\text{nm}$ ), as

these embedded platinum electrodes to locally heat the graphene during STEM sculpting of nanoribbons and nanopores to prevent carbon deposition. The formation of a narrow ( $d \sim 100$  nm) access channel in such a ‘thick’ membrane would add a large channel resistance to the nanopore circuit. In **chapter 5**, a technique is presented to make thin (down to 20nm) membranes within the thicker SiN membranes (600nm) from the backside, while retaining the flat topside of the membrane. With the thin windows, it was possible to suspend smaller areas of freestanding graphene, which resulted in lower noise in the ionic currents through the nanopores in these graphene membranes.

The most important chapter in this thesis is **chapter 6**, which describes the work that is done to detect inplane current modulations in a graphene nanoribbon with a nanopore, next to the ionic current readout, during DNA translocation events. High-temperature STEM is used to fabricate graphene nanoribbons and nanopores of the smallest scale with high electrical conductivity. With a home-built differential current amplifier, it is shown that resistive modulations in the graphene current that originate from DNA-graphene interactions can be decoupled from parasitic capacitive currents, which are inherent to the measurement. The multi-step device fabrication procedure enabled the fabrication of small and conductive nanostructures, but the lack of scalability resulted in a very low throughput of measurement devices. We show that DNA sensing with graphene nanoribbons with nanopores is challenging, but possible.

In **chapter 7**, the various virtues and issues of graphene are shortly emphasized and the challenges for the inplane current readout are considered. The advantages and disadvantages of different fabrication procedures are briefly discussed and the opportunities for other two-dimensional materials are addressed. With the knowledge that is gained over the years, I present a personal view on the challenges that lie ahead for the use of graphene in nanopore sequencing.





# Samenvatting

De informatie die uit DNA-base sequenties wordt gehaald, is van groot belang voor onze kennis in de biologie, voor inzichten in ziekten en biedt mogelijkheden om ziekten beter te behandelen. De methode die gebruikt wordt om DNA-base sequenties te bepalen heet 'DNA sequencing'. Huidige technologieën zijn relatief duur, traag en onnauwkeurig. Een handzaam apparaat, dat sneller, nauwkeuriger en goedkoper kan meten, kan de gezondheidszorg ingrijpend veranderen. Zo'n apparaat kan worden gebaseerd op de technologie van nanoporiën in grafeen en heeft de potentie de basis te vormen voor de nieuwe generatie DNA sequencing methodes.

Een nanoporie is een gaatje van enkele nanometers in een dun membraan. In een nanopore experiment, vormt een nanoporie in een membraan, dat aan beide zijden wordt omsloten door twee vloeistofkamers, de enige doorgang voor ionen en moleculen. Wanneer een potentiaalverschil over het membraan wordt aangebracht, ontstaat er een ionenstroom en kunnen moleculen zoals DNA van de ene zijde naar de andere zijde bewegen ('transloceren'). De kleine stroomverschillen die gemeten worden tijdens deze translocatie, bieden informatie over de verschillende DNA basen. De membranen die voor deze experimenten gebruikt worden, zijn typisch tientallen nanometers dik, en omsluiten daardoor honderden DNA basen tegelijk. Grafeen is opgebouwd uit een enkele laag koolstofatomen in een tweedimensionaal hexagonaal rooster. Door de tweedimensionale structuur, heeft grafeen een dikte van een enkel atoom, zo'n 0.34 nm, wat overeenkomt met de afstand tussen twee basen op een DNA molecuul (~0.5 nm). Dit uitiem dunne materiaal is theoretisch erg geschikt als membraan. Door die dikte kan de resolutie van de meting aan DNA worden gemaximaliseerd. Helaas is de ruis in de ionenstroom door grafeen nanoporiën erg hoog, daardoor is het tot op heden niet mogelijk met deze meting informatie over de DNA basen in kaart te brengen.

Theoretisch is er een meting mogelijk met een beter signaal/ruis niveau. In dat geval meet men de stroom door een grafeen nanolint, een smalle grafeen strook van enkele tientallen nanometers breed en lang, met in het midden een nanoporie. Aan de hand van modulaties in de stroom door een dergelijk gevoelig grafeenlint zou men de afzonderlijke DNA basen kunnen onderscheiden, wanneer een DNA molecuul door de nanoporie beweegt. Een belangrijk voordeel van deze detectiemethode is de relatief grote stroom die door deze grafeen nanolinten gaat, waardoor mogelijk bij hoge bandbreedte gemeten kan worden. Dit

---

proefschrift beschrijft het werk dat is gedaan om experimenteel te bepalen of het mogelijk is DNA base sequenties te meten in de stroom door grafeen nanolinten met nanoporiën.

Grafeen is een materiaal met bijzondere eigenschappen. Naast dat het de dikte heeft van een enkel koolstofatoom, is het extreem sterk, een goede thermische geleider en een erg goede elektrische geleider. Na de isolatie en karakterisatie van grafeen in 2004, zijn veel creatieve ideeën opgebracht om de bijzondere eigenschappen te benutten voor een nieuwe DNA sequencing technologie. In **hoofdstuk 2** van dit proefschrift, worden de verschillende concepten beschreven en het uitgevoerde experimentele werk geëvalueerd. Samengevat betreft het vier verschillende methoden: het meten aan DNA moleculen met variaties in ionenstromen door nanoporiën in grafeen membranen, met tunnelstromen over grafeen nanogaten, met elektrische stromen door grafeen nanolinten en metingen aan DNA adsorptie op grafeen nanostructuren. De verschillende mogelijkheden en uitdagingen van de verschillende strategieën worden besproken. Hoofdstuk 2 wordt afgesloten met een toekomstperspectief over het gebruik van grafeen voor een toekomstige DNA sequencing technologie.

Nanostructuren in grafeen kunnen gevoelig zijn voor omgevingsfluctuaties, zoals variaties in gasmoleculen of biologische moleculen, waardoor ze een basis vormen voor verschillende typen sensoren. Een algemene uitdaging voor het fabriceren van nanostructuren van grafeen, is om de beschadiging aan het materiaal te controleren. Deze beschadigingen in het rooster kunnen de mechanische, chemische, elektrische en optische eigenschappen van het grafeen beïnvloeden. In **hoofdstuk 3**, worden verschillende typen roosterdefecten en hun effect op het elektrisch transport besproken. Er wordt een overzicht gegeven van de experimentele studies die gedaan zijn om materiaalbeschadigingen te bestuderen en door middel van rekristallisatie te herstellen. Scanning tunnelling electron microscopy (STEM) biedt een geschikte methode om roosterdefecten te bestuderen. STEM maakt het namelijk mogelijk de respons weer te geven van het materiaal op omgevingsfluctuaties, zoals elektronenbundel irradiatie en verhitting.

Voor een optimale DNA-nanoporie meting wordt gestreefd naar een maximaal signaal en een minimale ruis. Helaas vertoont de ionenstroom door grafeen nanoporiën relatief veel ruis. Die manifesteert zich met name in het laagfrequente regime, gekarakteriseerd door een  $1/f$  afhankelijkheid. In **hoofdstuk 4** van dit proefschrift wordt een onderzoek naar de oorzaak van deze ruis gepresenteerd. De ruis in de ionenstromen door grafeen is gemiddeld twee orden hoger dan in conventionele silicium nitride nanoporiën. Een onderdeel van de studie is de relatie van de ruis tot verschillende parameters, zoals de nanoporie grootte, de zoutconcentratie en de pH-waarde van de zoutoplossing. Geconcludeerd wordt dat de ruis zich niet verhoudt tot de inverse van het aantal ladingsdragers. Dat is onverwacht,

omdat die inverse relatie in een eerdere ruisstudie aan nanopore ionenstromen wel werd gevonden. De vergelijking van de ruis van nanoporiën in enkellaags grafeen, multilaags grafeen en boron nitride (h-BN), laat zien dat de ruis kleiner wordt met een toenemende dikte van het materiaal. Grafeen en andere tweedimensionale materialen, zoals h-BN, zijn erg flexibel, terwijl multilagen zich eerder als een plaat gedragen. Een mogelijke oorzaak van hogere ruis wordt daarom toegeschreven mechanische fluctuaties van het flexibele enkellaags grafeen membraan.

De conclusies van de ruisstudie, zoals besproken in hoofdstuk 4, bieden een aanknopingspunt om de nanoporie chip opbouw aan te passen met als doel de ruis te verlagen. Om membraan fluctuaties te onderdrukken, is geprobeerd om het vrijstaand oppervlak van het grafeen te minimaliseren. De silicium basis chips voor de grafeen membranen, bevatten een relatief dik membraan van siliciumnitride met een ingebedde spiraal van platinum, met een totale dikte van ~600nm. De platinum spiraal is nodig om het grafeen te verhitten tijdens het fabriceren van de nanoporiën en nanostructuren in de STEM. In **hoofdstuk 5** wordt een methode beschreven om aan de onderzijde van het silicium nitride membraan een deel weg te etsen, zodat er lokaal een dun membraan ontstaat (tot zo'n 20nm). Deze techniek maakt het mogelijk om een kleiner gat te fabriceren, zodat het vrijstaand deel van het grafeen terug gebracht kan worden tot 50-100nm, zonder daarbij een hoge kanaalweerstand aan de nanoporie weerstand toe te voegen. De ionenstroom die gemeten is met nanoporie chips met een kleiner vrijstaand grafeen oppervlak, vertoont inderdaad een lager ruisniveau dan de originele grafeen nanoporie chips.

Het belangrijkste werk van dit promotieonderzoek wordt beschreven in **hoofdstuk 6**. Dit hoofdstuk beschrijft het ultieme experiment: de toets of het mogelijk is DNA te meten in de stroom door een grafeen nanolint, naast de ionenstroommeting, wanneer een DNA molecuul door een nanoporie in een grafeenlint beweegt. Voor de fabricage van grafeen nanostructuren met nanoporiën, van de kleinst mogelijke schaal met hoge geleidbaarheid, is hoge temperatuur STEM gebruikt. Met behulp van een zelf ontwikkelde differentiële stroomversterker, is gedemonstreerd dat weerstandsmodulaties in een grafeenstroom die ontstaat door DNA-grafeen interacties, onderscheiden kunnen worden van parasitaire capacatieve stromen die inherent zijn aan deze meetopstelling. Met de toegepaste meerstaps fabricage methode, konden kleine en goed geleidende nanostructuren gemaakt worden, maar het gebrek aan schaalbaarheid resulteerde in een lage opbrengst van meetbare devices. De conclusie van hoofdstuk 6 is daarmee dat DNA-detectie met grafeen nanolinten uitdagend, maar mogelijk is.

In het laatste hoofdstuk worden enkele conclusies van dit proefschrift uitgelicht. Hierbij wordt aandacht besteed aan de uitdagingen van de stroommeting door grafeen nanolint-

---

en met nanoporiën. De voor- en nadelen van verschillende fabricagemethoden worden besproken en de mogelijkheden voor het gebruik van andere tweedimensionale materialen worden aangestipt. Met de kennis van nu, wordt in **hoofdstuk 7** een persoonlijk perspectief gegeven op het gebruik van grafeen voor een DNA sequencing technologie.





# Curriculum Vitae

## Stephanie Joy Heerema

13-11-1985	Born in Leiden, The Netherlands
1998-2004	Gymnasium and IB English Rijnlands Lyceum Wassenaar, The Netherlands
2005-2008 & 2009-2012	B.Sc. & M.Sc Applied Physics Delft University of Technology, The Netherlands
2011	Internship at the Department of Cell Biology Netherlands Cancer Institute Amsterdam, The Netherlands
2011-2012	Master Student at the Physics of Living Systems Section Vrije Universiteit Amsterdam, The Netherlands <i>Thesis:</i> Sliding, Pausing, Bridging: how Human XRCC4 and XLF Interact with DNA <i>Supervisors:</i> Dr. A. Candelli, Prof. dr. G.J.L. Wuite, and Prof.dr. E.J.G. Peterman
2013-2018	Ph.D Department of Bionanoscience Kavli Institute of Nanoscience Delft University of Technology, The Netherlands <i>Thesis:</i> DNA sensing with nanopores in graphene nanoribbons <i>Promotor:</i> Prof. dr. C. Dekker





# List of publications

6. **S.J. Heerema**, L. Vicarelli., S. Pud, R.N. Schouten, H.W. Zandbergen, C. Dekker. Probing DNA Translocations with Inplane Current Signals in a Graphene Nanoribbon with a Nanopore. *ACS Nano*, DOI 10.1021/acsnano.7b08635, (2018).
5. M. Neklyudova, A. K. Erdamar, L. Vicarelli, **S.J. Heerema**, T. Rehfeldt, G. Pandraud, Z. Kolahdouz, C. Dekker, H.W. Zandbergen. Through-Membrane Electron-Beam Lithography for Ultrathin Membrane Applications. *Appl. Phys. Lett.* **111** (2017).
4. I. Brouwer, G. Sitters, A. Candelli, **S.J. Heerema**, I. Heller, A.J. de Melo, H. Zhang, D. Normanno, M. Modesti, E.J.G. Peterman, G.J.L. Wuite. Sliding Sleeves of XRCC4–XLF Bridge DNA and Connect Fragments of Broken DNA. *Nature* **535**, 566–569 (2016).
3. **S.J. Heerema** and C. Dekker. Graphene Nanodevices for DNA Sequencing. *Nature Nanotechnology* **11**, 127-136 (2016).
2. L. Vicarelli, **S.J. Heerema**, C. Dekker, H.W. Zandbergen. Controlling Defects in Graphene for Optimizing the Electrical Properties of Graphene Nanodevices. *ACS Nano* **9** , 3428-3435 (2015).
1. **S.J. Heerema**, G.F. Schneider, M. Rozemuller, L. Vicarelli, H.W. Zandbergen, C. Dekker.  $1/f$  Noise in Graphene Nanopores. *Nanotechnology* **26** (2015).



Casimir PhD series: 2018-09  
ISBN: 978.90.8593.341.0